SYNTHESIS AND CHARACTERIZATION OF LIGHT - WEIGHT, LEAD - FREE POLYMER COMPOSITES FOR X-RAY AND γ-RAY SHIELDING

Synopsis submitted to CHRIST (Deemed to be University)
as a partial requirement for the award of the degree of

DOCTOR OF PHILOSOPHY

IN

PHYSICS

by

SRILAKSHMI PRABHU

Under the supervision of

BUBBLY S G

Professor

CHRIST
(DEEMED TO BE UNIVERSITY)
BANGALORE · INDIA

Signature of Research Scholar

Signature of Research Supervisor

CENTRE FOR RESEARCH

CHRIST (Deemed to be University)

BENGALURU - 560029

AUGUST 2022

CENTRE FOR RESEARCH
Approval of PhD Synopsis

[as per clause 11(k.) of CU Regulation for the Degree of Doctor of Philosophy, May 2019]

Name of Scholar:	Srilakshmi Parbhu
Register Number:	1881301
Department:	Physics and Electronics
Name of Supervisor:	Prof. Bubbly S. G., Professor, Department of Physics and Electronics, CHRIST (Deemed to be University), Bengaluru-560029
Title of the PhD thesis:	Synthesis and characterization of light - weight, lead - free polymer composites for X-ray and γ-ray shielding

Names of Research Advisory Committee:

1. Prof. Bubbly S. G.
2. Prof. A. G. Kunjomana
3. Prof. Shivappa B. Gudennavar
4. Dr. Suman Mandal

Name and Designation of External Reviewer if applicable:	NA
Date of Synopsis Presentation:	25 July, 2022 at 6.30 pm

Approved by:

1. Name of Supervisor: Prof. Bubbly S. G. Bubblyfp
2. Name of RAC Member: Prof. A. G. Kunjomana Kunj. 02-08-2022
3. Name of RAC Member: Prof. Shivappa B. Gudennavar
4. Name of RAC Member: Dr. Suman Mandal Suman Mandal
5. Name of External reviewer if applicable

Head of Department

Date of approval by Doctoral Committee:

Director Centre for Research (Paul KT)

ABSTRACT

The present study has been focussed towards development of technologically viable and advanced radiation shielding materials to meet the safety requirements for use in medical imaging and diagnostic facilities, nuclear research laboratories, military operations, food sterilization industry, agriculture and so on. Designed from polymeric materials, based upon dispersion of non-lead based heavy metal/metal oxide fillers, these shields are both light in weight and environmentally friendly. Apart from offering good shielding efficiency, a high-performance shielding material must also possess multifunctional properties including good dimensional stability, high thermal resistance, good tensile strength and stability against drastic environment. In view of this, we have investigated the thermo-mechanical, viscoelastic and X-/γ-ray shielding ability of several polymer composites prepared by reinforcing high-Z metal oxide additives such as bismuth (III) oxide (Bi_2O_3), micro-/nano-tantalum (V) oxide (Ta_2O_5) and Bi_2O_3 decorated graphene oxide (GO) fillers (BGO) into polymers such as sodium alginate (SA) and epoxy resin, respectively by simple solution casting technique. Structural characterization of the synthesized composites was performed using X-ray diffraction (XRD), Fourier transform infrared (FTIR) spectroscopy and Raman spectroscopy. Microstructural analysis was carried out using energy dispersive X-ray analysis coupled with scanning electron microscopy (SEM-EDX) and ImageJ software. Microstructural analyses have confirmed the existence of fairly uniform dispersion of fillers within the SA and epoxy matrix with the average particle size of 15 µm, 4 µm, 75 nm and 42 nm in Bi_2O_3/SA, micro-Ta_2O_5/epoxy, nano-Ta_2O_5/epoxy and BGO/epoxy composites, respectively. Thermal stability of the polymer composites, as determined by thermogravimetric analysis (TGA), was found to increase with the filler loading, with degree of enhancement depending on choice of filler and/or matrix and filler size. SA composites with 40 wt% Bi_2O_3 loading showed peak degradation temperature as high as 251 °C, while that of epoxy containing 30 wt% nano-Ta_2O_5 and 15 wt% nano-BGO was found to be 409 °C and 418 °C, respectively. Similarly, tensile and viscoelastic properties of the composites were found to increase with filler loading as measured using universal testing machine (UTM) and dynamic mechanical analyser (DMA). Epoxy resin reinforced with nano-Ta_2O_5 (at 30 wt% loading) displayed highest tensile strength (~ 576 MPa) and elastic modulus (~ 11.4 GPa) among the studied composites, whereas Bi_2O_3/SA composites showed good level of flexibility. Variations in storage modulus and loss modulus of the composites with temperature indicated presence of strong matrix-filler interfacial adhesion and low heat build-up in the synthesized composites. Epoxy based materials are inherently water and chemical

resistant, while SA is a hydrophilic and highly functional polymer. With cross-linking of SA with optimum concentration of divalent calcium ions, we have developed robust and chemically resistant films of Bi_2O_3/SA. Further, the X-ray and γ-ray attenuation behaviour of Bi_2O_3/SA, micro-Ta_2O_5/epoxy, nano-Ta_2O_5/epoxy and BGO/epoxy composites were studied using CdTe and NaI(Tl) detector spectrometers, respectively. The mass attenuation coefficients (μ/ρ) of the composites were determined in the energy range of 30 – 1332 keV emitted produced by point sources, ^{22}Na, ^{137}Cs, ^{133}Ba and ^{60}Co. The experimental μ/ρ values were compared with those computed using PAGEX and were found to be in good agreement with each other. Interestingly, it was observed that at a given energy and filler loading, polymer nanocomposites exhibited superior shielding properties compared to micro counterparts, with effect being predominant at low filler loading. At 662 keV, μ/ρ value for 15 wt% nano-BGO loaded epoxy composite was found to be 0.098 $cm^2\ g^{-1}$, which is quite lower than that of 40 wt% Bi_2O_3/SA (0.090 $cm^2\ g^{-1}$), 30 wt% micro-Ta_2O_5/epoxy (0.087 $cm^2\ g^{-1}$) and 30 wt% micro-Ta_2O_5/epoxy (0.096 $cm^2\ g^{-1}$) composites. This could be attributed to influence of decoration of graphene oxide with Bi_2O_3 and consequent microstructural changes in the resultant nanocomposites, facilitating formation of continuous filler network across polymer phase, thereby enhancing attenuation. These observations, time and again, prove that surface decorated nanofillers at low level of loadings provide significant enhancement in material and shielding properties of polymers, making the composites resource-efficient. Having displayed good shielding performance in the energy range of medical and industrial interest, the composites under present study are potential candidates for light-weight and lead-free shielding materials.

Keywords: Sodium alginate, epoxy resin, bismuth oxide, tantalum oxide, graphene oxide, surface decoration, nanocomposites, thermo-mechanical, viscoelastic, X-/γ-ray shielding

TABLE OF CONTENTS

1. INTRODUCTION 1

2. STATEMENT OF THE RESEARCH PROBLEM 5

3. OBJECTIVES OF THE WORK 5

4. RESEARCH WORK CARRIED OUT 5

4.1 Bismuth (III) oxide filled sodium alginate composites 5

4.1.1 Materials and synthesis 6

4.1.2 Water sensitivity, chemical resistance, biodegradability, structural and thermo-mechanical studies on SA/Bi_2O_3 6

4.1.3 X-/γ-ray attenuation properties of SA/Bi_2O_3 13

4.1.4 Conclusions 18

4.2 Micro/nano tantalum (V) oxide filled DGEBA epoxy composites 19

4.2.1 Materials and synthesis 20

4.2.2 Structural, thermo-mechanical and viscoelastic properties of m-Ta_2O_5/epoxy and n-Ta_2O_5/epoxy composites 20

4.2.3 X-/γ-ray attenuation properties of m-Ta_2O_5/epoxy and n-Ta_2O_5/epoxy composites 27

4.2.4 Conclusions 29

4.3 Bismuth (III) oxide decorated graphene oxide filled DGEBA epoxy nanocomposites 31

4.3.1 Materials and synthesis 31

4.3.2 Structural and thermal properties of BGO nanocomposites 32

4.3.3 Structural, thermo-mechanical and viscoelastic properties of BGO/epoxy nanocomposites 35

4.3.4 X-/γ-ray attenuation properties of BGO/epoxy nanocomposites 37

4.3.5 Conclusions 41

4.4 PAGEX: A simple and robust software for computation of photon and charged particle interaction parameters 41

4.4.1 Rationale behind the work 41

4.4.2 PAGEX – The software 42

4.4.3 PAGEX validation 43

4.4.4 Conclusions 48

5. SUMMARY AND FUTURE WORK 49

5.1 Summary of the work 49

5.2 Future prospects 54

BIBLIOGRAPHY 55

PUBLICATIONS/PROCEEDINGS 64

List of Tables

Table 4.1.1: Thermal stability parameters of neat and Bi_2O_3 filled SA composites. 12

Table 4.1.2: Tensile characteristics of neat and Bi_2O_3 filled SA composites. 13

Table 4.1.3: Experimental (E) and PAGEX (T) μ/ρ values of the composites in the energy range 30 – 1332 keV and relative deviation (D%) between them. 16

Table 4.1.4: Comparison of μ/ρ values from the present work with literature. 18

Table 4.2.1: Thermal properties of neat and Ta_2O_5 filled epoxy composites. 24

Table 4.2.2: Tensile properties of neat and Ta_2O_5 filled epoxy composites. 24

Table 4.2.3: Thermo-mechanical properties of neat and Ta_2O_5 filled epoxy composites. 27

Table 4.2.4: Experimental (E) and PAGEX (T) values of μ/ρ, density, relative increase rate (d%) for neat epoxy, m-Ta_2O_5/epoxy and n-Ta_2O_5/epoxy composites. 28

Table 4.2.5: Comparison of μ/ρ values at various energies of γ-rays. 30

Table 4.3.1: Thermal stability parameters of neat epoxy and BGO filled epoxy nanocomposites. 36

Table 4.3.2: Tensile characteristics of neat epoxy and BGO filled epoxy nanocomposites. 37

Table 4.3.3: Thermo-mechanical properties of neat epoxy and BGO filled epoxy nanocomposites. 38

Table 4.3.4: Comparison of μ/ρ values. 40

Table 4.4.1: Various software and parameters computed. 44

Table 4.4.2: Percentage of deviation of PAGEX μ/ρ values from WinXCom. 47

Table 5.1.1: Synergistic properties of synthesized composites. 53

List of Figures

Figure 4.1.1: Schematic illustration of the preparation of calcium ion cross-linked (A) and Bi_2O_3 reinforced (B) SA composite films. 6

Figure 4.1.2: Effect of Bi_2O_3 addition on water solubility (WS) and swelling ratio (SR) of SA/Bi_2O_3 films. 7

Figure 4.1.3: XRD of neat and Bi_2O_3 filled SA composites. 9

Figure 4.1.4: (i) SEM images of (a) S10B, (b) S20B, (c) S30B and (d) S40B composites and (ii) analysis of Bi_2O_3 filler size and distribution in matrix using ImageJ. 10

Figure 4.1.5: Left: FTIR spectra of (a) neat SA film and SA film cross-linked with (b) 0.5 wt%, (c) 1 wt%, (d) 1.5 wt% and (e) 2 wt% Ca^{2+} ions. Right: Magnified FTIR spectra of dashed box in left. 11

Figure 4.1.6: (a) TGA and (b) DTG curves for neat and Bi_2O_3 filled SA composites. 12

Figure 4.1.7: Schematic diagram of attenuation experimental setup. 14

Figure 4.1.8: (a) Z_{eff} and (b) N_{eff} of the composites. 18

Figure 4.1.9: Comparison of % heaviness. 19

Figure 4.2.1: Schematic illustration of the preparation of micro/nano - Ta_2O_5 epoxy composite films. 21

Figure 4.2.2: Representative (a) XRD and (b) FTIR spectra neat (E0), 10 wt% micro-Ta_2O_5 (E10mT) and 10 wt% nano-Ta_2O_5 (E10nT) loaded DGEBA epoxy composites. 22

Figure 4.2.3: SEM images of m-Ta_2O_5 and n-Ta_2O_5 filled DGEBA epoxy composite films. 23

Figure 4.2.4: Variation of storage modulus of (a) m-Ta_2O_5/epoxy and (b) n-Ta_2O_5/epoxy composites, damping curves of (c) m-Ta_2O_5/epoxy and (d) n-Ta_2O_5/epoxy composites. 26

Figure 4.3.1: Schematic illustration of the preparation of BGO/epoxy nanocomposite films. 31

Figure 4.3.2: XRD patterns of Bi_2O_3, GO and BGO composite. 33

Figure 4.3.3: (a) FTIR and (b) Raman spectra of Bi_2O_3, GO and BGO composite. 33

Figure 4.3.4: SEM image of (a) GO (b) Bi_2O_3 and (c) BGO composite and (d) particle size distribution of BGO fillers. 34

Figure 4.3.5: SEM images of (a) 5 wt%, (b) 10 wt% and (c) 15 wt% BGO filled epoxy composites. 35

Figure 4.3.6: (a) TGA curves of BGO filled epoxy composites and (b) comparison of thermal resistance of various resin-based polymer composites. 36

Figure 4.3.7: Variation of μ/ρ of epoxy nanocomposites with BGO loading. 39

Figure 4.4.1: Flowchart of PAGEX software. 46

Figure 4.4.2: (a) PAGEX GUI, (b) main page of PAGEX showing the material input, parameters grid and output options and (c) graphical output from PAGEX. 46

Figure 4.4.3: Comparison of Z_{eff} values from PAGEX and Auto-Z_{eff}. 47

Figure 4.4.4: Comparison of EABF and EBF values for water, concrete and air from PAGEX and ANSI database. 48

Figure 4.4.5: Variation of Z_{eff} as function of kinetic energy for proton, electron and alpha particle interaction. 48

Figure 5.1.1: Comparison of (a) $T_{10\%}$, (b) tensile strength, (c) storage modulus and (d) % elongation at break between micro- and nano-Ta_2O_5/epoxy composites at various filler loadings. 51

Figure 5.1.2: Comparison of %E of various polymer composites at 10 wt% filler loading. 51

1. INTRODUCTION

With the advanced technologies playing a supporting role in having better healthcare and sustainable development, the use of X-rays and γ-rays has become indispensable in various sectors such as medical radiation facilities, nuclear research laboratories, industrial gauging, food irradiation, geological exploration, military and security operations. According to World Health Organization (WHO), medical industry makes the highest utilization of ionizing radiations, accounting for 98% of the population dose contribution from all artificial radioactive sources and 20% of total population exposure. Approximately, 3600 million diagnostic radiological examinations, 7.5 million radiotherapies and 37 million nuclear medicine operations are conducted worldwide each year (WHO). In general, it is impracticable for patients, occupational workers and radiation researchers to keep away from workplace radiation exposure. Undesired exposure to these ionizing radiations may cause short- and long-term adversities including acute radiation syndrome, cancer, somatic and genetic damage. To address the global problem of planned, existing, and emergency radiation exposure scenarios, it is crucial to design personal protective equipment (PPE) in the form of protective clothing that functions as an external barrier to shield against high energy radiations.

Designing effective radioprotective materials requires understanding of the underlying mechanisms of interaction of radiation with matter. While X-rays interact with matter primarily through photoelectric absorption and Compton scattering, γ-rays interact with matter through photoelectric absorption and Compton scattering and pair production depending on the energy (E) of incident radiation and atomic number (Z) of interacting medium. Consequently, high-Z and high-density materials offering greater interaction probability are often employed to develop shields. Traditionally employed metallic lead (Pb) shields are no longer preferred due to their high carcinogenicity, disposal challenges, and the ergonomic inconvenience of wearing hefty shields. The ever-increasing demand for cost-effective and environmentally sustainable shielding materials has resulted in the development of metal matrix composites, concrete and ceramics and glass matrix composites as shields. Nonetheless, considering some of the drawbacks of these materials, the search for light-weight, low-maintenance and conformable materials that may be tailored according to specific applications is in progress.

Polymers have undoubtedly emerged as the most promising matrix materials for developing high performance composites for radiation shielding applications in recent years. As a matrix, polymer offers desirable material properties including ease of processability, light-weight, low-maintenance, good workability and environmental resilience (Arshad et al., 2020). Polymers

being low-Z materials, they cannot offer the required shielding efficiencies on their own. As a result, polymers have been reinforced with suitable fillers/additives to develop competent and effective shielding materials in the form of polymer matrix composites (PMCs). In the last few decades, varieties of polymers such as polyethylene (PE), polypropylene (PP), epoxy resin, unsaturated polyester, natural rubber (NR), ethylene propylene diene monomer rubber (EPDM), polyvinyl alcohol (PVA), poly(methyl methacrylate) (PMMA), polydimethylsiloxane (PDMS) and so on have been explored for shielding purpose (Belgin and Aycik, 2015; Ambika et al., 2017; Mirzaei et al., 2018; Muthamma et al., 2019; Cao et al., 2020; Intom et al., 2020; Fan et al., 2020; Yılmaz et al., 2020; Muthamma et al., 2021). Fillers can improve the thermal stability and physico-mechanical characteristics of PMCs in addition to the enhancement in shielding properties. Some of the most commonly used fillers include metals (lead, tantalum, tungsten), metal oxides (copper oxide, gadolinium oxide, lead oxide, tungsten oxide, bismuth oxide), fibrous materials (Kevlar, basalt fibres, glass fibers), minerals (chalcocite, hematite, perovskites) and so on (Gwaily et al., 2002; Chang et al., 2015; Li et al., 2017; Zegaoui et al., 2018; Mahmoud et al., 2019; Adlienė et al., 2020; Zegaoui et al., 2020; Mahmoud et al., 2020; Yu et al., 2021). Polymers reinforced with nanofillers have demonstrated exceptional size-dependent radiation shielding effects, as well as significant impact on their physico-mechanical and thermal characteristics at much lower concentrations compared to micron sized fillers (Kim et al., 2014; Mahmoud et al., 2018; Asgari et al., 2021; Muthamma et al., 2021; Abbas et al., 2022; Hosseini et al., 2022).

In order to clearly understand the approaches and emerging trends in the use of polymer composites for radiation shielding applications, we have conducted an extensive literature review. The outcome of this survey and its analysis has resulted in a review article titled "*X-ray and γ-ray shielding efficiency of polymer composites: Choice of fillers, effect of loading and filler size, photon energy and multifunctionality*" (*Polymer Reviews*, (1 – 44), 2022). Having identified the research gap, we planned to employ sodium alginate and epoxy resin as polymer matrices to develop composites for X-ray and γ-ray radiation shielding using different metal fillers in micro and nano forms. We have developed sodium alginate composites loaded with different wt% of Bi_2O_3 in micro form, epoxy resin composites loaded with Ta_2O_5 in micro and nano form, and Bi_2O_3 decorated graphene oxide (GO) epoxy composites. These synthesized polymer composites were characterized experimentally for their structural, thermal, mechanical properties, and radiation attenuation characteristics theoretically and experimentally.

Sodium alginate (SA) is a naturally occurring polymer which offers attractive properties such as low-cost availability, abundance, biodegradability and biocompatibility (Sime 1990; Lee and Mooney, 2012). With its rigid molecular chain and good film forming ability, SA has been extensively used for biomedical applications (Nishiya et al., 1994; Augst et al., 2006; Kaneda et al., 2008; Sachan et al., 2009; Singh et al., 2010; Kumar Giri et al., 2012; Abasalizadeh et al., 2020). SA can form a rigid 3D interpenetrating hydrogel network on cross-linking with multivalent metal cations (Pavlath et al., 1999). We have developed composites of SA loaded with different concentrations of Bi_2O_3 to study their efficacy as γ-ray shielding materials. Bismuth (Bi), with Z = 83 and ρ = 8.98 g cm^{-3}, offers similar shielding ability to an equal mass of Pb but at higher thickness due to its lower density than Pb (McAlister, 2012). Bismuth (III) oxide (Bi_2O_3), in particular, is commercially available at low cost with no evidence of mutagenicity and teratogenicity. We have examined the composites for their water and chemical resistance, thermal stability, tensile properties and biodegradability as function of Bi_2O_3 loading.

Diglycidyl ether of bisphenol A (DGEBA) epoxy resin is an industrially interesting and advanced versatile thermosetting polymer that provides excellent mechanical strength and toughness. With no volatile emissions and low shrinkage upon curing, it is desirable in the production of void-free composites. We have synthesized epoxy composites loaded with different concentrations of tantalum (V) oxide (Ta_2O_5). With a density of 8.2 g cm^{-3}, high melting point (1872 °C) and high Youngs modulus (~ 190 GPa), Ta_2O_5 can impart good thermo-mechanical and X-/γ-ray shielding properties to the polymers on par with Bi- or W-based materials (Canel et al., 2019; Adliene et al., 2020; Muthamma et al., 2020). Along with γ-ray (0.356 – 1.332 MeV) attenuation studies, we have also carried out detailed investigations on the structural, thermal, tensile and viscoelastic properties of epoxy composites as function of both Ta_2O_5 filler loading and filler size (micro and nano). The enhanced thermo-mechanical and γ-ray shielding properties displayed by the epoxy nanocomposites, at low nanofiller loading, compared to their micro counterparts, further motivated us to investigate the profound prospects of nanostructured materials in enhancing the probability of radiation interaction cross-section of X- and γ-rays.

Surface modification of inorganic fillers has succeeded in addressing the challenges involved in the synthesis of agglomeration-free nanocomposites with enhanced matrix-filler interfacial adhesion (Hashemi et al., 2018; Pavlenko et al., 2019). Polymer matrices reinforced with graphene oxide (GO) surface decorated with metal oxides, where GO acts as a carrier of metal

oxides, has resulted in their uniform distribution throughout the matrix, thereby enhancing the shielding properties (Hashemi et al., 2018). Also, surface decoration almost certainly changes the size and microstructure of the changed structures, hence influencing the overall physico-mechanical characteristics of the reinforced phase (Pavlenko et al., 2019). Furthermore, the combination of low-Z elements (particularly carbon and oxygen) with heavy metals (cerium, gadolinium, bismuth, and so on) influences attenuation behaviour of shields by increasing the likelihood of Compton scattering, hence improving overall shielding qualities (Hashemi et al., 2018; Zohdiaghdam et al., 2020). Since both GO and Bi_2O_3 have high biocompatibility and low toxicity, we have considered their combination as fillers for further studies. Therefore, we synthesized Bi_2O_3 decorated GO and employed the same as fillers in DGEBA epoxy resin at different loadings. The correlation between surface decoration, filler size and loading, dispersion and interfacial adhesion between matrix-filler phase was systematically examined as function of thermo-mechanical and viscoelastic properties of the composites. Further, we also explored the shielding efficiency of these nanocomposites for X-ray and γ-ray.

The shielding ability of materials is usually evaluated in terms of the radiological properties of the irradiated medium depending on the type and energy of the radiations. The photon mass attenuation coefficient (μ/ρ, $cm^2\ g^{-1}$) is the most widely used parameter to quantify the shielding efficiency and is determined experimentally. All other related parameters can be derived from the μ/ρ values. The experimentally determined μ/ρ values and other parameters are often compared with the theoretically estimated values. Despite the availability of several data tables, programs and software tools for theoretical calculations, none of them offered the possibility to compute all the parameters on a single platform. In view of this, we developed a user-friendly Python-based graphical user interface (GUI) software named PAGEX (**P**roton, **A**lpha, **G**amma, **E**lectron and **X**-ray) which is more comprehensive than existing packages, namely, WinXCom (Gerward et al. 2004), ASTAR, ESTAR and PSTAR (Berger et al., 2005), SRIM (Zeigler et al., 2010) and Auto-Z_{eff} (Taylor et al., 2012), and simplifies the task of manual calculation of various radiation interaction parameters. This software allows the user to compute desired photon and charged particle interaction parameters for any kind of material simultaneously for continuous standard energy grid and user-defined energies. Designed on basis of well-established theoretical formulations and computational techniques, PAGEX is verified for its accuracy and reliability. Following the comprehensive literature survey, we have defined the statement of our research problem as follows.

2. STATEMENT OF THE RESEARCH PROBLEM

Radiation protection is a major concern in medical diagnostics and therapy, nuclear research laboratory and occupational hazard workers. Traditionally employed lead-based materials are no longer desirable as they are bulky and highly toxic. Therefore, the light-weight and lead-free polymer-matrix composites (PMCs) are suitable candidates for developing high performance shields.

3. OBJECTIVES OF THE WORK

The research work carried as part of the PhD thesis has been accomplished through the following objectives:

(a) Synthesis of lead-free sodium alginate and epoxy-based polymer composites by simple solution casting technique.
(b) Characterization of as-synthesized polymer composites for structural, thermal, mechanical and viscoelastic properties.
(c) X-/γ-ray attenuation studies of the composites by theoretical computations and experiments.

In the following section, we present a brief description of the work carried out in meeting the above stated objectives.

4. RESEARCH WORK CARRIED OUT

Three different lead-free polymer composite systems namely, SA/Bi_2O_3, micro/nano-Ta_2O_5/epoxy and Bi_2O_3 decorated GO loaded epoxy, were synthesized and characterized for various structural, thermo-mechanical, viscoelastic and X-/γ-ray shielding properties. Studies conducted on each of these composite systems are detailed in the following subsections.

4.1 Bismuth (III) oxide filled sodium alginate composites

In this study, we investigated the radioprotective effectiveness of bismuth (III) oxide (Bi_2O_3) loaded, calcium (Ca) ion cross-linked solution cast sodium alginate (SA) composite films. First, we studied the effect of Ca^{2+} ion cross-linking on water and chemical resistance of SA. Further, Ca^{2+} ion cross-linked SA matrix was loaded with Bi_2O_3 at varying loading (0 – 40 wt%) and the structural, thermo-mechanical and X-/γ-ray attenuation properties of these composites were studied. The details on synthesis of the composites, their characterization and results are presented in the following sections.

4.1.1 Materials and synthesis

Sodium alginate (MW = 120,000 g mol^{-1}; ρ = 1.61 g cm^{-3}) was procured from Loba Chemie Pvt. Ltd. Mumbai, India. Bismuth (III) oxide (99.99%) (MW = 465.96 g mol^{-1}; ρ = 8.90 g cm^{-3}) was procured from Research Laboratory, Bengaluru, India. All the solvents, acids, bases and other chemicals were of analytical grade and were used without further modification. All aqueous solutions were prepared using double distilled water.

All the SA composite films were prepared by solution casting method (Figure 4.1.1). The concentration of $CaCl_2.2H_2O$ in film forming SA solutions was varied from 0 to 2 wt% in steps of 0.5 wt%. Beyond 2 wt% $CaCl_2$ addition, there was immediate gelling, making it difficult to stir the solution and cast it. SA film with 1.5 wt% calcium chloride (SCa) was found to be optimum after the solubility tests. Furthermore, Bi_2O_3 was loaded into SCa film solutions varying from 0 – 40 wt% in steps of 10 wt% to develop composite films S10B, S20B, S30B, and S40B, respectively.

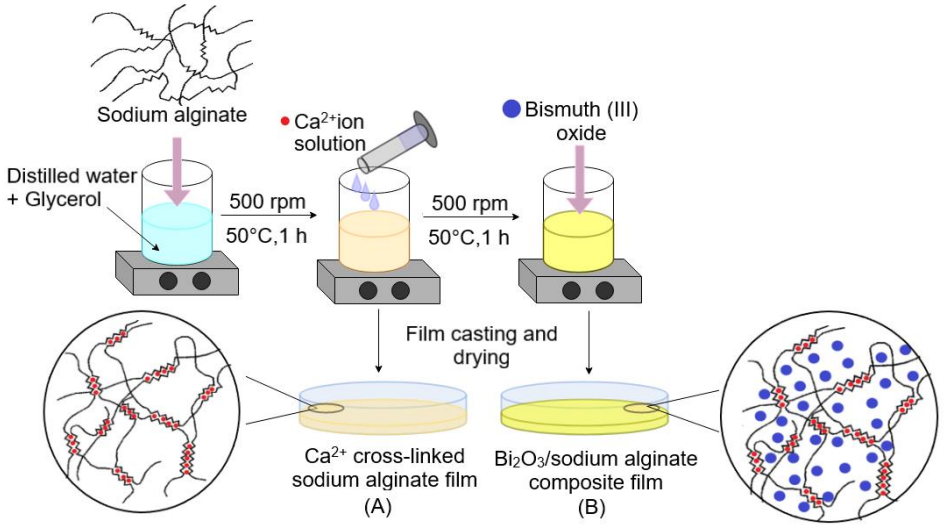

Figure 4.1.1 Schematic illustration of the preparation of calcium ion cross-linked (A) and Bi_2O_3 reinforced (B) SA composite films.

4.1.2 Water sensitivity, chemical resistance, biodegradability, structural and thermo-mechanical studies on SA/Bi_2O_3

The composites of SA/Bi_2O_3 were characterized to study their material characteristics such as water sensitivity, chemical resistance, biodegradability, thermal stability and tensile properties.

Water sensitivity (WS) of SA-based films were estimated quantitatively using the method discussed by Rhim (2004). WS test performed at room temperature on neat and Ca^{2+} cross-linked SA films showed that the neat SA film had maximum solubility. The WS of the films dropped as the $CaCl_2$ content increased from 0.5 to 1.5 wt%. All $CaCl_2$ treated films retained

their integrity in distilled water at ambient circumstances even after 12 months. The increase in water resistance of the films is mostly due to interaction of Ca^{2+} ions with -COOH groups of adjacent SA polymer chains, resulting in cross-linking and the formation of junction zones.

Swelling ratio of the SA-based films were determined by using weight ratio technique (Huang and Yang, 2010; Manjula et al., 2013). All the samples exhibited fast swelling at first, and afterwards swelling ratios (SR) attained sorption equilibrium when immersed in water. On comparison with untreated films, $CaCl_2$ treated films had lower SR values and quicker equilibration times. Because the swelling behaviour and cross-linking density are inversely related, a reduction in SR with Ca^{2+} concentration implies an increase in degree of cross-linking and the creation of a rigid network capable of repelling water penetration. No significant change in weight was seen even after 24 hours of immersion in distilled water, indicating that Ca^{2+} cross-linking improves the dimensional stability of the SA network. The effect of Bi_2O_3 loading on the WS and SR of composite films is shown in Figure 4.1.2. The slight decrease in WS of films with increasing filler loading is due to the development of hydrogen bonds between the hydroxyl and carboxyl groups on SA. The SR of composite films reduced as the Bi_2O_3 concentration increased, and the composite films reached sorption equilibrium substantially faster than neat sodium alginate (S0) and SCa films. After only 5 minutes of immersion, the 40 wt% SA/Bi_2O_3 films reached equilibrium. This is most likely due to a decrease in SA and an increase in Bi_2O_3 concentration, which is essentially insoluble in water.

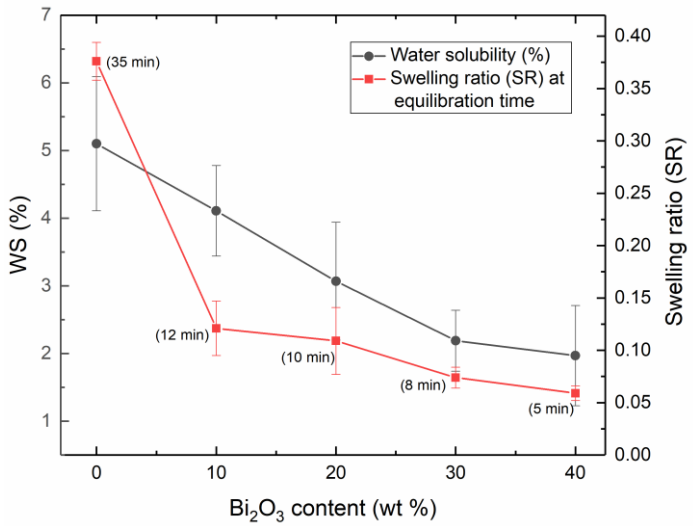

Figure 4.1.2. Effect of Bi_2O_3 addition on water solubility (WS) and swelling ratio (SR) of SA/Bi_2O_3 films.

The chemical resistance of SA-based films was determined according to ASTM D543–95 standard test procedure. All of the composite films demonstrated good chemical resistance

(after 30 days) in the studied chemical environments (acetone, aniline, carbon tetrachloride, dimethyl formamide, 95% ethyl alcohol, methyl alcohol, toluene, glacial acetic acid, concentrated hydrochloric acid, concentrated sulphuric acid, and edible olive oil), except for an alkaline environment containing 10% ammonium hydroxide and 10% sodium hydroxide solutions. The chemical resistance of SA/Bi_2O_3 composite films was greater than that of unfilled samples (S0 and SCa). The increase in chemical resistance with filler loading could be attributed to the chemical inertness of Bi_2O_3. Nonetheless, samples soaked in alkaline solution revealed slight weight loss after 168 hours, which increased with each week until 30 days. In the current study, the S40B sample outperformed all other samples in terms of chemical resistance.

Natural soil biodegradability test on SA-based films was carried out by soil burial method (Riyajan et al., 2012; Deepa et al., 2016). The effect of Bi_2O_3 loading on the weight loss rate (WL%) of SA/Bi_2O_3 films in natural soil was studied to understand their biodegradability. After 4 weeks of burial, the samples S0, SCa, S10B, S20B, S30B, and S40B samples were found to be 70%, 60% 45%, 38%, 31%, and 26% biodegradable, respectively. While the homogenous distribution of fillers and strong interfacial adhesion between matrix and filler phase may make bond breaking harder, the decrease in biodegradable SA concentration with Bi_2O_3 loading also explains the slower rate of biodegradation. However, SA/Bi_2O_3 composite films have a substantially better biodegradability prognosis than polymers such as polyester, polypropylene, polyethylene, and others that are very resistant to soil breakdown (Ibrahim et al., 2021; Sharma et al., 2021).

X-ray diffractograms (XRD) of the SA-based samples were obtained using Bruker AXS D8 Advance X-ray diffractometer in the 2θ range of 0° to 120° at a scan rate of 2° min^{-1} and the patterns of neat and Bi_2O_3-filled SA composites are shown in Figure 4.1.3. Amorphous SA was assigned a large diffraction peak occurring about 2θ = 23°. The spectra of Bi_2O_3-filled samples S10B, S20B, S30B, and S40B revealed multiple strong peaks, including notable ones at 2θ = 27.4°, 33.3°, and 46.3° corresponding to the (120), (121), and (311) diffraction planes of the monoclinic phase of α-Bi_2O_3 (JCPDS 76-1730). Small peaks over 50° in the spectra at around 52.4° (321), 54.8° (241), 55.9°, 56.5°, and 59.2° (024) also correspond to Bi_2O_3 fillers. The intensities of all these sharp peaks were seen to increase slightly with increase in Bi_2O_3 content, whereas intensity of the broad SA peak decreased. These results indicated that crystallinity of the films increased with filler loading (Shah et al., 2009).

High resolution SEM images of the SA-based samples were obtained using JEOL Model JSM-6390LV to examine the microstructural changes in SA films caused by Ca^{2+} cross-linking. Neat SA film showed smooth surface whereas Ca^{2+} cross-linked SA films appeared to have a coarser surface with irregularities and interconnected morphologies. The latter indicates the occurrence of ion exchange and subsequent cross-linking processes. Furthermore, SEM images of SA/Bi_2O_3 composites are shown in Figure 4.1.4. Long needle-shaped - Bi_2O_3 fillers are seen to be dispersed evenly throughout the SA matrix in the composite films, and the film surface seems to become compact as loading increases, indicating an increase in composite density. ImageJ software analysis shows that the average particle size is roughly 15 µm (Figure 4.1.4(ii)).

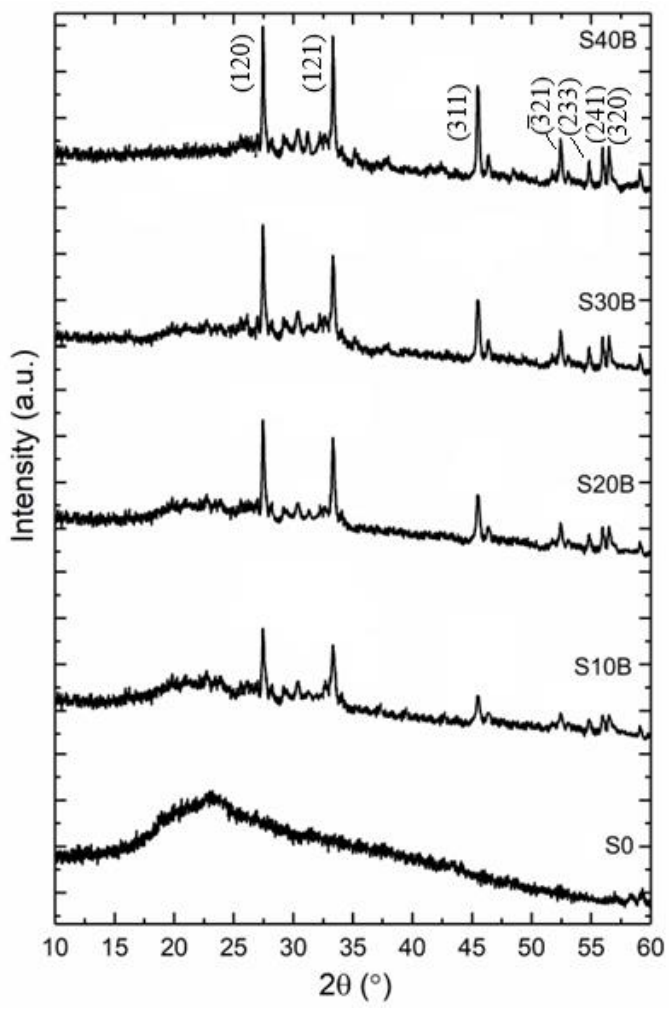

Figure 4.1.3. XRD of neat and Bi_2O_3 filled SA composites.

FTIR spectra of SA-based samples were recorded on Thermo Nicolet Avatar 370 spectrometer (Waltham, MA) in transmission mode in the wavenumber range 400 – 4000 cm^{-1}. Left panel of Figure 4.1.5 shows the FTIR spectra of SA films before and after addition of varying amounts of $CaCl_2$. The bands at 3446, 2930 and 1029 cm^{-1} in neat SA is ascribed to -O-H

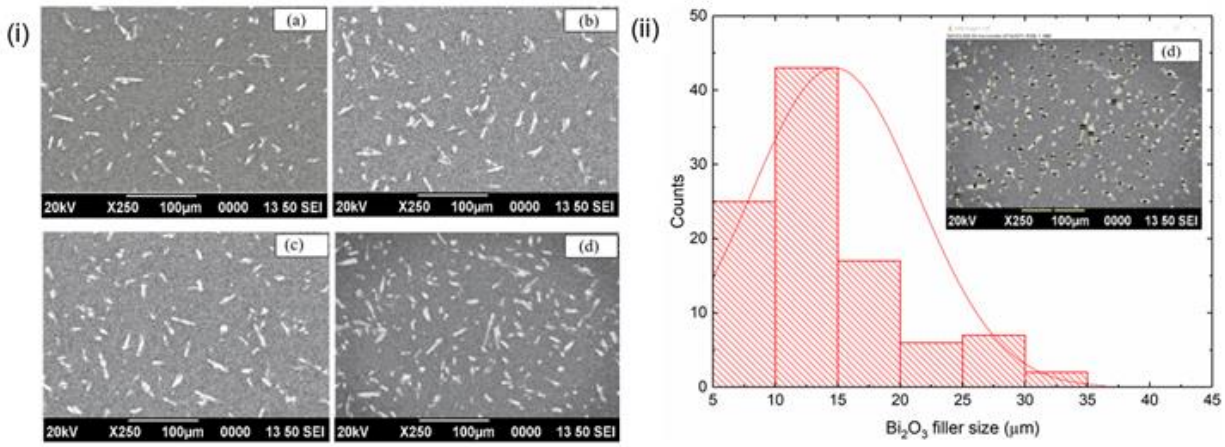

Figure 4.1.4. (i) SEM images of (a) S10B, (b) S20B, (c) S30B and (d) S40B composites and (ii) analysis of Bi_2O_3 filler size and distribution in matrix using ImageJ.

stretching vibration, -C-H of aliphatic chain stretching vibrations and stretching vibration of -C-O-C groups, respectively. With the addition of $CaCl_2$, there is a slight increase in the intensity of -O-H band indicating intramolecular bonding. The peak at 1617 cm^{-1} indicates the abundance of uronic acid residues in SA. When SA film was cross-linked with increasing amounts of Ca^{2+}, the asymmetric -COO peak shifted towards the lower wavenumber side (from 1617 to 1604 cm^{-1}) and the symmetric -COO peak shifted towards the higher wavenumber side (from 1402 to 1417 cm^{-1}), as shown in Figure 4.1.5(a–e) right panel, consistent with literature reports (Zheng et al., 2016; Lima et al., 2018; Badita et al., 2020). This is due to ion exchange between Na^+ ions in the SA matrix and Ca^{2+} ions, with the Ca^{2+} ions forming strong electrostatic interactions with the SA carboxylate group. When the $CaCl_2$ concentration approached 1.5 wt%, the position and intensity of both symmetric and asymmetric -COO peaks did not change, implying that the probable Na^+ ions were entirely replaced with Ca^{2+} ions.

The FTIR spectra of SA/Bi_2O_3 composites revealed the presence of all of the characteristic peaks associated with Ca^{2+} ion cross-linked SA and Bi_2O_3. With Bi_2O_3 introduction into SCa matrix, the intensity and width of the overall -OH (3446 cm^{-1}) band altered slightly which might be caused by the creation of weak hydrogen bonds between SCa and the Bi_2O_3 via adsorbed water molecules on the latter. With increasing Bi_2O_3 loading, the intensity of the absorption bands typical of SA between 2000 – 450 cm^{-1} decreased. Three additional bands in the FTIR spectra were found at 845, 611, and 543 cm^{-1}, corresponding to Bi-O-Bi and Bi-O bonds, respectively, and their intensity increased with loading.

Perkin Elmer Diamond TG/DTA instrument was used to carry out the thermogravimetric analysis (TGA) of the vacuum dried sample films heated from room temperature up to 800 °C

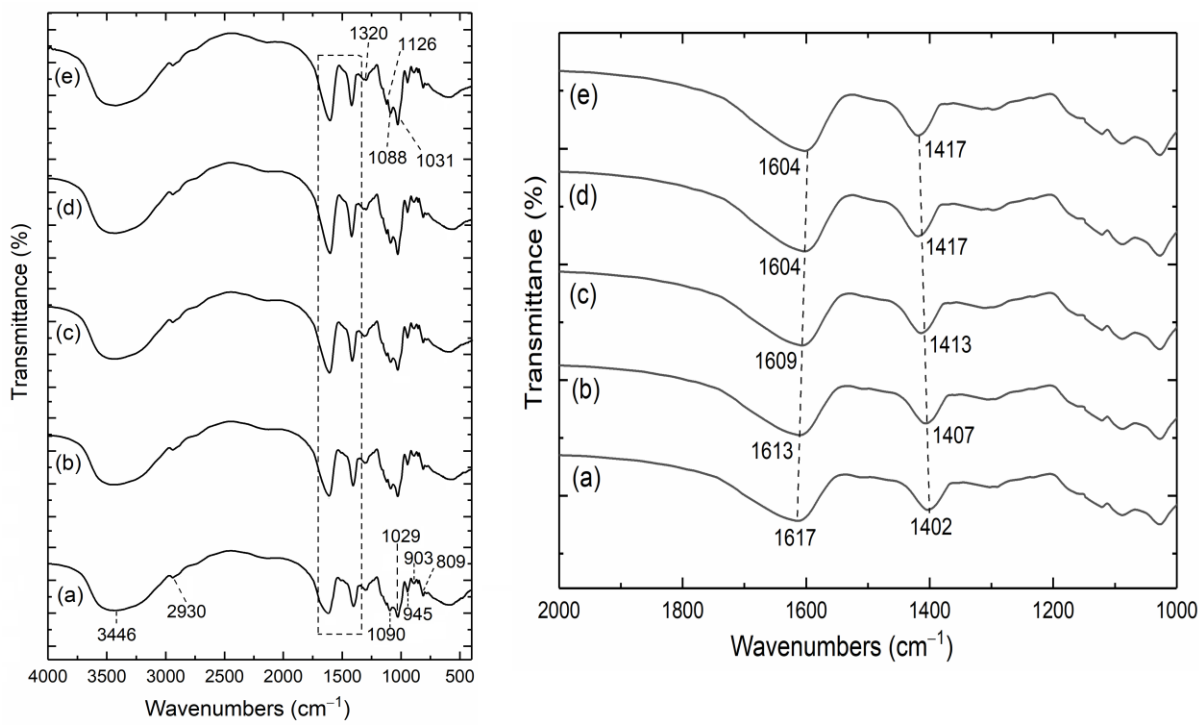

Figure 4.1.5. Left: FTIR spectra of (a) neat SA film and SA film cross-linked with (b) 0.5 wt%, (c) 1 wt%, (d) 1.5 wt% and (e) 2 wt% Ca^{2+} ions. Right: Magnified FTIR spectra of dashed box in left.

at a scan rate of 10 °C min^{-1} at a constant nitrogen purging rate of 100 mL min^{-1}. Figure 4.1.6(a) represents thermograms of SA/Bi_2O_3 composites. The initial slight weight loss seen for S0 and SCa samples below 120 °C, attributed to the loss of trapped and physiosorbed water molecules that interact with the -OH and -COO polar groups in the SA chain via hydrogen bonding, was substantially lower in Bi_2O_3 loaded samples. Furthermore, the region of major weight loss (200 to 250 °C) in S0 and SCa samples was larger (220 – 300 °C) in Bi_2O_3 loaded samples due to glycosidic link breakdown, dehydration, decarboxylation, and decarbonylation of SA. The broader zone of deterioration in Bi_2O_3 loaded SA composites demonstrates their better temperature resilience. SA is entirely degraded and carbonised at 300 °C, resulting in the production of inorganic char. Thermal stability of the composites in terms of 10% sample weight loss temperature ($T_{10\%}$), 50% sample weight loss temperature ($T_{50\%}$), char yield (Y_c), peak decomposition temperature (T_p) and maximum weight loss rate (R_{max}) as recorded at 500 °C are presented in Table 4.1.1. With increase in Bi_2O_3 loading, the above-mentioned parameters are observed to increase. The incorporation of high melting point inorganic Bi_2O_3 fillers (melting point = 817 °C) in SA matrix might have caused the delay in early disintegration and improvement in thermal stability of SA composites. Thus, thermal stability of the composites increased in the order S0 < SCa < S10B < S20B < S30B < S40B, same as that of

their crystallinity, implying that crystalline domains of Bi_2O_3 fillers enhanced heat resistance property of SA. All the derivative thermogram curves showed wide decomposition temperatures and shift of T_p towards higher temperature side indicating the thermal reinforcing efficiency of Bi_2O_3 fillers (Figure 4.1.6(b)).

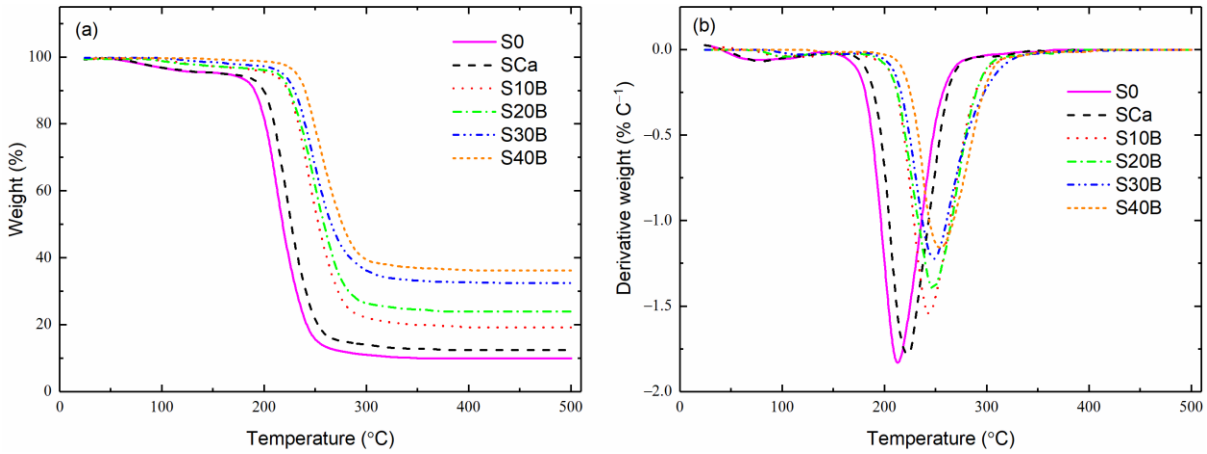

Figure 4.1.6. (a) TGA and (b) DTG curves for neat and Bi_2O_3 filled SA composites.

Table 4.1.1. Thermal stability parameters of neat and Bi_2O_3 filled SA composites.

Sample	$T_{10\%}$ (°C)	$T_{50\%}$ (°C)	Y_c (%)	T_p (°C)	R_{max} (% °C^{-1})
S0	191.88	223.88	9.96	217.91	– 2.11
SCa	197.38	228.74	12.38	221.74	– 2.02
S10B	219.90	252.10	19.30	242.33	– 1.72
S20B	225.95	258.47	23.99	246.47	– 1.62
S30B	232.54	266.94	32.74	249.06	– 1.43
S40B	236.66	273.03	37.60	251.65	– 1.34

Tensile properties of SA-based films were measured according to ASTM D882-02 using an Instron Universal Testing Machine. Stress-strain curves showed the trend similar to that of soft-elastic and hard-tough materials for S0 and Bi_2O_3 filled composites, respectively. Tensile strength (TS), Young's modulus (YM) and % elongation at break (%E) as estimated from stress-strain curves are presented in Table 4.1.2. The presence of Ca^{2+} ions in the SA matrix favoured TS and YM but not %E. The improvement in the TS and YM is most likely due to increased cross-linking network density caused by Ca^{2+} ions. Furthermore, when varying quantities of Bi_2O_3 fillers were added to the SCa matrix, TS and YM increased but E% decreased. Such a significant increase in TS and YM could be attributed to (a) strong interfacial adhesion between the cross-linked SA matrix and the Bi_2O_3 fillers and (b) homogeneous distribution of the Bi_2O_3 fillers into the SA matrix, resulting in the formation of a stable 3D network where the fillers fit into the cross-linked matrix and ensure efficient load transfer. In

contrast, the addition of Bi_2O_3 reduces the %E value of the SA/Bi_2O_3 composite film mostly due to increase in cross-linking density, which shortens the length of inter-cross-linking chains, limiting the orientation of stretched chains. However, considerable rise in the toughness of the composites with an increase in Bi_2O_3 loading up to 30 wt% was observed indicating that the composites are strongly ductile. The overall tensile characteristics of the SA/Bi_2O_3 composite films were good.

Table 4.1.2. Tensile characteristics of neat and Bi_2O_3 filled SA composites.

Sample	TS (MPa)	YM (GPa)	%E	Toughness (MJ m^{-3})
S0	34.38 ± 2.13	0.74 ± 0.45	11.80 ± 0.89	0.31 ± 0.28
Sca	66.40 ± 2.22	1.27 ± 2.01	10.24 ± 1.31	0.50 ± 0.09
S10B	109.64 ± 3.53	5.78 ± 1.49	9.50 ± 2.56	0.71 ± 0.14
S20B	151.27 ± 1.08	6.47 ± 3.12	9.64 ± 2.77	1.07 ± 0.20
S30B	169.23 ± 4.36	6.74 ± 1.90	8.92 ± 1.78	1.12 ± 0.19
S40B	172.16 ± 3.44	6.96 ± 1.66	4.44 ± 3.21	1.63 ± 0.68

4.1.3 X-/γ-ray attenuation properties of SA/Bi_2O_3

γ-Ray attenuation properties of SA/Bi_2O_3 composites were studied using a well calibrated NaI(Tl) detector spectrometer in the γ-ray energy range of 0.356 – 1.332 MeV. The radioactive point sources used in the present study, ^{133}Ba, ^{22}Na, ^{137}Cs, and ^{60}Co, were all procured from Board of Radiation and Isotope Technology (BRIT), Mumbai, India. Incident (I_0) and transmitted (I) γ-ray intensity measurements were conducted adopting the narrow beam geometry (Figure 4.1.7). γ-Ray attenuation properties of the polymer composites were determined in terms of μ/ρ by measuring the transmitted (I) intensities of γ-rays through various thicknesses of the composites. After the initial adjustments and calibration of the detector, the experimental procedure was standardized using standard reference material, Aluminium (Al), whose μ/ρ values are well-known both experimentally and theoretically. For a given γ-ray source, transmitted intensities of γ-rays were measured by stacking Al foils of varying thickness between the lead collimators. μ/ρ values were determined from the slope of ln(I) versus mass thickness (t, g/cm^2) plots in three trials. The weighted mean value of μ/ρ computed using the three trials was compared with standard theoretical μ/ρ value obtained using PAGEX. This procedure was extended to determine the μ/ρ values of SA-based samples under study. The deviation (Δ%) in experimental μ/ρ values from the PAGEX values was calculated using the following equation,

$$\Delta\% = \left| \frac{\left(\mu/\rho\right)_{avg} - \left(\mu/\rho\right)_{theoretical}}{\left(\mu/\rho\right)_{theoretical}} \right| \times 100 \qquad (4.1.1)$$

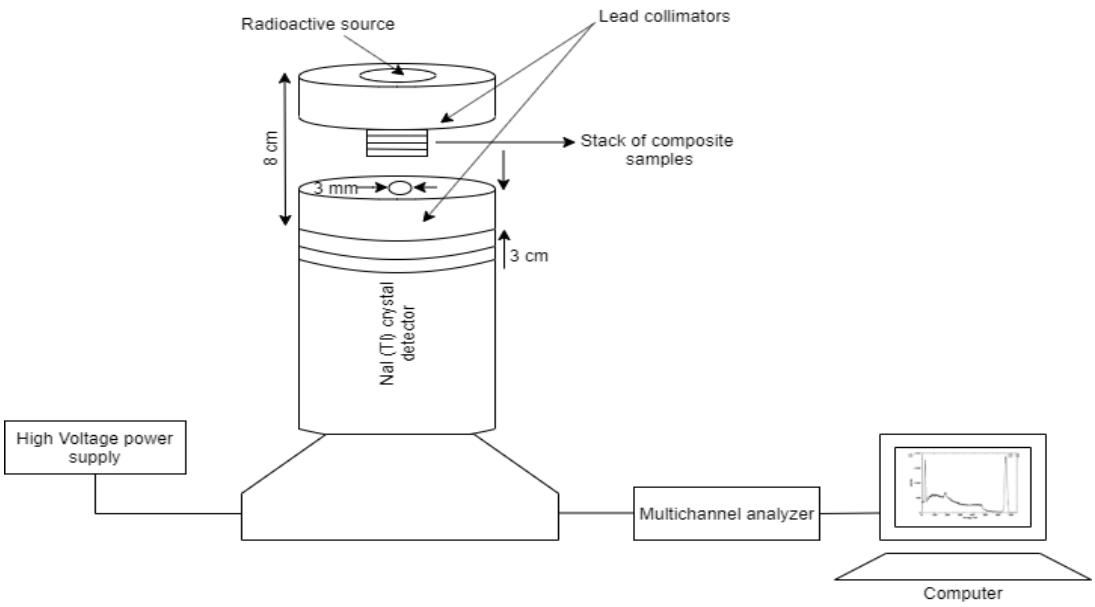

Figure 4.1.7. Schematic diagram of attenuation experimental setup.

For most practical applications, shielding efficiency of the materials are characterized using parameters such as half-value layer (HVL, cm), tenth-value layer (TVL, cm) and relaxation length (λ, cm). HVL is the thickness of a material required to reduce the intensity of the incident γ-rays to half of its original value, whereas TVL is to one tenth of the original intensity of the incident γ-rays. HVL and TVL were determined using following Equations (4.1.2) and (4.1.3) respectively (Biersack and Freeman, 2008),

$$\text{HVL} = \frac{\ln 2}{\mu} = \frac{0.693}{\mu} \tag{4.1.2}$$

$$\text{TVL} = \frac{\ln 10}{\mu} = \frac{2.303}{\mu} \tag{4.1.3}$$

Relaxation length (λ), also called the mean free path, is defined as the material thickness that reduces 36.8% of the incoming γ-rays, and is given by (Stabin, 2007),

$$\lambda = \frac{1}{\mu} \tag{4.1.4}$$

As light-weight materials are mostly desirable for shielding applications, it is essential to have knowledge on their heaviness. Polymer composites are known to be lighter than conventionally used shielding materials such as lead, metals or concrete. Since, lead is the most widely used shielding material, % heaviness of the composites is determined with lead as standard and normalizing its density to 100%. The % heaviness is expressed using the following equation (Ambika et al., 2017),

$$\%\ \text{heaviness} = \frac{\text{Density of material}}{\text{Density of lead}} \times 100 \tag{4.1.5}$$

For mixtures/compounds, atomic number cannot be represented by a single number uniquely in different energy regions as the partial interaction cross-sections show Z dependence. Therefore, an energy-dependent parameter called effective atomic number (Z_{eff}) is used to differentiate different materials based on total interaction probability. Z_{eff} values of polymer composites were calculated using the semi-empirical relation given by the following equation (Russo, 2017),

$$Z_{eff} = \frac{\sigma_a}{\sigma_e} \tag{4.1.6}$$

such that σ_a (b atom^{-1}) is effective (average) cross-section per atom which is given by the following equation (Rao et al., 1985),

$$\sigma_a = \frac{1}{N_A}\frac{(\mu/\rho)_{composite}}{\sum_i w_i/A_i} \tag{4.1.7}$$

where, A_i is the atomic weight of ith constituent element, N_A is the Avogadro's constant and $(\mu/\rho)_{composite}$ is the mass attenuation coefficient of the composites. While, σ_e (b electron^{-1}) is the effective (average) cross-section per electron is given by the following equation,

$$\sigma_e = \frac{\sum_i \frac{f_i A_i (\mu/\rho)_i}{Z_i}}{N_A} \tag{4.1.8}$$

where, Z_i and $(\mu/\rho)_i$ are the atomic number and mass attenuation coefficient of ith element and is the number fraction of ith element. The experimental values of Z_{eff} are obtained by substituting experimentally determined μ/ρ values and $(\mu/\rho)_i$ values computed from WinXCom program (Gerward et al., 2004). On the other hand, theoretical Z_{eff} values are calculated using μ/ρ and $(\mu/\rho)_i$ values, both obtained from WinXCom. Another software, Auto-Z_{eff}, is used to further compute the theoretical values of Z_{eff} and validate the experimental results (Taylor et al., 2012). Effective electron density (N_{eff}, electrons g^{-1}) is another closely related quantity that gives the number of electrons per unit mass of the interacting medium which in turn represents the probability of radiation interaction. N_{eff} can be calculated using the following equation (Russo et al., 2017),

$$N_{eff} = \frac{(\mu/\rho)_{composite}}{\sigma_e} \tag{4.1.9}$$

The densities of the polymer composite films were measured using the principle of hydrostatic weighing in accordance to ASTM D792-00 standard. Thickness of the films were measured using Mitutoyo digital micrometer with accuracy of 0.001 mm.

Experimental μ/ρ values of SA/Bi_2O_3 composites showed good agreement with theoretical values computed using our newly developed PAGEX software in the energy range of 30 – 1332 keV (Table 4.1.3). Also, the μ/ρ values computed using PAGEX well agreed with those from WinXCom. While S0 and SCa have closer values of μ/ρ, significant increase in μ/ρ was observed for SA/Bi_2O_3 composites. With the Bi_2O_3 loading, the packing density of the composites increases and a greater number of Bi attenuator atoms will be available for radiation attenuation. Consequently, SA composites containing 40 wt% Bi_2O_3 (S40B) displayed highest shielding performance among the studied composites. Maximum attenuation was observed at 0.356 MeV which then decreased with increase in energy, for all the samples. Only at lower energies (0.356, 0.511 and 0.662 MeV), the filler loading was found to have significant effect on μ/ρ values. This is probably attributed to variation in dominance of various photon interaction processes in different energy regions.

Table 4.1.3. Experimental (E) and PAGEX (T) μ/ρ values of the composites in the energy range 30 – 1332 keV and relative deviation (Δ%) between them.

E (keV)	S0			SCa			S10B		
	E	T	Δ%	E	T	Δ%	E	T	Δ%
30.85	--	0.357	--	--	0.385	--	--	2.979	--
32.06	--	0.338	--	--	0.363	--	--	2.708	--
35.10	--	0.300	--	--	0.319	--	--	2.170	--
36.35	--	0.288	--	--	0.305	--	--	1.994	--
53.16	--	0.209	--	--	0.214	--	--	0.836	--
80.99	--	0.172	--	--	0.174	--	--	0.377	--
276.40	--	0.114	--	--	0.114	--	--	0.148	--
302.85	--	0.110	--	--	0.110	--	--	0.137	--
356.01	0.105 ± 0.001	0.104	1.156	0.105 ± 0.002	0.104	1.156	0.118 ± 0.003	0.121	2.479
383.85	--	0.101	--	--	0.101	--	--	0.115	--
511.00	0.091 ± 0.002	0.090	1.529	0.091 ± 0.003	0.090	1.563	0.095 ± 0.001	0.096	0.949
661.7	0.081 ± 0.004	0.080	1.149	0.081 ± 0.004	0.080	1.187	0.083 ± 0.001	0.083	0.072
1173.20	0.062 ± 0.003	0.061	1.673	0.062 ± 0.005	0.061	1.723	0.062 ± 0.005	0.061	1.506
1274.40	0.059 ± 0.004	0.058	0.941	0.059 ± 0.007	0.058	0.976	0.059 ± 0.001	0.058	0.976
1332.50	0.058 ± 0.008	0.057	1.523	0.058 ± 0.005	0.057	1.558	0.058 ± 0.002	0.057	1.630
30.85	--	5.573	--	--	8.166	--	--	10.760	--
32.06	--	5.054	--	--	7.399	--	--	9.745	--

Table 4.1.3 Continued.

E (keV)	S20B			S30B			S40B		
	E	T	Δ%	E	T	Δ%	E	T	Δ%
35.10	--	4.021	--	--	5.873	--	--	7.724	--
36.35	--	3.684	--	--	5.374	--	--	7.064	--
53.16	--	1.458	--	--	2.079	--	--	2.701	--
80.99	--	0.581	--	--	0.785	--	--	0.988	--
276.40	--	0.183	--	--	0.217	--	--	0.251	--
302.85	--	0.164	--	--	0.191	--	--	0.217	--
356.01	0.136 ± 0.006	0.138	1.592	0.150 ± 0.005	0.154	2.597	0.169 ± 0.004	0.173	2.142
383.85	--	0.129	--	--	0.143	--	--	0.157	--
511.00	0.100 ± 0.005	0.102	2.153	0.105 ± 0.003	0.109	3.226	0.113 ± 0.010	0.115	1.568
661.7	0.085 ± 0.008	0.086	0.967	0.088 ± 0.009	0.089	0.812	0.090 ± 0.001	0.092	1.757
1173.20	0.062 ± 0.007	0.061	1.307	0.062 ± 0.004	0.061	1.092	0.062 ± 0.002	0.061	0.895
1274.40	0.059 ± 0.008	0.058	0.958	0.059 ± 0.007	0.058	0.958	0.059 ± 0.005	0.058	0.958
1332.50	0.058 ± 0.001	0.057	1.719	0.058 ± 0.003	0.057	1.790	0.058 ± 0.005	0.057	1.862

--: Not available.

HVL and λ values of the composites decreased with increasing Bi_2O_3 content, mostly due to increase in mass thickness of the composites. As lower values of HVL and λ implies higher shielding ability, S40B composites showed better photon attenuation ability. Similar variation was observed with Z_{eff} and N_{eff} values with increasing Bi_2O_3 content as shown in Figure 4.1.8. μ/ρ value of 40 wt% SA/Bi_2O_3 composites (S40B) was compared with that of shielding materials reported in literature (Table 4.1.4). Lead is the reference material because it is the most efficient and widely used shielding material, and it is usually desired to obtain attenuation equivalent to it (Belgin et al., 2015). From Table 4.1.4, it is evident that at any given energy, 40 wt% SA/Bi_2O_3 composites show greater μ/ρ values than stainless steel, barite and concrete (Sharifi et al., 2013; Buyukyildiz et al., 2017). Furthermore, these SA/Bi_2O_3 composites have μ/ρ values comparable to that of polymer composites reported in literature. At all the energies, S40B composites showed relatively higher μ/ρ values than silicone and natural rubber composites which had higher loading of 50 wt% and 500 phr Bi_2O_3, respectively (Toyen et al., 2017; Verdipoor et al., 2018). The enhancement in μ/ρ values for SA/Bi_2O_3 composites in the present study could be due to uniform dispersion of filler and higher density of sodium alginate matrix (1.61 g cm^{-3}) compared to UP (1.2 g cm^{-3}), PVA (1.19 g cm^{-3}), PMMA (1.18 g cm^{-3}) and epoxy (1.2 g cm^{-3}) (Ambika et al., 2017; Muthamma et al., 2019; Cao et al., 2020, Muthamma et al., 2020). We also compared the % heaviness of the neat and SA/Bi_2O_3

composites with standard shielding materials (Figure 4.1.9). In comparison to lead at 100%, barite, steel, and concrete are 37.10, 69.21, and 21.16% heavy, respectively, whereas S40B and S0 are 21.24% and 14.09% heavy, respectively.

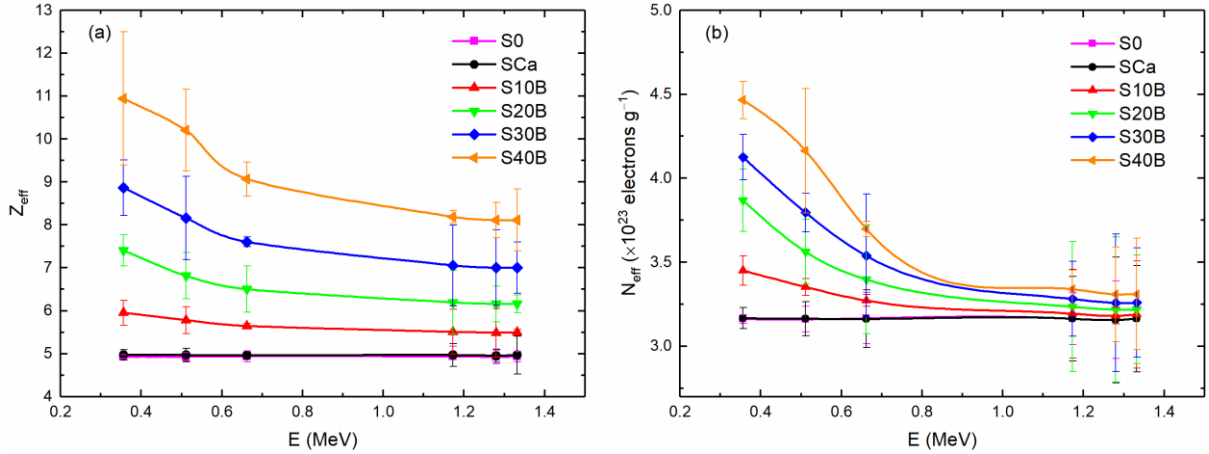

Figure 4.1.8. (a) Z_{eff} and (b) N_{eff} of the composites.

4.1.4 Conclusions

Soft and flexible composite films of SA/Bi_2O_3 were prepared by simple solution casting method. Ca^{2+} ion treatment altered the water sensitivity of SA films, with 1.5 wt% $CaCl_2$ content determined to be optimal for producing robust and hydrophobic films, the effect being attributed to cross-linking. XRD, FTIR and SEM studies confirmed the formation of composites and homogeneous distribution of Bi_2O_3 into polymer matrix. Bi_2O_3 loaded SA films demonstrated decreased water solubility and swelling ratio, suggesting the improved

Table 4.1.4. Comparison of μ/ρ values from the present work with literature.

Material	μ/ρ values (cm^2g^{-1})					
	0.356 MeV	0.511 MeV	0.662 MeV	1.173 MeV	1.332 MeV	1.274 MeV
Lead (Belgin et al., 2015)	---	---	0.100	---	0.056	---
Ordinary concrete (Sharifi et al., 2013)	---	0.088	0.079	---	0.056	---
Barite (Sharifi et al., 2013)	---	0.092	0.078	---	0.052	---
Stainless steel 304L (Buyukyildiz et al., 2017)	0.100	---	0.074	---	0.054	---
UP/60 wt% Bi_2O_3 (Ambika et al., 2017)	0.197	---	0.100	0.057	0.051	---
NR/500 phr Bi_2O_3 (Toyen et al., 2017)	---	---	0.070	0.036 (at 1.25 MeV)		---
Silicone resin/50 wt% Bi_2O_3 (Verdipoor et al., 2018)	0.099	---	0.075	0.055	0.052	---
PVA/40 wt% Bi_2O_3 (Muthamma et al., 2019)	---	---	0.089	---	---	---
PMMA/44 wt% Bi_2O_3 (Cao et al., 2020)	0.105	---	0.066	0.082	0.089	---
Epoxy/35 wt% Bi_2O_3 (Muthamma et al., 2020)	---	---	0.089	---	---	---
SA/40 wt% Bi_2O_3 (This work)	0.169	0.113	0.090	0.062	0.058	0.059

---: Not available.

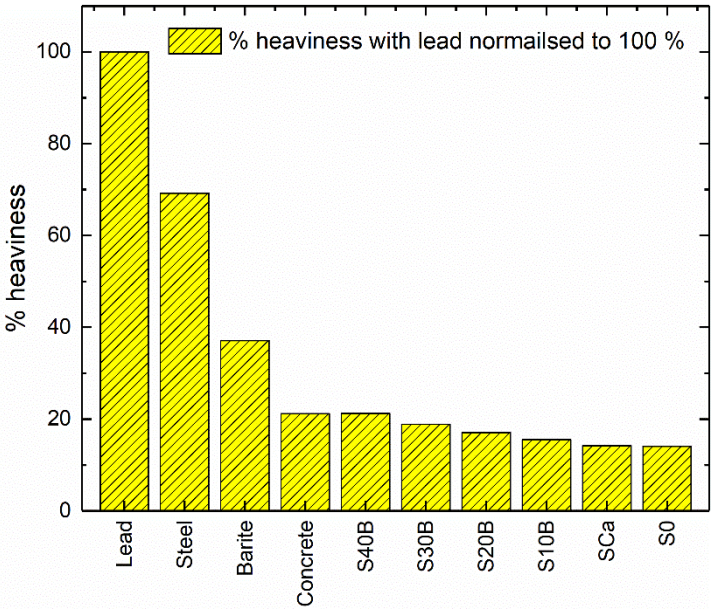

Figure 4.1.9. Comparison of % heaviness.

structural integrity of Bi_2O_3 loaded composite films. The Bi_2O_3 loaded composites showed enhanced tensile strength and Youngs modulus up to 40 wt% loading. Compared to high modulus polymers like epoxy, high density polyethylene (HDPE) and poly (vinyl chloride) (PVC), these exhibit relatively greater extent of stretching before breaking. The 40 wt% Bi_2O_3 loaded films showed good heat resistance with the peak degradation temperature reaching as high as 251 °C. With low values of % heaviness (~ 21 % of that of lead for S40B), these composites are relatively lighter in weight. Attenuation studies using the γ-ray sources (^{137}Cs, ^{60}Co, ^{22}Na and ^{133}Ba) of medical and industrial interest revealed that μ/ρ increased with filler loading and S40B composite with 40 wt% filler content exhibited highest radiation attenuation ($\mu/\rho = 0.169$ cm^2 g^{-1}) for 0.356 MeV photons. The composite films also demonstrated good resistance to most of the laboratory reagents, including acids and organic solvents. Above all, biodegradability of sodium alginate composites is of great benefit to environmental safety. Owing to their non-toxic nature, good thermal and mechanical properties, easy and rapid fabrication possibility, these SA/Bi_2O_3 composites may have potential applications as γ-ray shielding materials in various radiation environments.

This work on SA/Bi_2O_3 composites is published in the *Journal of Applied Polymer Science,* **138**, 50369 (1-19), 2021.

4.2 Micro/nano tantalum (V) oxide filled DGEBA epoxy composites

In this work, we have investigated the synergistic effect of loading micro- and nano-Ta_2O_5 fillers on the thermal, mechanical, viscoelastic and radioprotective properties of DGEBA epoxy resin-based composites. We have compared all the above-mentioned properties of the epoxy

composites as function of Ta_2O_5 filler loading and filler size. Further details of this study are described in the following sections.

4.2.1 Materials and synthesis

Commercial grade epoxy Araldite LY556 (MW = 320.813 g mol^{-1}; ρ = 1.20 g cm^{-3}) and hardener Aradur HY951 (MW = 146.238 g mol^{-1}), chemically called triethylenetetramine (TETA), were procured from S & S Polymers, Bengaluru, India. Tantalum (V) oxide (99.99%) (MW = 441.893 g mol^{-1}; ρ = 8.20 g cm^{-3}) micro powder was procured from Research Laboratory, Bengaluru, India, while tantalum (V) oxide nano powder having average particle size (APS) of 80 nm was supplied by Nanoshel LLC, India.

Room temperature solution casting technique was employed to synthesize neat and Ta_2O_5 filled epoxy composite films as shown in Figure 4.2.1. The neat epoxy sample is designated as E0 while microcomposites are named E(x)mT and nanocomposites as E(x)nT in general, where x, mT and nT represent the filler concentration (wt%), micro-Ta_2O_5 fillers and nano-Ta_2O_5 fillers, respectively.

4.2.2 Structural, thermo-mechanical and viscoelastic properties of m-Ta_2O_5/epoxy and n-Ta_2O_5/epoxy composites

The formation of epoxy composites was confirmed structurally by XRD and FTIR spectra, for neat epoxy, m-Ta_2O_5/epoxy and n-Ta_2O_5/epoxy composites at 10 wt% filler loading, as shown in Figure 4.2.2a and b respectively. Neat epoxy showed broad XRD peak at 2θ = 18°, due to scattering from cured epoxy molecules, revealing its amorphous nature. With filler addition, the sharp characteristic peaks that appeared at 2θ = 22.84°, 28.40°, 36.74°, 46.75°, 50.70°, 55.68°, 58.44° and 63.87° correspond to (001), (1110), (1111), (002), (2151), (1112), (2200) and (2221) planes, respectively of orthorhombic phase of β-Ta_2O_5 (PDF 00-025-0922 with lattice parameters a = 6.1980 Å, b = 40.2900 Å, c = 3.8880 Å, and $\alpha = \beta = \gamma = 90°$ for the spatial group $P2_12_12$). For nanocomposites, XRD peaks were observed to be slightly broader and less sharp compared to their micro counterparts, denoting the increase in lattice strain and decrease in crystallinity of the samples. In general, XRD of the samples revealed that added Ta_2O_5 fillers did not alter the structure of epoxy matrix. Similar results were observed in the FTIR spectrum. All the peaks corresponding to various functional groups characteristic of cured neat epoxy was observed (Figure 11b). The two additional peaks at 830.11 and 680.05 cm^{-1} correspond to stretching vibrations of Ta-O-Ta and Ta-O bonds of Ta_2O_5 respectively, indicating the formation of desired composites. These peaks for nanocomposites were relatively broader and less intense, suggesting decrease in filler size. With increase in filler

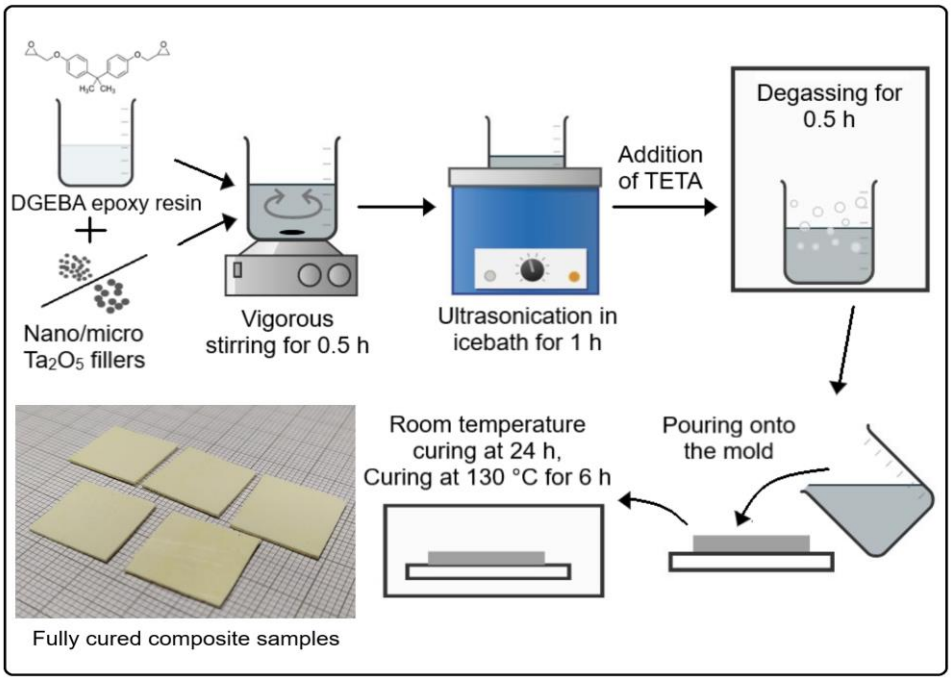

Figure 4.2.1. Schematic illustration of the preparation of micro/nano - Ta_2O_5 epoxy composite films.

loading, the intensity and width of the hump at ~ 3400 cm^{-1} in neat epoxy, which corresponds to stretching vibrations of -OH group, is observed to increase. This is due to the interaction of free -OH or -OH groups attached to absorbed/adsorbed water molecules on the surface of fillers with the polar groups of epoxy resin, resulting in hydrogen bonding formation. The 10 wt% n-Ta_2O_5 composites, in particular, show a broader and deeper hump than their micro counterparts, indicating a greater number of -OH groups on the nanofiller surface. Metal-oxide (Ta-O) bonds develop and intensify with filler loading, implying that the additional Ta_2O_5 is grafted onto the epoxy chain backbone, forming composites.

SEM images of epoxy composites with m-Ta_2O_5 loading are given in Figures 4.2.3(a-c). All the images depict fairly uniform distribution of the micro-sized spherical Ta_2O_5 fillers. Average particle size was found to be 4.18 µm as determined using ImageJ software. While Figures 4.2.3(d-i) show the SEM images of epoxy composites with n-Ta_2O_5 loading. Spherical Ta_2O_5 nanoparticles with average particle size of 75.01 nm are uniformly distributed throughout the epoxy matrix. The fraction of surface Ta atoms appear to increase with the increase in Ta_2O_5 loading from 10 – 30 wt%, irrespective of the filler size.

TGA curves of all epoxy composites showed sharp one-stage thermal decomposition implying that the inclusion of Ta_2O_5 fillers, regardless of size, has not significantly affected the epoxy

matrix degradation mechanism. Thermal properties in terms of $T_{10\%}$, $T_{50\%}$, T_p and R_{max} are presented in Table 4.2.1. Increase in the values of $T_{10\%}$, $T_{50\%}$, T_p with Ta_2O_5 loading, irrespective of filler size, suggests an enhancement in thermal properties of epoxy matrix. However, the enhancement in thermal stability is more prominent in nanocomposites compared

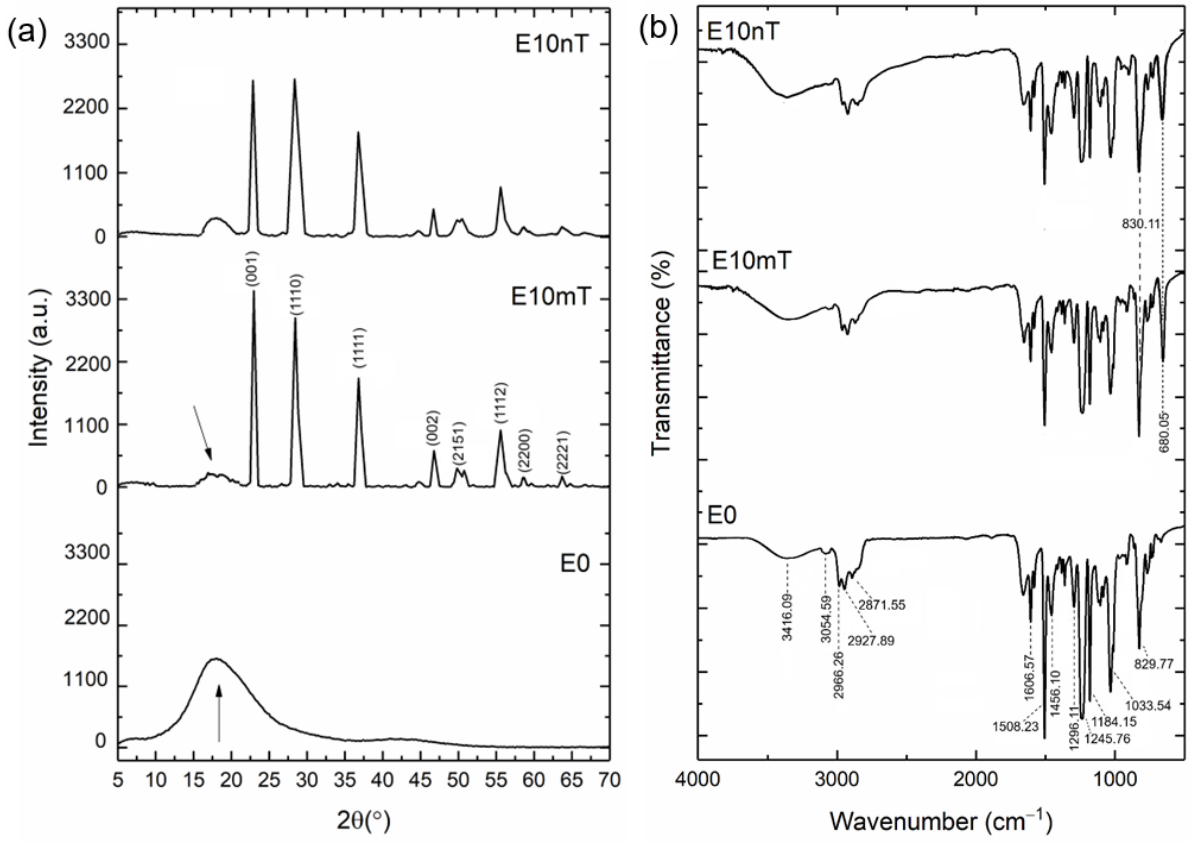

Figure 4.2.2. Representative (a) XRD and (b) FTIR spectra neat (E0), 10 wt% micro-Ta_2O_5 (E10mT) and 10 wt% nano-Ta_2O_5 (E10nT) loaded DGEBA epoxy composites.

to micro-composites at a given loading. This could be attributed to several reasons. Nanofillers agglomerate more quickly on the molten matrix surface than micro-fillers during thermal decomposition, forming a physical barrier that impedes the thermo-oxidative degradation process. Because nanofillers are smaller in size than micro-fillers, the mean distance between aggregates is reduced significantly, resulting in a more effective barrier against oxygen diffusion. Second, the inclusion of fillers considerably lowers the molecular mobility of degradation products and macro chain fragments, with nano-sized fillers having a greater effect due to their high surface-to-volume ratio (Majka et al., 2016). As a result, the higher thermal stability of nanocomposites might be attributed to the slowing of molecular dynamics, physical cross-linking, or particular interactions between distinct components of the composite system.

Reduced volatile fraction of epoxy resin with increased Ta_2O_5 concentration and high melting point (1872 °C) of Ta_2O_5 fillers might also be responsible for the composites' improved thermal stability.

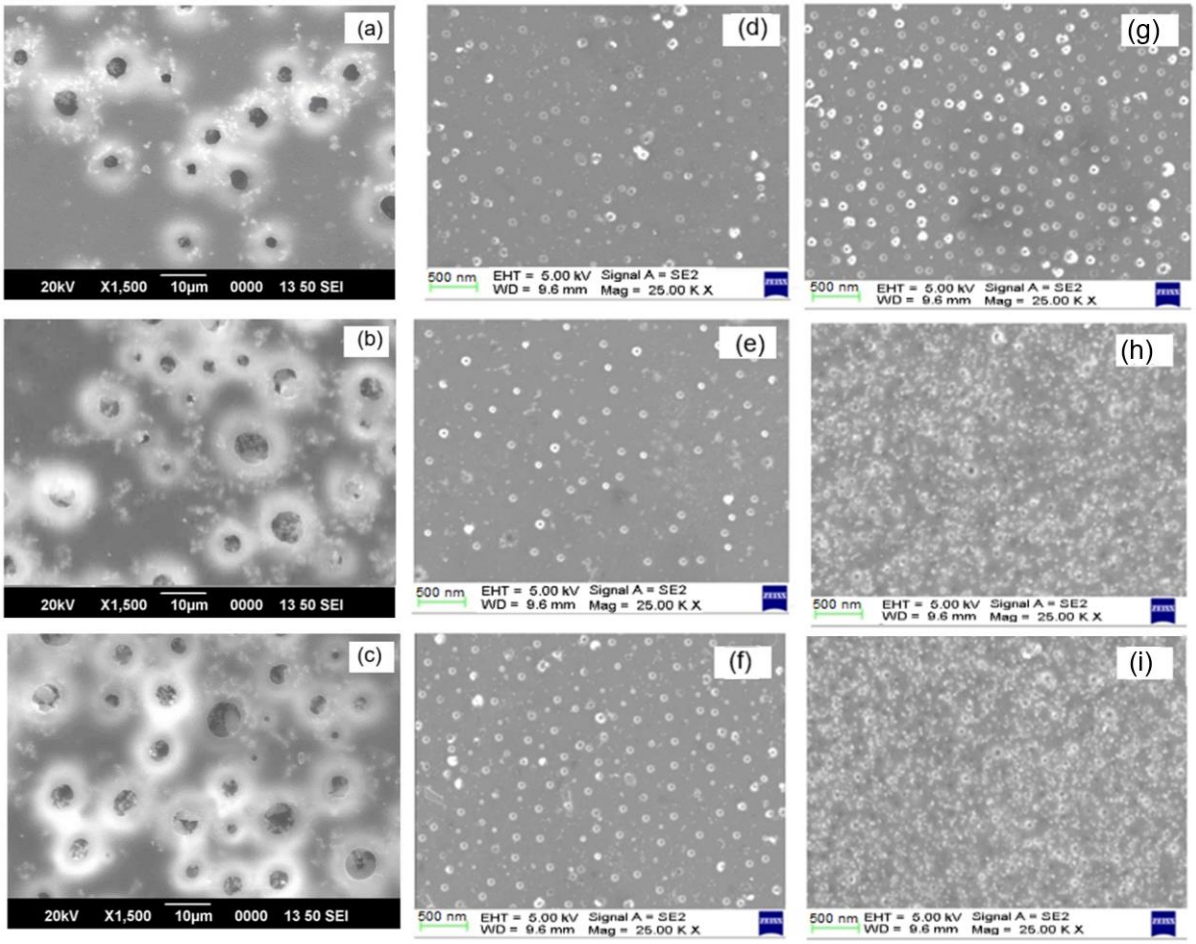
(a)
20kV X1,500 10µm 0000 13 50 SEI
(d)
500 nm EHT = 5.00 kV Signal A = SE2 WD = 9.6 mm Mag = 25.00 K X
(g)
500 nm EHT = 5.00 kV Signal A = SE2 WD = 9.6 mm Mag = 25.00 K X
(b)
20kV X1,500 10µm 0000 13 50 SEI
(e)
500 nm EHT = 5.00 kV Signal A = SE2 WD = 9.6 mm Mag = 25.00 K X
(h)
500 nm EHT = 5.00 kV Signal A = SE2 WD = 9.6 mm Mag = 25.00 K X
(c)
20kV X1,500 10µm 0000 13 50 SEI
(f)
500 nm EHT = 5.00 kV Signal A = SE2 WD = 9.6 mm Mag = 25.00 K X
(i)
500 nm EHT = 5.00 kV Signal A = SE2 WD = 9.6 mm Mag = 25.00 K X

Figure 4.2.3. SEM images of m-Ta_2O_5 and n-Ta_2O_5 filled DGEBA epoxy composite films.

Tensile properties of epoxy-based samples were studied using Instron 8502 Servo-hydraulic UTM according to ASTM D638 Type V dimension (suitable standard for rigid samples < 4 mm thickness) and are presented in Table 4.2.2. The stress-strain curves of epoxy composites indicated their brittle fracture nature via linear growth until breaking point. Regardless of filler size, the addition of Ta_2O_5 enhanced the TS and YM of composites. However, at a given loading, the TS and YM of nanocomposites are significantly greater than those of microcomposites. This is due to the fact that an increase in filler loading and a decrease in filler size are followed by a decrease in filler distance, resulting in a large number of barriers against grain boundary motions, constraining their movement, which would otherwise make the material weaker. This increase might possibly be ascribed to hydrogen bonding between free hydroxyl groups on the n-Ta_2O_5 filler surface and the epoxy matrix, as revealed in FTIR spectra, which improves interfacial adhesion and uniform stress transmission between the two

Table 4.2.1. Thermal properties of neat and Ta_2O_5 filled epoxy composites.

Sample	$T_{10\%}$ (°C)	$T_{50\%}$ (°C)	T_p (°C)	R_{max} (% °C^{-1})
E0	389.19	435.12	420.30	–1.109
E10mT	393.68	441.15	423.97	–1.049
E20mT	401.71	454.04	429.47	–0.918
E30mT	406.37	466.52	430.21	–0.794
E3nT	390.56	437.08	420.80	–1.074
E6nT	393.13	440.78	423.04	–1.037
E10nT	396.49	446.22	425.29	–0.986
E13nT	398.07	448.69	426.60	–0.962
E16nT	401.63	454.37	428.84	–0.912
E20nT	404.39	459.55	430.15	–0.866
E23nT	406.37	463.50	431.27	–0.832
E26nT	407.55	468.19	431.27	–0.788
E30nT	408.74	472.35	431.33	–0.726

Table 4.2.2. Tensile properties of neat and Ta_2O_5 filled epoxy composites.

Sample	TS (MPa)	YM (GPa)	% E	Toughness (MJ m^{-3})
E0	85.07	2.51	4.01	1.88
E10mT	189.05	3.96	3.45	3.60
E20mT	324.96	6.36	2.96	5.31
E30mT	535.80	11.01	2.64	7.80
E3nT	175.26	2.60	3.69	3.57
E6nT	197.63	2.70	3.57	3.89
E10nT	236.27	3.38	3.34	4.35
E13nT	260.67	4.09	3.11	4.47
E16nT	295.25	4.96	2.96	4.82
E20nT	356.26	5.95	2.92	5.74
E23nT	411.17	7.04	2.88	6.53
E26nT	443.71	8.00	2.77	6.78
E30nT	575.90	11.38	2.59	8.23

phases. The higher modulus (175 - 190 GPa) of Ta accounts for the increase in YM of composites. The incorporation of such high stiffness fillers into the matrix improved the fracture toughness of the composites, as evidenced by an increase in the area under the stress-strain curves with filler loading. The fact that there is a systematic decrease in %E with Ta_2O_5 loading indicates that the fillers resist deformation when the matrix tries to stretch under increasing stress, and so the filled composites have slightly less deformation than plain epoxy. Unlike TS and YM, the values of %E for m-Ta_2O_5/epoxy composites are better than that of n-

Ta_2O_5/epoxy at similar loading. Nonetheless, nanocomposites with minimal loading demonstrated tensile characteristics comparable to fully loaded micro composites.

The viscoelastic properties of the epoxy-based samples were studied using dynamic mechanical analysis (DMA), performed on TA-Q800 Instrument at a fixed frequency of 1 Hz from room temperature to 250 °C at a linear heating rate of 5 °C min^{-1} on the samples of dimension 35 mm × 12.8 mm × 2.8 mm. DMA curves were analysed to assess the structural changes in composites such as degree of cross-linking density (N), matrix-filler interfacial bonding given by adhesion factor (A), effectiveness of filler reinforcement (C-factor), glass transition temperature (T_g) and damping (tan δ) using the Eqs (4.2.1) to .(4.2.3). The 'C-factor' which gives the relative measure of the decrease in modulus on increase in temperature as the material passes through its glass transition is given by following equation (Jyoti et al., 2016),

$$C = \frac{\left(E'_g / E'_r\right)_{composites}}{\left(E'_g / E'_r\right)_{neat\ polymer}} \tag{4.2.1}$$

where, E'_g and E'_r are the values of storage modulus in glassy and rubbery regions, respectively. The extent of cross-linking between fillers and the matrix is expressed in terms of degree of entanglement density (N) using the following equation (Jyoti et al., 2016),

$$N = \frac{E'}{6RT} \tag{4.2.2}$$

where, E' is the storage modulus in the rubbery plateau region, R is the universal gas constant and T is the absolute temperature. On the other hand, the efficiency of adhesion between the fillers and the matrix was determined by adhesion factor (A) given by following equation (Jyoti et al., 2016),

$$A = \frac{1}{1-V_f}\left(\frac{\tan\delta_c}{\tan\delta_p}\right) - 1 \tag{4.2.3}$$

Where $\tan\delta_c$ and $\tan\delta_p$ is the relative damping of composite and neat polymer, respectively and V_f is volume fraction of fillers in the composite.

Various viscoelastic parameters as determined from DMA curves are presented in Table 13. The variation of storage modulus (E′) with temperature is given in Figures 4.2.4(a) and (b), and the viscoelastic parameters evaluated at 1 Hz oscillation frequency are presented in Table 4.2.3. All the composites showed similar variation in E′ with temperature. E′ curves show three distinct regions, representing a high modulus glassy region (below 110 °C), a transition zone (110-140 °C) a plateau in rubbery region (above 140 °C). E′ of filled composites have increased with increase in filler loading from 10-30 wt%, which may be attributed to the

restriction in molecular mobility of the epoxy polymer chains by presence of fillers. However, the enhancement in viscoelastic properties of nanocomposites is considerably higher compared to micro composites. This could be probably attributed to the fact that nano-Ta_2O_5 with higher surface-to-volume ratio than micro-Ta_2O_5 provide better interfacial interactions with the matrix. A lower value of C indicates more stress transfer between filler and the matrix, since modulus in the glassy state is determined primarily by the strength of intermolecular forces and the way the polymer chains are packed (Table 4.2.3). C-factor was observed to be lowest for E30nT composite. The higher the value of N, higher is the interfacial adhesion. N values have increased with Ta_2O_5 loading, irrespective of filler size, suggesting good interfacial adhesion even at 30 wt% nanofiller loading.

Figures 4.2.4(c) and (d) illustrate the temperature dependence of damping factor (tan δ) for neat and filled epoxy composites. The decrease in the height of tan δ peaks of composites compared to that of neat epoxy resin could be probably attributed to the stiffening effect due to physical and chemical adsorption of epoxy chains on filler surface. Such a decrease also proves a minimum heat build-up in the filled composites indicating restriction in damping characteristics of the composites. A lower value of tanδ at T_g indicates better interfacial adhesion between filler and the matrix. In the present study, E30nT composite has showed the lowest value of tanδ.

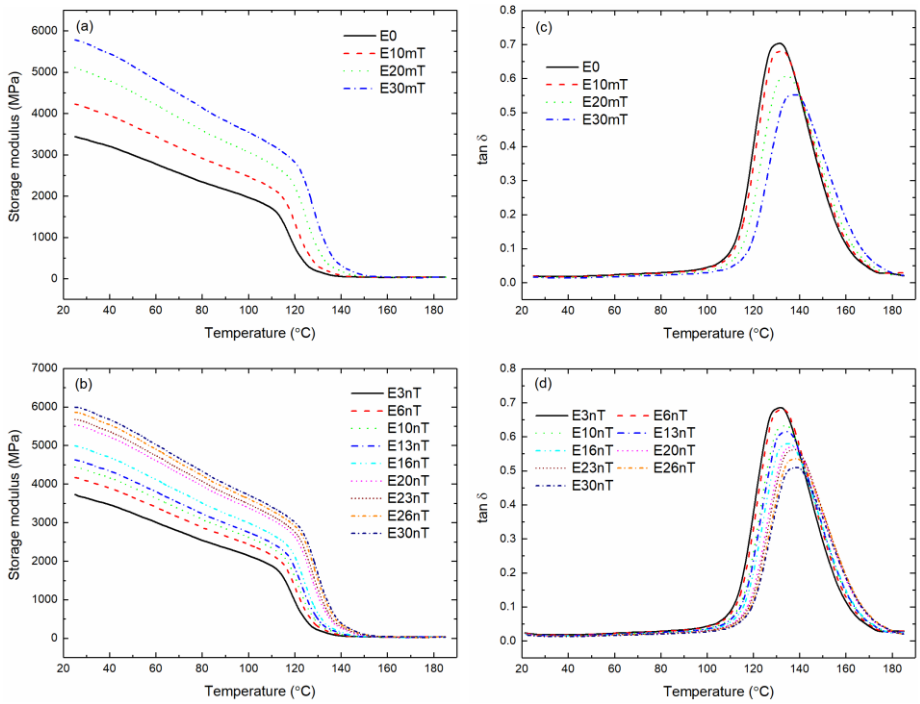

Figure 4.2.4. Variation of storage modulus of (a) m-Ta_2O_5/epoxy and (b) n-Ta_2O_5/epoxy composites, damping curves of (c) m-Ta_2O_5/epoxy and (d) n-Ta_2O_5/epoxy composites.

Table 4.2.3. Thermo-mechanical properties of neat and Ta_2O_5 filled epoxy composites.

Sample	E′ (MPa)		C-factor	N (at 150 °C) (mol m^{-3})	T_g (°C)	tanδ at T_g	A
	Glassy region	Rubbery region (at 150 °C)					
E0	3441.551	33.227	--	1574.670	131.418	0.703	--
E10mT	4225.821	38.998	1.046	1848.165	132.404	0.681	– 0.016
E20mT	5110.406	47.654	1.035	2258.384	134.703	0.606	– 0.106
E30mT	5786.202	55.164	1.013	2614.292	137.989	0.554	– 0.162
E3nT	3734.572	34.58	1.043	1638.790	131.746	0.686	– 0.020
E6nT	4167.654	38.789	1.037	1838.260	132.732	0.681	– 0.022
E10nT	4439.875	41.449	1.034	1964.321	134.046	0.633	– 0.085
E13nT	4625.481	43.224	1.033	2048.440	134.572	0.615	– 0.106
E16nT	4984.320	46.997	1.024	2227.248	135.360	0.580	– 0.152
E20nT	5541.138	53.228	1.005	2522.543	137.332	0.571	– 0.158
E23nT	5677.249	54.676	1.002	2591.165	137.989	0.563	– 0.164
E26nT	5862.855	57.001	0.993	2701.350	138.646	0.536	– 0.198
E30nT	5998.966	60.884	0.951	2885.370	138.712	0.510	– 0.229

--: values not available.

4.2.3 X-/γ-ray attenuation properties of m-Ta_2O_5/epoxy and n-Ta_2O_5/epoxy composites

Experimental and PAGEX μ/ρ values for the microcomposites and experimental μ/ρ values for nanocomposites for 10, 20 and 30 wt% Ta_2O_5 loadings, determined in wide energy range 30 – 1332 keV, are presented in Table 4.2.4 along with density and relative enhancement rate (δ%) in radiation shielding. The relative enhancement rate (δ%) in shielding efficiency of nanocomposites over microcomposites is given by the following,

$$\delta\% = \left| \frac{\left(\mu/\rho\right)_{\text{nano}} - \left(\mu/\rho\right)_{\text{micro}}}{\left(\mu/\rho\right)_{\text{micro}}} \right| \times 100 \qquad (4.2.4)$$

Experimental and theoretical μ/ρ values are in good agreement with each other. Irrespective of Ta_2O_5 filler size, μ/ρ values increased with increase in filler content for both micro- and nanocomposites and decreased with photon energy. The addition of high-ρ (= 8.2 g cm^{-3}) and high-Z Ta_2O_5 fillers to a low density DGEBA (ρ = 1.2 g cm^{-3}) matrix increases the packing density, enhancing the probability of radiation-matter interaction. However, for the same filler loading and energy, nanocomposites have much higher μ/ρ values than their micro counterparts. In fact, n-Ta_2O_5 composites at low loading offered shielding performance comparable to highly loaded micro-composite systems. The number of nanoparticles per volume percent of filler is substantially larger, and their inter-particle distances are much smaller, than the number of microparticles. As a result, the empty spaces/voids via which photons can enter are limited, resulting in increased photon attenuation. Another interesting

Table 4.2.4. Experimental (E) and PAGEX (T) values of μ/ρ, density, relative increase rate (δ%) for neat epoxy, m-Ta_2O_5/epoxy and n-Ta_2O_5/epoxy composites.

E (keV)	Neat epoxy		10 wt% Ta_2O_5 loading			
	E	T	E_{micro}	E_{nano}	T	δ%
30.85	--	0.279	--	--	1.785	--
32.06	--	0.269	--	--	1.628	--
35.10	--	0.249	--	--	1.317	--
36.35	--	0.243	--	--	1.215	--
53.16	--	0.198	--	--	0.550	--
80.99	--	0.173	--	--	0.712	--
276.40	--	0.118	--	--	0.137	--
302.85	--	0.114	--	--	0.129	--
356.01	0.109 ± 0.001	0.107	0.119 ± 0.003	0.131 ± 0.001	0.116	10.084
383.85	--	0.104	--	--	0.112	--
511.00	0.094 ± 0.002	0.093	0.096 ± 0.001	0.107 ± 0.003	0.096	11.458
661.7	0.084 ± 0.003	0.083	0.086 ± 0.007	0.093 ± 0.007	0.084	8.140
1173.20	0.064 ± 0.001	0.063	0.064 ± 0.005	0.069 ± 0.007	0.063	7.813
1274.40	0.060 ± 0.007	0.061	0.061 ± 0.002	0.065 ± 0.002	0.060	6.557
1332.50	0.059 ± 0.004	0.059	0.059 ± 0.003	0.063 ± 0.003	0.059	6.780

E (keV)	20 wt% Ta_2O_5 loading				30 wt% Ta_2O_5 loading			
	E_{micro}	E_{nano}	T	δ%	E_{micro}	E_{nano}	T	δ%
30.85	--	--	3.320	--	--	--	4.883	--
32.06	--	--	3.013	--	--	--	4.424	--
35.10	--	--	2.404	--	--	--	3.512	--
36.35	--	--	2.206	--	--	--	3.215	--
53.16	--	--	0.908	--	--	--	1.272	--
80.99	--	--	1.262	--	--	--	1.821	--
276.40	--	--	0.156	--	--	--	0.176	--
302.85	--	--	0.144	--	--	--	0.159	--
356.01	0.127 ± 0.006	0.142 ± 0.003	0.126	11.811	0.136 ± 0.005	0.154 ± 0.004	0.135	13.235
383.85	--	--	0.119	--	--	--	0.126	--
511.00	0.101 ± 0.002	0.110 ± 0.002	0.098	8.911	0.103 ± 0.004	0.114 ± 0.002	0.101	10.680
661.7	0.086 ± 0.008	0.095 ± 0.006	0.085	10.465	0.087 ± 0.006	0.096 ± 0.001	0.086	10.345
1173.20	0.064 ± 0.004	0.069 ± 0.009	0.062	7.813	0.063 ± 0.003	0.069 ± 0.005	0.062	9.524
1274.40	0.061 ± 0.007	0.065 ± 0.005	0.060	6.557	0.061 ± 0.008	0.065 ± 0.009	0.059	6.557
1332.50	0.059 ± 0.007	0.063 ± 0.001	0.058	6.780	0.059 ± 0.002	0.063 ± 0.004	0.058	6.780

--: Not available.

finding was that the relative enhancement in shielding (δ%) increased with Ta_2O_5 loading at a given energy, whereas δ% decreased with energy at a given loading. At low energies, γ-ray photons interact with Ta atoms via photoelectric effect, but at intermediate energies (0.511 and 0.662 MeV), photoelectric effect and Compton scattering coexist.

However, at higher energies (1.173, 1.274, and 1.332 MeV), photon interactions happen mostly by Compton scattering, which is least affected by the interacting medium's atomic number. At 0.356 MeV, E30nT had the best shielding performance (13.235%) and relative shielding increase. Beyond 20 wt% n-Ta_2O_5 loading, the distribution tends to be unvarying, leaving no interstitial gaps or voids in composites, assuring the existence of a sufficient number of Ta atoms for efficient radiation attenuation. The decrease in δ% with photon energy, on the other hand, is most likely attributable to the fact that the size impact becomes weak due to the dominance of interaction processes. These findings show that using nano-scaled fillers in lower quantities than their micro-counterparts can significantly improve radiation attenuation, with the impact being most noticeable at low energies.

μ/ρ value of 30 wt% n-Ta_2O_5/epoxy composites (E30nT) were compared with that of traditionally used materials and polymer composites reported in literature (Table 4.2.5). From Table 4.2.5, it is evident that our E30nT composites shows μ/ρ values comparable to stainless steel, barite and concrete. Interestingly, at any given energy, E30nT composites have higher μ/ρ values than the polymer composites containing PbO at same or higher loading (≥ 30 wt%), which can be related either to difference in densities of composites or size of fillers (Harish et al., 2009; Bagheri et al., 2018). At all the energies, E30nT composites outperform silicone resin composites loaded with 50 wt% nanofillers of each of PbO, WO_3 and Bi_2O_3 (Verdipoor et al., 2018). However, the μ/ρ values of E30nT composites, with Ta_2O_5 of average size 75 – 80 nm, are just on par with the 14 wt% nano-Bi_2O_3 (20 nm) reinforced epoxy systems (Muthamma et al., 2021). Fillers with a smaller size, greater atomic number, and higher density play a key role in improving radiation attenuation efficiency.

4.2.4 Conclusions

We systematically investigated the influence of micro- and nano-Ta_2O_5 loading on the structural, morphological, thermal, tensile, thermo-mechanical, viscoelastic and γ-ray shielding properties of DGEBA epoxy resin composites. While XRD and FTIR analysis have confirmed the formation of composites with no change in the original structure of epoxy matrix, microstructural analysis revealed uniform dispersion of fillers in the matrix. Nano-Ta_2O_5

Table 4.2.5. Comparison of μ/ρ values at various energies of γ-rays.

Material	μ/ρ (cm^2 g^{-1})					
	0.356 MeV	0.511 MeV	0.662 MeV	1.274 MeV	1.173 MeV	1.332 MeV
Lead (Belgin and Aycik, 2015)	--	--	0.100	--	--	0.056
Ordinary concrete (Sharifi et al., 2013)	--	0.088	0.079	--	--	0.056
Barite (Sharifi et al., 2013)	--	0.092	0.078	--	--	0.052
Stainless steel 304L (Büyükyıldız et al., 2017)	0.100	--	0.074	--	--	0.054
50 wt% PbO/UP (Harish et al., 2009)	--	--	0.095	--	--	--
50 wt% n-WO_3/E44 (El-Toony et al., 2020)	0.126	--	0.078	--	0.036	0.038
500 phr W_2O_3/Natural rubber (Toyen et al., 2018)	--	--	0.056	--	0.029*	
500 phr Bi_2O_3/Natural rubber (Toyen et al., 2017)	--	--	0.070	--	0.036*	
30 wt% PbO/Nanoclay/UP (Bagheri et al., 2018)	--	--	0.084	--	0.031*	
50 wt% n-WO_3/Silicone resin (Verdipoor et al., 2018)	0.110	--	0.084	--	0.065	0.060
50 wt% n-Bi_2O_3/Silicone resin (Verdipoor et al., 2018)	0.110	--	0.084	--	0.065	0.061
50 wt% n-PbO/Silicone resin (Verdipoor et al., 2018)	0.110	--	0.085	--	0.065	0.060
50 wt% Bi_2O_3/PVA (Muthamma et al., 2019)	--	--	0.092	--	--	--
70 wt% W/PEEK composites (Wu et al., 2020)	--	--	0.060	--	0.042*	
50 wt% WO_3/PVA (Muthamma et al., 2020)	--	--	0.088	--	--	--
30 wt% Ta_2O_5/Epoxy (Muthamma et al., 2020)	--	--	0.084	--	--	--
40 wt% Bi_2O_3/Sodium alginate (Prabhu et al., 2021)	0.169	0.113	0.090	0.059	0.062	0.058
14 wt% n-Bi_2O_3/Epoxy (Muthamma et al., 2021)	0.150	0.112	0.094	0.063	0.069	0.060
30 wt% n-Ta_2O_5/Epoxy (Present study)	0.154	0.114	0.096	0.065	0.069	0.063

-- : values not available, * : value at 1.250 MeV

epoxy composites have shown significantly higher thermal stability, flame-retardance and tensile properties compared to micro-composites at same loading. The overall enhancement in material properties of nanocomposites was predominant at low nano-loading (10 wt%). At 10 wt% n-Ta_2O_5 loading, an enhancement in tensile strength of around 25% has been observed compared to its micro-counterpart, while at 30 wt% loading there has been only 8% enhancement. DMA studies have shown overall improvement in visco-elastic properties of epoxy nanocomposites, indicating good matrix-filler interfacial adhesion and better dispersion of nano fillers compared to micro fillers in the matrix. γ-Ray attenuation studies performed in

the energy range of 0.356 – 1.332 MeV revealed better γ-ray shielding ability of nanocomposites compared to microcomposites at same weight fraction of fillers. In particular, γ-ray attenuation at 0.356 MeV for 30 wt% nano-Ta_2O_5 loaded epoxy composite was enhanced by around 13% compared to the microcomposites at the same loading. Thus, n-Ta_2O_5/epoxy composites are found to be promising human safe γ-ray shielding materials.

This work on m-Ta_2O_5/n-Ta_2O_5/Epoxy composites is published in the *Journal of Applied Polymer Science*, **138**, 51289 (1-16), 2021.

4.3 Bismuth (III) oxide decorated graphene oxide filled DGEBA epoxy nanocomposites

In this study, bismuth (III) oxide (Bi_2O_3) decorated graphene oxide (GO) nanocomposites were employed as novel radioprotective fillers in the epoxy polymer matrix. The correlation between surface decoration, filler size and loading, dispersion and interfacial adhesion between matrix-filler phase was systematically examined as function of structural, thermo-mechanical, viscoelastic and radiation shielding properties of the composites. The details of this study are discussed in the following sections.

4.3.1 Materials and synthesis

Multi-stage technique was employed to decorate Bi_2O_3 on the surface of GO to form Bi_2O_3 decorated GO nanocomposites, abbreviated as BGO. First, GO was synthesized by Improved Hummers method (Chen et al., 2013) and BGO nanocomposite was synthesized employing the procedure described by Hashemi et al. (2018). Thereupon, BGO was loaded into DGEBA epoxy resin at different concentrations (5, 10 and 15 wt%) using solution casting technique to form epoxy nanocomposites (Figure 4.3.1).

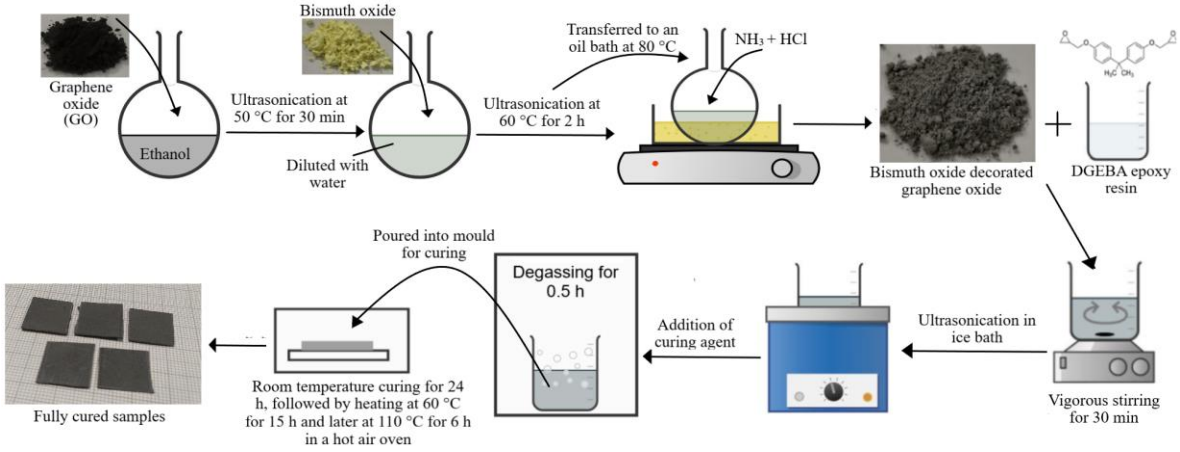
Graphene oxide (GO)
Ethanol
Ultrasonication at 50 °C for 30 min
Bismuth oxide
Diluted with water
Ultrasonication at 60 °C for 2 h
Transferred to an oil bath at 80 °C
NH3 + HCl
Bismuth oxide decorated graphene oxide
DGEBA epoxy resin
Vigorous stirring for 30 min
Ultrasonication in ice bath
Addition of curing agent
Degassing for 0.5 h
Poured into mould for curing
Room temperature curing for 24 h, followed by heating at 60 °C for 15 h and later at 110 °C for 6 h in a hot air oven
Fully cured samples

Figure 4.3.1. Schematic illustration of the preparation of BGO/epoxy nanocomposite films.

4.3.2 Structural and thermal properties of BGO nanocomposites

The formation of BGO nanocomposites was confirmed via XRD, FTIR, Raman spectroscopy, SEM-EDX and thermal analysis. The XRD of Bi_2O_3, GO and BGO composite is presented in Figure 4.3.1. Pure GO has a broad and characteristic peak at lower diffraction angle of 2θ = 11.20°, which corresponds to (001) plane with d-spacing of 0.789 nm. Bi_2O_3 shows multiple sharp and intense peaks consistent with the monoclinic α-phase. While the XRD pattern of BGO displays all the XRD peaks due to α-Bi_2O_3, these peaks are slightly broadened probably due to bridging of Bi_2O_3 with the functional groups between GO layers. The disappearance of stacking GO peak in BGO could be explained by its low content. It is also an indication that bridging of Bi_2O_3 to GO layers would lead to exfoliation of GO and destruction of their regular stacking. Such an XRD further demonstrates that the decoration of Bi_2O_3 on GO surface neither results in development of new crystal phases of Bi_2O_3 nor does it modify the preferential orientations of the α-Bi_2O_3 needles.

Raman spectra were obtained using Bruker RFS 27 MultiRAM FT Raman spectrometer working at 1064 nm wavelength in the wavenumber range 50 – 3000 cm^{-1}. Figures 4.3.3a and b shows the FTIR and Raman spectra, respectively, of Bi_2O_3, GO and BGO composite. FTIR spectrum of Bi_2O_3 shows sharp bands in the frequency region of 500 – 900 cm^{-1} all of which are attributed to stretching vibrations of each type of Bi-O bond (Figure 4.3.3a). For GO, the broad peak around ~3407 cm^{-1} is due to stretching vibrations of hydroxyl and residual water between the GO sheets. The peak at 2976 cm^{-1} is caused by asymmetric CH_2 stretching vibrations of GO. The peaks at 1728 and 1624 cm^{-1} are ascribed to carboxyl/carbonyl (C=O) stretching vibrations and C=C stretching mode of the non-oxidized graphitic domains, respectively. The peaks at 1386 and 1249 cm^{-1} are related to deformation vibration of tertiary C-OH and C-O-C stretching vibrations, respectively, while the peak at 1100 cm^{-1} is caused by vibrational mode of C-O group. The FTIR spectrum of BGO comprises bands originating from vibrations of both Bi_2O_3 and GO. In the Raman spectrum for GO, D band, G band and 2D band was found at 1351, 1595, 2671 cm^{-1} respectively. However, Bi_2O_3 is distinguished by several vibrational bands below 600 cm^{-1}. Among them, the band at 119 cm^{-1} is assigned to bismuth vibrational mode (A_g symmetry) while the bands at 138 (A_g) and 153 cm^{-1} (B_g) are attributed to displacements of both Bi and O atoms in the α-Bi_2O_3 lattice. All the other bands are due to anharmonicity of oxygen vibrational modes. The Raman spectrum of BGO reveals phonon modes attributed to both α-Bi_2O_3 and GO. For BGO composites, the D and G phonon modes are located at 1360 and 1610 cm^{-1}, respectively. The shift of the G phonon mode

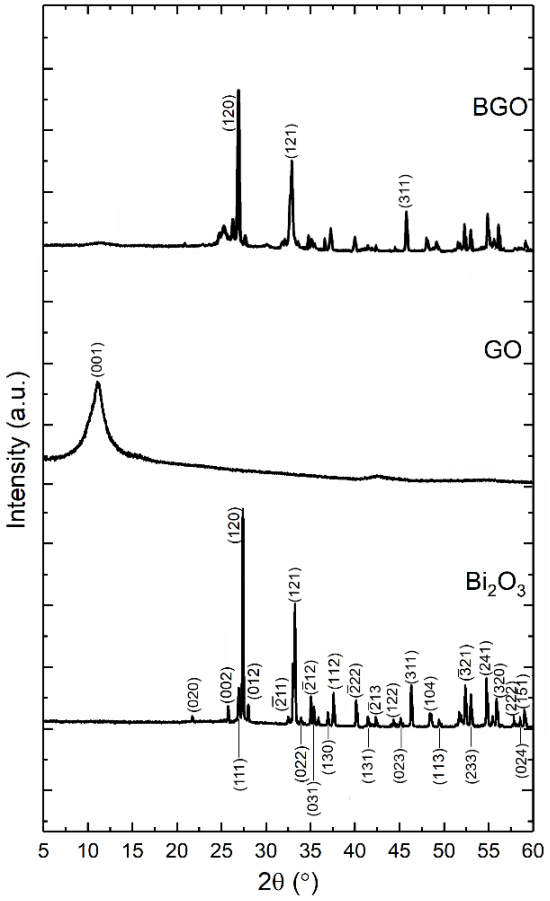

Figure 4.3.2. XRD patterns of Bi_2O_3, GO and BGO composite.

from 1595 to 1610 cm^{-1} indicates chemical bonding and hybridization between Bi_2O_3 and GO sheets. The I_D/I_G ratio, which indicates the degree of disorder/exfoliation in graphene-based materials, was found to be 1.16 for GO, but it increased to 1.22 for the BGO composites, showing that Bi_2O_3 was successfully decorated on GO (Mulik et al., 2020). All these observations confirm the decoration of Bi_2O_3 on GO in the composite BGO material.

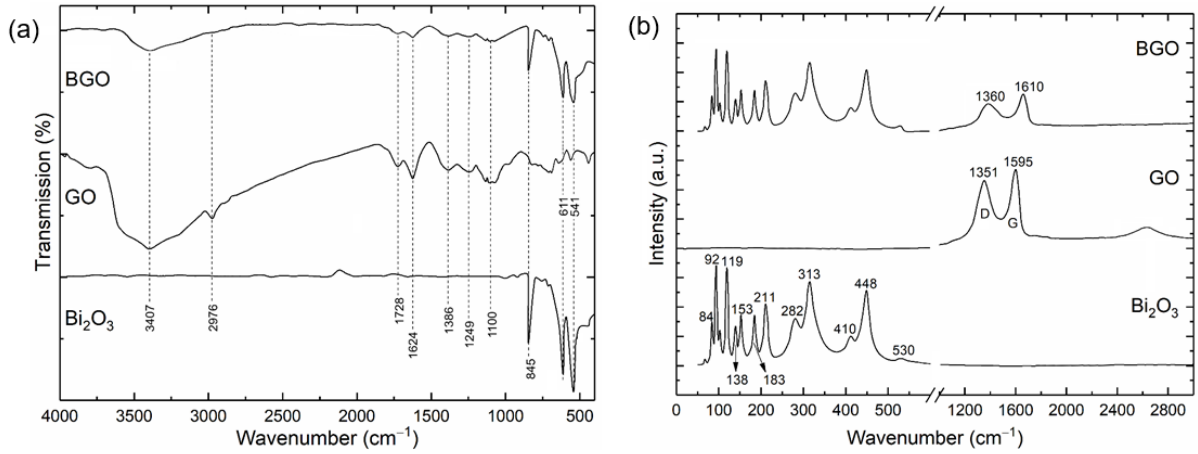

Figure 4.3.3. (a) FTIR and (b) Raman spectra of Bi_2O_3, GO and BGO composite.

High resolution SEM images were obtained using JEOL Carl Zeiss Ultra 55 field emission scanning electron microscope coupled to energy dispersive X-ray analyser to estimate elemental composition. The surface morphologies of GO, Bi_2O_3 and BGO composite were investigated using SEM analysis (Figure 4.3.4). SEM image of GO (Figure 4.3.4a) shows that it has closely packed thick lamellar structure and flaky texture mostly due to existence of carbonyl, carboxyl, hydroxyl, and epoxy groups above and below the original graphene plane (Tavakoli et al., 2015). Figure 4.3.4b illustrates the long needle-like crystal morphology of Bi_2O_3, with sharp edges and angular shapes. ImageJ analysis revealed that the average particle size of these unmodified Bi_2O_3 was 10 µm. On the other hand, SEM images of BGO composite (Figure 4.3.4c) shows the formation of uniformly distributed platelet-like structures with smooth edges suggesting the disappearance of needle-shaped particles following the decoration of GO with Bi_2O_3. These results indicate that the decoration is mostly due to the surface reaction via the coordination of the Bi(III) ion with oxygen, hydroxyl, and nitrogen-containing functional groups of GO (Han et al., 2019). The average particle size of BGO was measured to be 42.41 nm (Figure 4.3.4d). The graphic EDX spectra of GO revealed elemental compositions of 55.36 and 44.43 wt% for carbon and oxygen, respectively. Bi_2O_3 showed presence of Bi (89.7 wt%) and O (10.3 wt%). In case of BGO composites, EDX recorded 2.48, 15.97 and 81.54 wt% of C, O and Bi atoms respectively. The increase in oxygen concentration of BGO composites over Bi_2O_3 implies the successful decoration of GO with Bi_2O_3.

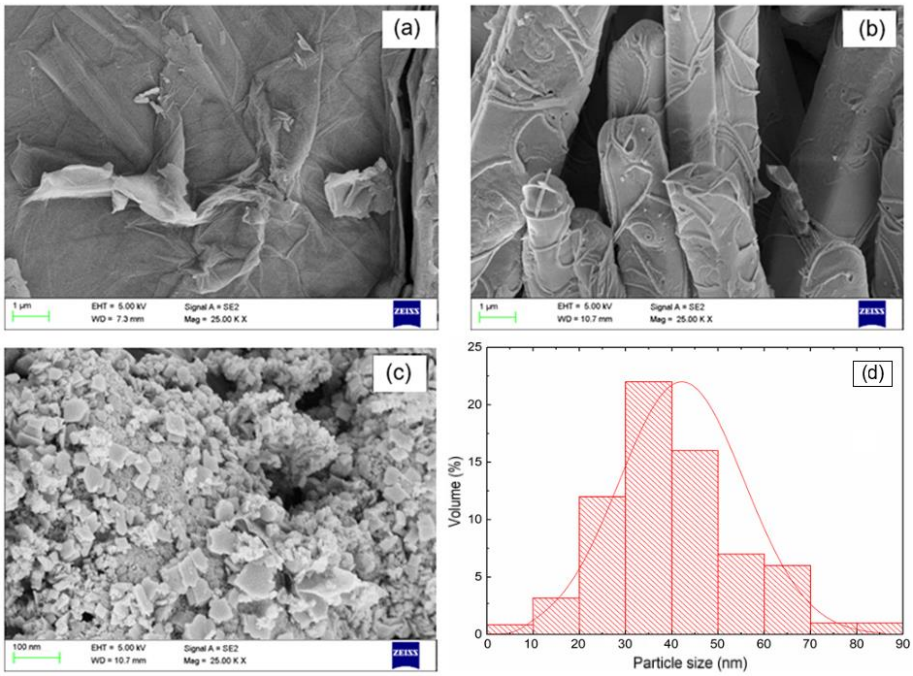

Figure 4.3.4. SEM image of (a) GO (b) Bi_2O_3 and (c) BGO composite and (d) particle size distribution of BGO fillers.

TGA curve of GO suggested weight loss in three successive steps, a weight loss (~ 15 %) around 100 – 150 °C due to vaporization of water molecules trapped between GO layers, a rapid weight loss between 150 and 230 °C due to the degradation of less stable oxygenated organic functional groups on GO sheets and a weaker mass loss in the range of 230 – 750 °C caused by combustion of the carbon skeleton. However, a weight loss of less than 2% observed in Bi_2O_3 probably due to loss of adsorbed water or oxygen, indicates its high thermal stability. For BGO, major weight loss was observed in the higher temperature range of 450 – 550 °C, owing to excellent thermal stability of Bi_2O_3. The shift in onset of thermal degradation ($T_{10\%}$) from 103 °C to 449 °C and increased residual char content of BGO compared to GO confirm the decoration of GO with Bi_2O_3.

4.3.3 Structural, thermo-mechanical and viscoelastic properties of BGO/epoxy nanocomposites

XRD patterns of neat and BGO filled epoxy nanocomposites confirmed the formation of crystalline BGO/epoxy nanocomposites. SEM images showed fairly homogenous distribution of platelike-like BGO nanofillers throughout the epoxy matrix (Figure 4.3.5). The structure of composite films appeared to be dense and compact as the loading increased from 5 – 15 wt%. The decoration of GO with Bi_2O_3 and subsequent molecular interaction between them might potentially transform GO to a carrier for Bi_2O_3 particles, thus forming continuous GO network within epoxy matrix thereby improving the uniformity in distribution of resultant BGO fillers.

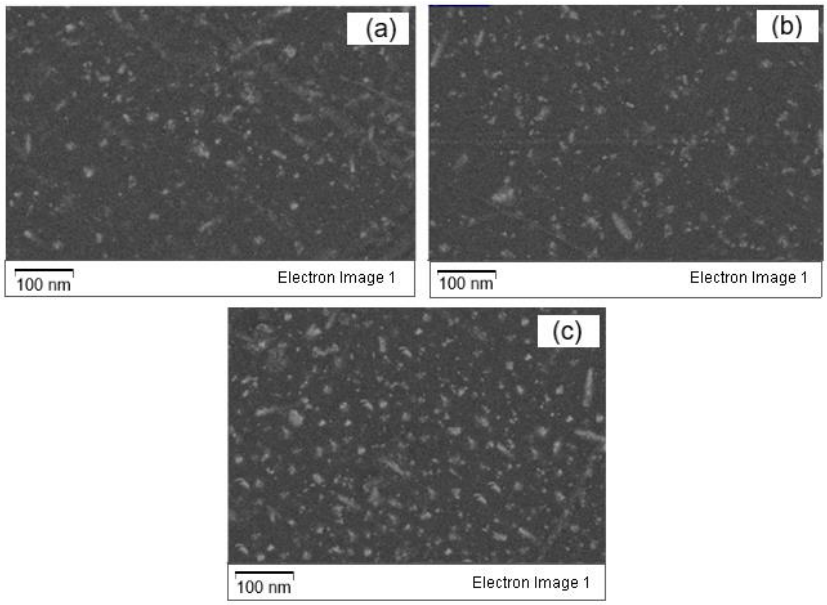

Figure 4.3.5. SEM images of (a) 5 wt%, (b) 10 wt% and (c) 15 wt% BGO filled epoxy composites.

All the epoxy nanocomposites exhibited one stage thermal degradation as seen in their TGA curves (Figure 4.3.6a). Epoxy nanocomposites display considerably greater thermal stability as indicated by shift in their major weight loss temperature (> 425 °C) towards higher side with BGO loading (Table 4.3.1). The results of this study reveal that the introduction of GO treated Bi_2O_3 fillers has considerably improved the thermal stability of resin-based systems such as epoxy. Figure 4.3.6b shows that the initial decomposition temperature of epoxy/BGO composite is higher than that of unsaturated polyester (UP), bisphenol-A based dicyanate ester and benzoxazine (DCBA/BA-a) containing PbO, short glass fibres (SGF), short basalt fibres (SBF), short Kevlar fibres (SKF) and micro/nano-Bi_2O_3 fillers at same filler loading (10 wt%) (Harish et al., 2010; Bagheri et al., 2018; Zegaoui et al., 2018; Zegaoui et al., 2020). In particular, $T_{10\%}$ for E10BGO was ~14% greater than that of DGEBA epoxy containing 10 wt% n-Bi_2O_3 (APS ~20 nm) fillers. These results suggests that increased heat capacity of the GO sheets provide better barrier effect to epoxy, slowing the thermal decomposition process.

The mechanical properties of BGO filled epoxy nanocomposites are presented in Table 4.3.2. With BGO loading, TS and YM of the composites increased significantly, most likely due to superior exfoliation and dispersion of the Bi_2O_3 decorated GO sheets and subsequent formation

Table 4.3.1. Thermal stability parameters of neat epoxy and BGO filled epoxy nanocomposites.

Sample	$T_{10\%}$ (°C)	$T_{50\%}$ (°C)	Y_c (%)	T_s (°C)	T_p (°C)	R_{max} (% °C^{-1})
E0	359.36	399.80	11.417	175.19	387.04	– 1.154
E5BGO	412.45	460.80	18.118	204.70	445.24	– 0.963
E10BGO	414.74	466.56	22.851	206.99	449.80	– 0.886
E15BGO	417.80	478.65	31.834	209.39	458.08	– 0.759

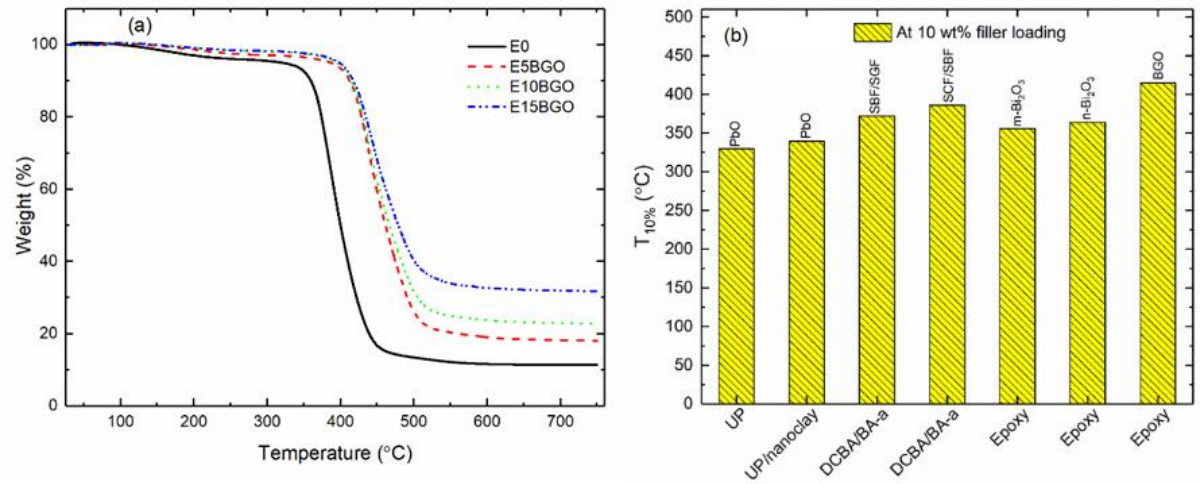

Figure 4.3.6. (a) TGA curves of BGO filled epoxy composites and (b) comparison of thermal resistance of various resin-based polymer composites.

of continuous graphene network in the epoxy matrix. However, %E of the composites showed a decreasing trend over neat resin mostly due to presence of high modulus BGO fillers, which increased the stiffness of the composites. Interestingly, %E values for epoxy/BGO composites are greater than those for previously studied resin systems. At 10 wt% loading, %E value for E10BGO is ~3.08% whereas %E value for DCBA/BA-a/SGF/SBF, epoxy/m-Bi_2O_3 and epoxy/n-Bi_2O_3 composites are 2.74%, 1.20% and 1.40%, respectively (Zegaoui et al., 2020; Muthamma et al., 2021). Higher value of %E for E10BGO might be due to formation of continuous BGO phase across epoxy matrix, which improves the mechanical interlocking and constrains the polymer segmental mobility, which would otherwise cause crack propagation.

Table 4.3.2. Tensile characteristics of neat epoxy and BGO filled epoxy nanocomposites.

Sample	TS (MPa)	YM (GPa)	%E	T (MJ m^{-3})
E0	75.15 ± 1.82	2.89 ± 0.37	4.69 ± 0.21	2.22 ± 0.18
E5BGO	98.67 ± 2.01	3.29 ± 0.62	4.32 ± 0.15	2.79 ± 0.23
E10BGO	129.34 ±1.19	3.79 ± 0.22	3.47 ± 0.17	3.08 ± 0.31
E15BGO	150.81 ± 3.2	4.36 ± 0.42	3.05 ± 0.20	3.14 ± 0.14

The dynamic mechanical behaviour of BGO filled epoxy nanocomposites has been investigated to understand the changes in E′, E″, T_g, and tan δ with BGO filler loading. As the temperature increased, the value of E′ reduced for all the epoxy composites, which is most likely due to the restriction in molecular mobility of the polymer chains. The synergistic effect of integrating micro and nano sized fillers was exploited such that the gaps between GO sheets were filled by linking Bi_2O_3 fillers resulting in formation of a network within the epoxy matrix, thus enhancing the stiffness of the composites. The influence of the BGO fillers on the thermo-mechanical properties of epoxy composites was assessed using C-factor, degree of entanglement density (N), glass transition temperature (T_g) and tan δ as presented in Table 4.3.3. The viscoelastic properties of 15 wt% BGO loaded epoxy composites were superior to all other samples. Also, the Cole-Cole plot showed semi-circular patterns for all samples, irrespective of filler loading, indicating good adhesion and positive reinforcing effect of fillers.

4.3.4 X-/γ-ray attenuation properties of BGO/epoxy nanocomposites

X-ray attenuation experiment was performed on well a calibrated X-123 CdTe X-ray detector spectrometer for X-rays of energy 32.06 and 36.35 keV emitted by ^{137}Cs source and 30.85 and 35.10 keV from ^{133}Ba. γ-ray attenuation experiment was performed using four radioactive sources, namely, ^{133}Ba (53.16, 80.99, 276.40, 302.85, 356 and 383.85 keV), ^{22}Na (511 and 1274.5 keV), ^{137}Cs (662 keV) and ^{60}Co (1173 and 1332 keV). We have carried out the attenuation experiment following the procedure as described in the Section 2.1.3.

Table 4.3.3. Thermo-mechanical properties of neat epoxy and BGO filled epoxy nanocomposites.

Sample	E' (MPa)		C-factor	N (At 150 °C) (mol m^{-3})	T_g (°C)	tanδ at T_g
	Glassy region (E'_g)	Rubbery region (E'_r)				
E0	3421.902	35.848	--	1698.882	131.338	0.700
E5BGO	3806.310	38.628	1.032	1830.630	133.235	0.634
E10BGO	4190.719	43.001	1.021	2037.872	135.132	0.600
E15BGO	4575.127	47.312	1.013	2242.176	136.555	0.591

--: *Not present*

Theoretical μ/ρ values of BGO/epoxy nanocomposites computed using PAGEX showed good agreement, validating the usefulness of newly developed PAGEX software. At a given loading, the μ/ρ values of the epoxy nanocomposites increased with increasing BGO loading and decreased with incident photon energy (Figure 4.3.7). However, the variation of μ/ρ values with photon energy is prominent in two regions i.e., 30.85 – 80.99 keV and 276.40 – 1332.50 keV. The μ/ρ values increase significantly with BGO loading and decrease sharply as the photon energy increases in the energy range 30.85 to 80.99 keV. This is caused by variation in dominance of photoelectric absorption, Compton scattering and pair production in different energy regions. Below 80.99 keV, photoelectric absorption cross-section is not only adequately high but also depend on Z^4 and $E^{-3.5}$ and therefore photons are attenuated mostly by photoelectric absorption. As a result, increasing the BGO loading in epoxy matrix increases the μ/ρ values, and because of photoelectric cross-section being inversely proportional to energy, μ/ρ decreases rapidly with increase in photon energy. E15BGO samples having the highest Bi content showed highest μ/ρ values when compared to others.

When the photon energy exceeds 80.99 keV, the probability of photoelectric absorption decreases and Compton scattering takes over. Since the Compton scattering cross-section varies as Z and E^{-1}, the μ/ρ value for each kind of sample slightly decreases with increasing photon energy while remaining almost constant with increased BGO loading. The probability of Compton scattering is related to the number of electrons per unit mass, which is proportional to the atomic number to atomic weight ratio (Z/M). In other words, the values of μ/ρ for all elements in this Compton scattering dominated region tend to be approximately the same. As a result, the increase in BGO loading does not lead to a drastic variation in μ/ρ values in the energy range of 276.40 to 1332.5 keV (Inset of Figure 4.3.7). However, at any given loading and energy, the experimental μ/ρ values of the epoxy/BGO nanocomposites are much greater than their micro counterparts.

The molecular attachment of Bi_2O_3 to the surface of GO via surface decoration not only reduces the size of decorated BGO fillers but also alters their dispersion in the epoxy matrix. The formation of a continuous BGO-based epoxy network enables dense composite structures with few/no void routes for unattenuated photon penetration. Further, because the modified BGO fillers are nanometric in size, they have a higher surface-to-volume ratio, which means that for a given volume fraction of nanocomposites, the number of surface atoms is much higher and inter-particle distances are much shorter than for corresponding microcomposites. The probability of photons participating in multiple scattering processes increases as surface area availability increases. As a result, photons will undergo several scattering processes until their energy fall below 100 keV, at which point they will be readily attenuated by photoelectric absorption. In addition to the size effect, the presence of more low-Z atoms (such as H, C, and O) in BGO than in Bi_2O_3 enhances the possibility of radiation attenuation via Compton scattering. Furthermore, such surface decoration can result in an increase in molecular weight, which improves photoelectric absorption in composites. These findings suggest that the synergistic effect of integrating micro- and nano-sized fillers can be used to improve the radiation attenuation properties of PMCs.

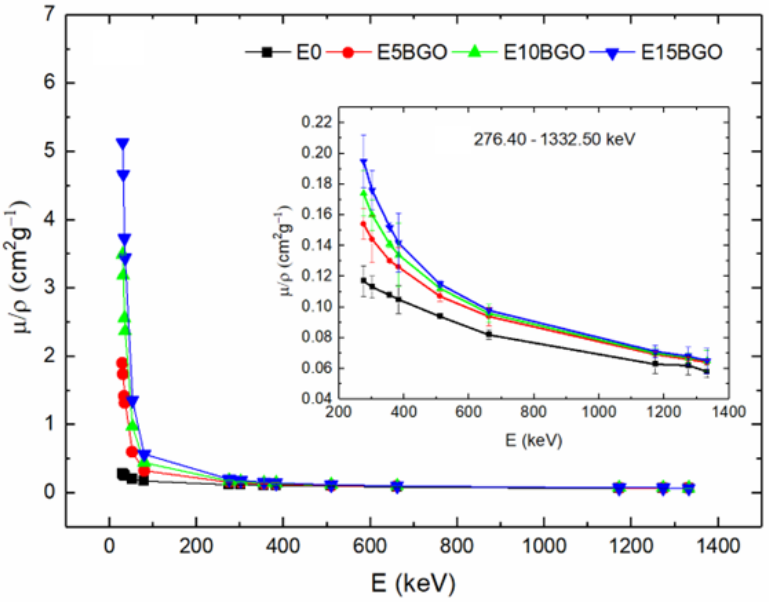

Figure 4.3.7. Variation of μ/ρ of epoxy nanocomposites with BGO loading.

The μ/ρ values of E15BGO was compared with traditionally used shielding materials and Bi-based PMCs in the energy range 30.85 to 1332.50 keV to further substantiate the correlation between surface decoration, filler size effect, and radiation attenuation (Table 4.3.4). E15BGO composites exhibit much better attenuation than 50 wt% nano-Bi_2O_3 loaded PMCs (Abdalsalam et al., 2020; Mehrara et al., 2021). Bi_2O_3 nanoparticles dispersed in silicone resin

and PC matrices were bigger in size (100 and 150 nm, respectively) than BGO (50 nm) employed in this investigation. Two factors might impact shielding efficiency: (a) filler size differences and (b) nano-filler aggregation at increased loading. E15BGO nanocomposites demonstrated shielding comparable to 14 wt% nano-Bi_2O_3 (20 nm) loaded epoxy composites (Muthamma et al. 2021). The formation of a continuous inter-linked epoxy/BGO network ensures uniform distribution of fillers throughout the matrix, which in turn improves radiation attenuation. These findings suggest that low loadings of surface modified micro-nano hybrid fillers can attenuate radiations as high as nanofillers alone, paving the way for novel hybrid materials. We also computed the percent heaviness of E15BGO composites and compared it to other materials. In comparison to lead, E15BGO has 2.15% heaviness.

Table 4.3.4. Comparison of μ/ρ values.

PMCs	μ/ρ (cm^2 g^{-1}) at various energies (MeV)							
	0.059	0.080	0.356	0.511	0.662	1.274	1.173	1.332
Lead (Belgin and Aycik, 2015)	--	--	--	--	0.100	--	--	0.056
Ordinary concrete (Sharifi et al., 2013)	--	--	--	0.088	0.079	--	--	0.056
Barite (Sharifi et al., 2013)	--	--	--	0.092	0.078	--	--	0.052
Stainless steel 304L (Büyükyıldız et al., 2017)	--	--	0.100	--	0.074	--	--	0.054
10 wt% Bi_2O_3/Unsaturated polyester (Ambika et al., 2017)	--	0.357	0.128	--	0.085	--	0.057	0.052
500 phr Bi_2O_3/Natural rubber (Toyen et al., 2017)	--	--	--	--	0.070	--	0.036*	
50 wt% Bi_2O_3/Silicone resin (Verdipoor et al., 2018)	--	--	0.099	--	0.075	--	0.055	0.052
50 wt% n-Bi_2O_3/Silicone resin (Verdipoor et al., 2018)	--	--	0.110	--	0.084	--	0.065	0.061
50 wt% Bi_2O_3/PVA (Muthamma et al., 2019)	1.570	--	--	--	0.092	--	--	--
2 wt% n-Bi_2O_3/HDPE (Abdalsalaam et al., 2020)	--	0.212	--	0.117	--	--	--	--
44 wt% Bi_2O_3/PMMA (Cao et al., 2020)	--	--	0.107	--	0.064	--	0.083	0.089
35 wt% Bi_2O_3/Epoxy (Muthamma et al., 2020)	0.876	--	--	--	0.084	--	--	--
14 wt% n-Bi_2O_3/Epoxy (Muthamma et al., 2021)	--	--	0.150	0.112	0.094	0.063	0.069	0.060
50 wt% n-Bi_2O_3/Polycarbonate (Mehrara et al., 2021)	2.930	--	0.130	--	--	--	--	--
E15BGO (Present work)	--	0.564	0.152	0.115	0.098	0.068	0.071	0.065

--: *Not present; *: Value at 1.245 MeV.*

4.3.5 Conclusions

In the present study, Bi_2O_3 decorated GO fillers were employed as a key to tailor the performance of DGEBA epoxy nanocomposites. XRD, Raman spectroscopy and SEM-EDX analysis of BGO composites confirmed the successful surface decoration. BGO/epoxy nanocomposites displayed good thermal resistance (~ 450 °C) and glass transition temperature (~ 136 °C), elastic modulus (~ 4.36 GPa) and high storage modulus, thereby confirming the improved dispersion and better interfacial adhesion in the composites. The formation of continuous filler network across epoxy matrix via synergistic shielding effect of combining high-Z metal oxide fillers with GO significantly improved the X-ray and γ-ray shielding properties of these composites in the wide energy range of medical interest (30 – 1332 keV). More importantly, small loadings (≤ 15 wt%) of hybrid filler BGO could realize significant enhancement in thermo-mechanical and radiation shielding properties of epoxy/BGO nanocomposites. Thus, this study serves to open a new avenue for novel and lead-free radioprotective materials.

This work on BGO/Epoxy composites is under revision in the *Advanced Composite Materials,* 2022.

4.4 PAGEX: A simple and robust software for computation of photon and charged particle interaction parameters

PAGEX is a compact and user-friendly cross-platform software package that we designed for the rapid computation of photon (X-ray and γ-ray) and charged particle interaction parameters. It is based on well-established theoretical formulations and computational techniques that integrates various Python packages to effectively calculate various parameters over a wide energy range. We have verified the results from PAGEX, against other commonly used software and databases, with satisfactory results. PAGEX, being a one-stop solution to radiation researchers, is made available freely to the public. In the following sections, we provide further information about PAGEX, including the rationale for developing it, the methodology used and its application.

4.4.1 Rationale behind the work

As we already know, evaluation of radiation interaction parameters is crucial for the assessment of the radiological properties of the any interacting medium. The basic quantities useful in understanding penetration depth and energy deposition of photon radiations in any medium are mainly mass attenuation coefficient (μ/ρ; $cm^2\ g^{-1}$), mass energy absorption coefficient (μ_{en}/ρ;

$cm^2\ g^{-1}$), total interaction cross-section per atom (σ; b $atom^{-1}$), effective cross-section per atom (σ_a; b $atom^{-1}$) and effective cross-section per electron (σ_e; b $electron^{-1}$), effective atomic number (Z_{eff}) and electron density (N_{eff}; electrons g^{-1}), energy absorption effective atomic number (Z_{PEAeff}) and electron density (N_{PEAeff}; electrons g^{-1}), kinetic energy released per unit mass (KERMA), equivalent atomic number (Z_{eq}), energy absorption (EABF) and exposure (EBF) build-up factors. For charged particle radiations, mass stopping power (S(E)/ρ; MeV $cm^2\ g^{-1}$) and mass stopping cross-sections (S_c; MeV cm^2 $atom^{-1}$) are the parameters of fundamental importance. Manual determination of the above-mentioned parameters may not lead to reliable results because of the tedious calculations and the involvement of several intermediate parameters. Consequently, several software/programs have been developed so far for swift computation of these parameters whose functionality is summarized in Table 4.4.1. Despite having different platforms to compute various radiation interaction parameters in diverse energy ranges using different methods, to the best of our knowledge, a cross-platform software that can calculate most of the radiation interaction parameters on a single platform is not yet available. In view of this, we developed a user-friendly graphical user interface (GUI) software named PAGEX (interaction of Proton, Alpha, Gamma rays, Electrons, and X-rays with matter) that is more comprehensive than existing packages and simplifies the task of calculating various radiation interaction parameters by providing a single package to calculate what used to take many different packages. Having captured the essence of the previous efforts, our software outperforms others as to account for highest number of parameters computed over wide energy and atomic number coverage using well established methodology (Table 4.4.1).

4.4.2 PAGEX – The software

PAGEX software is a GUI written in Python 3.7.2 and HTML5 languages using Visual Studio code editor version: 1.35.1. The code has been successfully tested for its operation and compatibility on multiple-operating systems (mainly Microsoft Windows, macOS and Linux). We have released PAGEX under open-source MIT License and the source-code is hosted on GitHub (https://github.com/sriharijayaram5/PAGEX), enabling active usage and improvement. Despite of being user-friendly, we have provided online PAGEX manual (pagex.readthedocs.io) containing detailed description of usage of software and framework of the Python code used. We have used well-established theoretical formulations and analytical techniques to compute the parameters included in PAGEX. The flowchart of working of PAGEX is shown in Figure 4.4.1. The software has been designed to achieve good level of

accuracy through quick and cogent computations. Average time to compute all the parameters for a typical compound on a macOS Catalina with 2.6 GHz 6-core Intel Core i7 processor and 16GB installed RAM is about 10 s. The images of PAGEX user interface/splash screen, its execution mode and output are presented in Figures 4.4.2(a-c).

4.4.3 PAGEX validation

Computations of several photon and charged particle interaction parameters in PAGEX have been verified by comparison with the values from currently available computer programs and standard databases, particularly μ/ρ and $S(E)/\rho$, from which all the other parameters are derived. Validation has been performed on wide variety of materials with elements ranging from low Z to high Z in wide energy region. μ/ρ values computed using PAGEX for various elements and compounds/mixtures in the energy range of 1 keV - 100 GeV have been compared with WinXCom software values, and the maximum % deviations are shown in Table 4.4.2. It has been observed that low Z materials exhibit considerable larger deviation compared than high Z materials, mostly due to presence of absorption edges. In any case, the disagreement in the μ/ρ values is ≤ 3 % when compared to WinXCom value.

Auto-Z_{eff} software has been considered as a standard software to validate Z_{eff} values using both direct and interpolation method (Figure 4.4.3). In the energy range of 10 keV - 1 GeV, we found that Z_{eff} values obtained from PAGEX (by interpolation method) are in close proximity Auto-Z_{eff} values. Such good level of agreement in the values is most likely due to the similarity in the methodology adopted in both the software. The PAGEX Z_{eff} values computed from direct method matches well with the values from interpolation method and Auto-Z_{eff} only in the energy range of 50 keV - 10 MeV, where Compton scattering is dominant.

ANSI is the only database currently available for providing a comprehensive set of standard data on build-up factors for about 23 elements, with data for the other elements interpolated as previously stated. For validation, we computed EABF and EBF build-up factors for water, concrete, and air at different penetration depths in the energy range 0.015 - 15 MeV (compositions for air and concrete taken from ANSI). Figure 4.4.4 depicts the photon energy dependency of EABF and EBF values from PAGEX and ANSI at various penetration depths. Build up factor values computed using PAGEX demonstrated good agreement with those from ANSI.

Table 4.4.1. Various software and parameters computed.

Software	Parameters	Energy range	Z-range	Database used
XMuDat (Nowotny, 1988)	μ/ρ, μ_{tr}/ρ, μ_{en}/ρ and single valued Z_{eff}	1 keV - 50 MeV	$Z \leq 92$	Hubbell and Seltzer (1995); Boone and Chavez (1996)
WinXCom (Gerward et al., 2004)	Partial/total μ/ρ and σ	1 keV - 100 GeV	$Z \leq 100$	Hubbell and Seltzer (1995)
Auto-Z_{eff} (Taylor et al., 2012)	Z_{eff}	10 keV - 1 GeV	$Z \leq 100$	Pratt (1960); Scofield (1973); Hubbell et al. (1975); Hubbell and Overbo (1979); Hubbell et al. (1980); Hubbell and Seltzer (1995)
Direct-Z_{eff} (Un and Caner, 2014)	μ/ρ, Z_{eff} and N_{eff}	1 keV - 100 GeV	$Z \leq 100$	Gerward et al. (2004)
EXABCal (Olarinoye et al., 2019)	Z_{eq}, EABF and EBF	15 keV - 15 MeV	$Z \leq 92$	ANSI/ANS-6.4.3 (1991)
BXCOM (Eyecioglu et al., 2019)	Z_{eff}, N_{eff}, Z_{eq}, EABF and EBF	15 keV - 15 MeV	$Z \leq 92$	ANSI/ANS-6.4.3 (1991); Gerward et al. (2004)
Phy-X/PSD (Sakar et al., 2019)	μ/ρ, σ_a, σ_e, Z_{eff} and N_{eff}	1 keV - 100 GeV	$Z \leq 100$	Berger and Hubbell (1987); ANSI/ANS-6.4.3 (1991); Chilton et al. (1984); Kaplan (1989)
	Z_{eq}, EABF and EBF	15 keV - 15 MeV		
	Fast neutron removal cross-section			
Phy-X/ZeXTRa (Özpolat et al., 2020)	Z_{eff} and Z_{PEAeff} for photons	1 keV - 20 MeV	$Z \leq 100$	Gerward et al. (2001; 2004); Hubbell and Seltzer (1995); Berger et al. (2005); Ziegler et al. (2010)
	Z_{eff} for charged particles and carbon ion	1 MeV - 1 GeV		
PAGEX	μ/ρ, σ_a and σ_e Z_{eff} and N_{eff} for photons	1 keV - 100 GeV	$Z \leq 100$	White et al. (1989); ANSI/ANS-6.4.3 (1991); Hubbell and Seltzer (2004); Berger et al. (2005); Berger et al. (2010)
	Z_{eff} and N_{eff} for charged particles	1 keV - 10 GeV	$Z \leq 100$	

μ_{en}/ρ, Z_{PEAeff}, N_{PEAeff} and K_R	1 keV - 20 MeV	$Z \leq 92$
Z_{eq}, EABF and EBF	15 keV - 15 MeV	$Z \leq 92$
$S(E)/\rho$, S_c, Z_{eff} and N_{eff} for electrons	10 keV - 1 GeV	$Z \leq 98$
$S(E)/\rho$, S_c, Z_{eff} and N_{eff} for protons	1 keV - 10 GeV	$Z \leq 92$
$S(E)/\rho$, S_c, Z_{eff} and N_{eff} for alpha particles	1 keV - 1 GeV	$Z \leq 92$

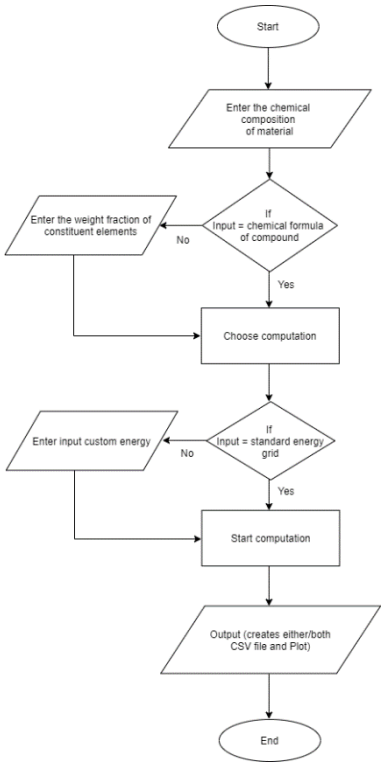

Figure 4.4.1. Flowchart of PAGEX software.

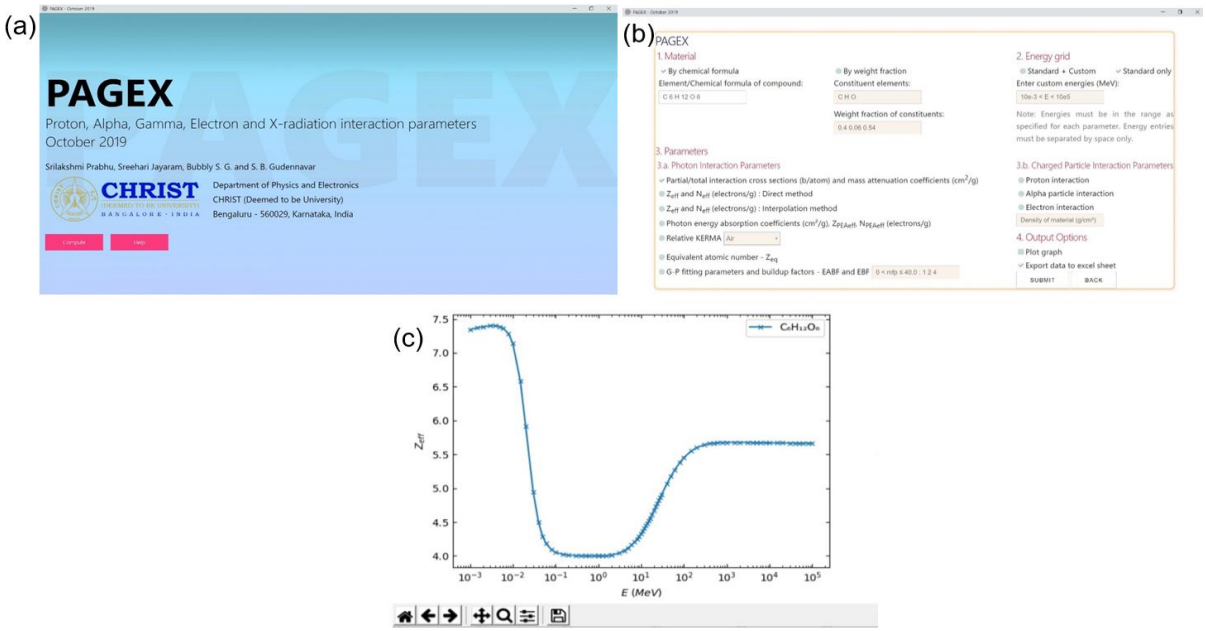

Figure 4.4.2. (a) PAGEX GUI, (b) main page of PAGEX showing the material input, parameters grid and output options and (c) graphical output from PAGEX.

Table 4.4.2. Percentage of deviation of PAGEX μ/ρ values from WinXCom.

to

Element/compound	1 keV - 0.1 MeV	0.1 - 100 MeV	100 MeV - 100 GeV
Acetone	0.179	2.843	2.913
Glycine	0.229	2.506	2.414
Skin	0.247	2.736	2.511
Rheum leaves	0.233	2.850	2.857
Sulphur	0.049	1.652	1.538
Silicon carbide	0.055	2.326	1.733
Cu-Zn alloy	0.042	1.289	0.826
Cadmium telluride	0.010	1.115	0.567
Barium sulphate	0.041	1.507	0.849
Europium	0.017	1.170	0.520
Gadolinium oxide	0.032	1.228	0.535
PbO-SiO_2 glass	0.038	1.062	0.611
Lead metal	0.033	0.803	0.418

The computed S(E)/ρ values for charged particles were compared to the standard NIST databases - ASTAR, PSTAR, and ESTAR. The S(E)/ρ values computed for protons, electrons and alpha particles by PAGEX for diverse materials with a wide range of Z showed good agreement with above-mentioned standard databases. More importantly, PAGEX is the first software to compute Z_{eff} values for electrons, protons, and alpha particles with energies ranging from 1 keV to 10 GeV. Above all, it is worth noting that the current study represents an extension to the PSTAR and ASTAR databases. ASTAR and PSTAR both give S(E)/ρ data for just 26 elements and 48 compounds/mixtures, but PAGEX provides data for all elements from

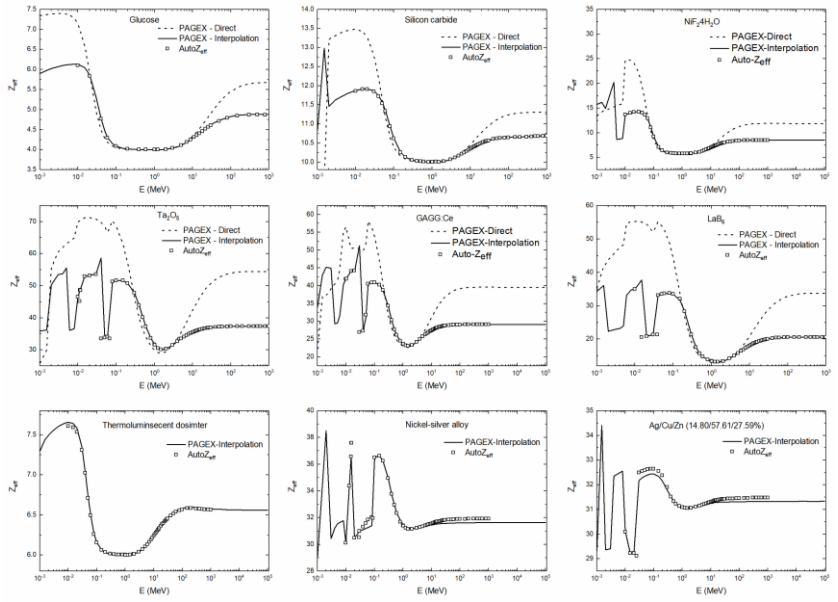

Figure 4.4.3. Comparison of Z_{eff} values from PAGEX and Auto-Z_{eff}.

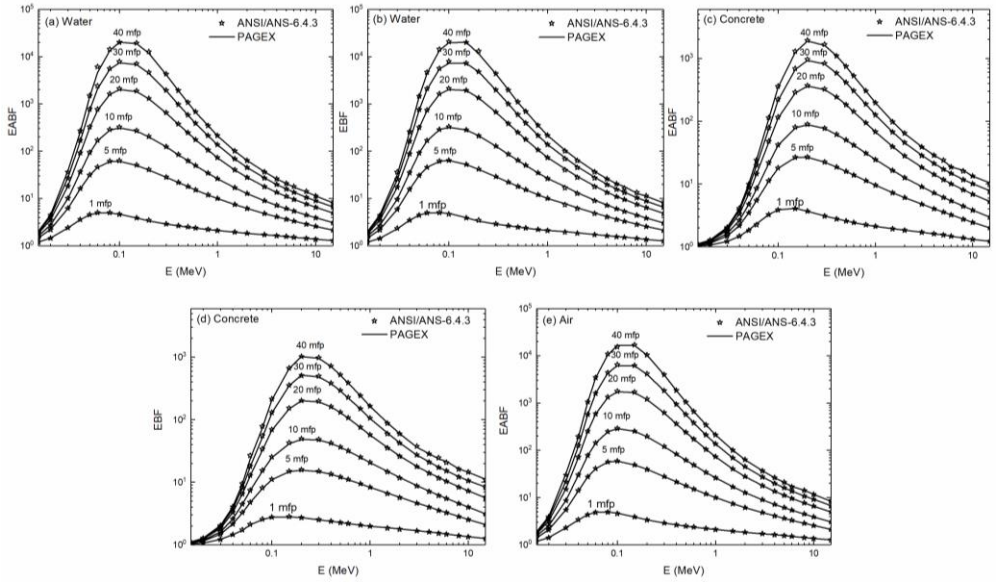

Figure 4.4.4. Comparison of EABF and EBF values for water, concrete and air from PAGEX and ANSI database.

Z = 1 to 92. PAGEX can reliably compute the S(E)/ρ values for any user-specified compound/mixture in the chosen energy region. Figure 4.4.5 depicts the Z_{eff} for charged particle interactions in various substances.

4.4.4 Conclusions

In this work, we attempted to design and develop PAGEX, a robust software that easily facilitates the computation of photon and charged particle interaction parameters relevant in radiation dosimetry and shielding. This user-friendly software can do precise and fast computations. PAGEX is dependable because it employs well-established theoretical

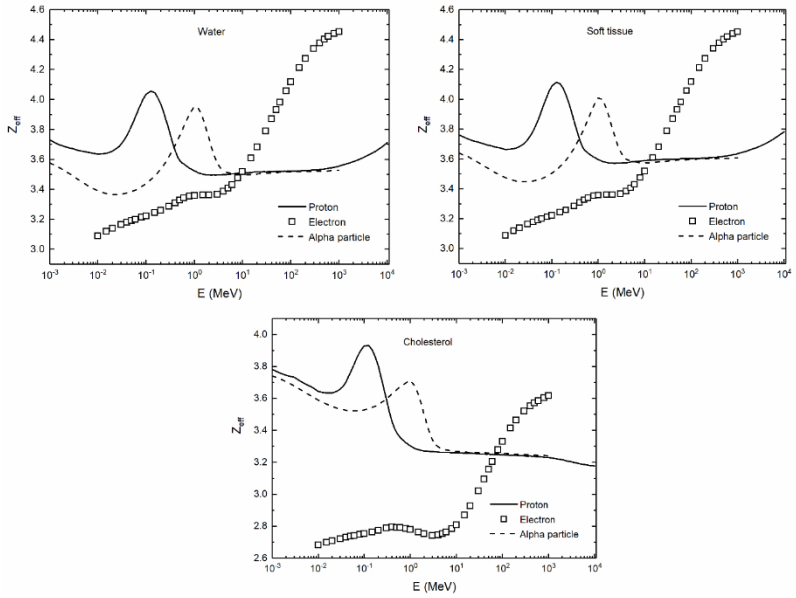

Figure 4.4.5. Variation of Z_{eff} as function of kinetic energy for proton, electron and alpha particle interaction.

formulations and analytical methodologies. PAGEX interaction parameters were evaluated against other published theoretical calculations, standard databases, and software for some representative materials. PAGEX's ability to compute both photon and charged particle interaction parameters for both the whole energy range and user defined energies on a single platform is a crucial element. Furthermore, the software generates both tabular and graphical output. This comprehensive software, which can operate on different platforms, offers radiation researchers with a single full package for rapid computation of photon and charged particle interaction parameters.

This work on PAGEX is published in the *Applied Radiation and Isotopes,* **176**, 109903 (1-12), 2021.

5. SUMMARY AND FUTURE WORK

5.1 Summary of the work

Light-weight and lead-free sodium alginate and epoxy-based polymer composites have been synthesized for their use in photon shielding applications. The structural, thermo-mechanical and viscoelastic properties of all the polymeric systems were investigated to assess their thermal stability, mechanical strength and reinforcing efficiency of incorporated fillers. Solution cast films of calcium ion cross-linked SA/Bi_2O_3 composites were found to be soft and flexible unlike high-modulus polymers like high density polyethylene (HDPE), poly (vinyl chloride) (PVC) and so on. Calcium ion cross-linking not only made the SA films robust and hydrophobic but significantly improved their thermal stability and tensile strength. 40 wt% Bi_2O_3 loaded SA films showed heat resistance as high as 251 °C, tensile strength of ~172 MPa and 4% elongation at break. All the SA-based composites good resistance to different chemicals including acids, organic solvents and oil, thereby extending their real-life applications. Above all, these composites show high level of biodegradability posing no potential environmental issues. Also, SA/Bi_2O_3 composite films were found to be effective in shielding γ-rays of 0.356 - 1.332 MeV energies, which falls in energy range of medical and industrial interest. 40 wt% Bi_2O_3 loaded SA composite films with highest shielding efficiency among this set can be used for developing soft and sewable radioprotective materials in the form of radioprotective gloves and apparels, pouches to store radiopharmaceuticals and radioactive isotopes.

Epoxy-based polymer composites, on the other hand, display inherently high thermal stability, high specific strength, excellent electrical insulation, chemical, heat, solvent, and moisture

resistance. All these material properties were found to be enhanced with addition of high modulus fillers like Bi_2O_3 and Ta_2O_5. With 30 wt% micro Ta_2O_5 loading, epoxy composites achieved thermal strength of 430 °C, tensile strength of ~535 MPa, 2.64% elongation at break and T_g of 138 °C. More interestingly, these properties enhanced significantly on addition of nano-Ta_2O_5 at same loading, with effect being predominant at lower loading as seen in the Figure 5.1.1. For instance, at 10 wt% Ta_2O_5 loading, epoxy nanocomposites showed 24.98% enhancement in tensile strength over microcomposites while the %enhancement was found to be around 7.48% at 30 wt% loading. γ-ray shielding studies also revealed the upper hand of epoxy nanocomposites at any given energy and loading. At a given energy, 20 wt% n-Ta_2O_5/epoxy composites showed significantly greater shielding performance compared to 30 wt% micro-Ta_2O_5/epoxy composites. And the γ-ray attenuation efficiency was observed to be highest for 30 wt% nano-Ta_2O_5 loaded epoxy composites among the studied samples. These observations demonstrated that low level of nanofiller loading is sufficient enough to display enhanced material properties. This was further proved in another study where we employed low loadings (5, 10 and 15 wt%) Bi_2O_3 decorated graphene oxide (GO) nanofillers, abbreviated as BGO, to tailor the performance of epoxy polymer matrix. The surface decoration, filler size and loading, dispersion and interfacial adhesion between matrix-filler phase was systematically correlated with thermo-mechanical and shielding properties of resultant epoxy nanocomposites. At 15 wt% BGO nano-filler loading, epoxy nanocomposites showed good thermal resistance (~ 450 °C) and glass transition temperature (~ 136 °C), elastic modulus (~ 4.36 GPa) and high storage modulus, thereby confirming the improved dispersion and better interfacial adhesion in the composites. Interestingly, BGO/epoxy nanocomposites displayed thermal stability superior to other polymer-based materials with higher filler loading. Also, the BGO addition improved the ability of epoxy matrix to resist deformation before fracture on application of tension. For instance, at 10 wt% filler loading, BGO/epoxy showed %E value of 3.47%, which is relatively higher than that of SGF/SBF DCBA/BA-a, m-Bi_2O_3/epoxy and n-Bi_2O_3/epoxy composites as represented in the Figure 5.1.2 (Zegaoui et al., 2020; Muthamma et al., 2021). An appreciable enhancement in radiation attenuation characteristics was observed in X-ray and γ-ray energy region (30 – 1332 keV), mainly due to the synergistic shielding effect of combining high-Z metal oxide fillers and GO. At any given loading and energy, 15 wt% BGO/epoxy nanocomposites displayed highest shielding performance compared to 40 wt% Bi_2O_3/SA and 30 wt% micro-/nano-Ta_2O_5/epoxy composites as explored in the present work. Therefore, this study serves to open a new avenue for novel and lead-free radioprotective

materials. Epoxy-based materials, in general, are non-carcinogenic, cost effective and versatile, thereby making them appealing candidates for use in storing nuclear wastes in corroding environments, safety enclosures to critical areas of reactor amenities, storage facilities of nuclear fuels in laboratory, hospitals and industry.

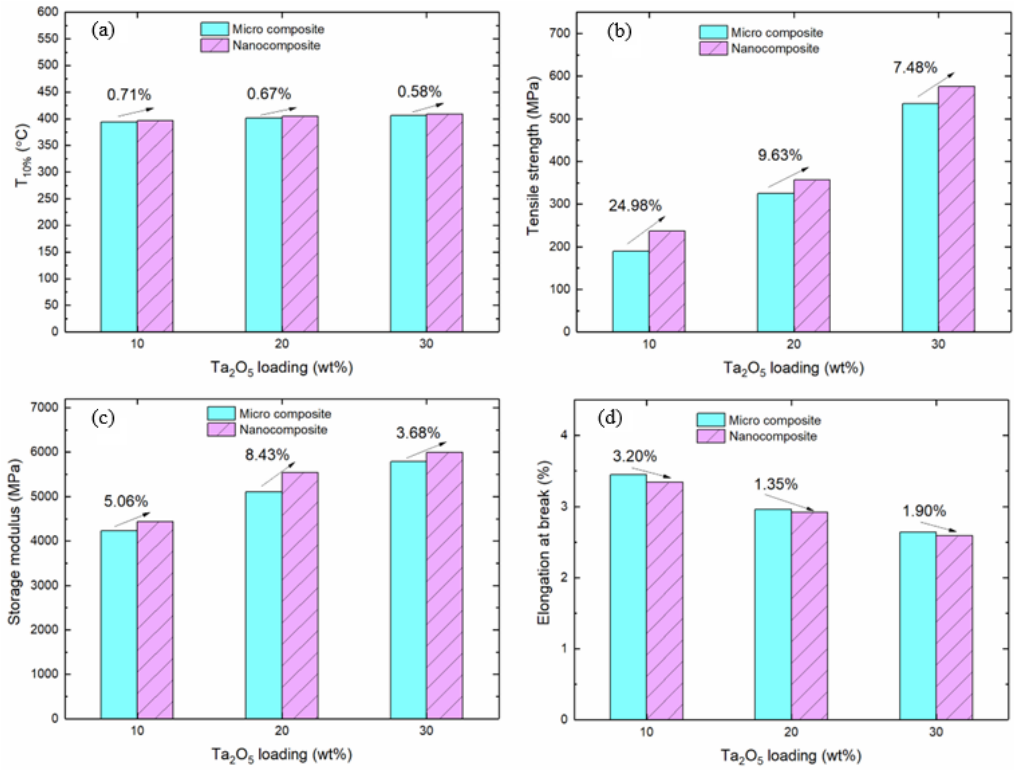

Figure 5.1.1. Comparison of (a) $T_{10\%}$, (b) tensile strength, (c) storage modulus and (d) % elongation at break between micro- and nano-Ta_2O_5/epoxy composites at various filler loadings.

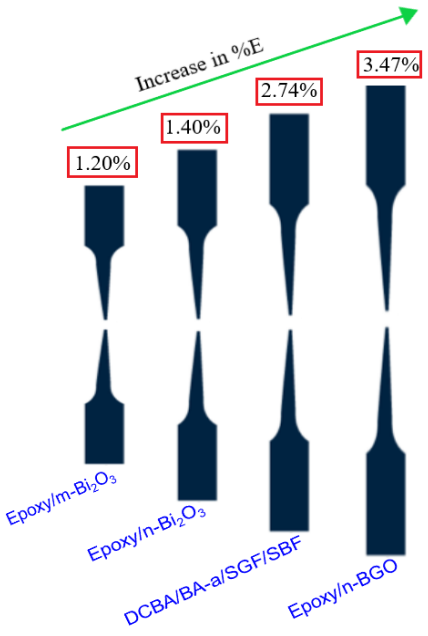

Figure 5.1.2. Comparison of %E of various polymer composites at 10 wt% filler loading.

Table 5.1.1 provides summary of the physical, thermal, mechanical and shielding parameters (at 0.662 MeV) for the most effective polymer - filler combination studied in the present work. Among the studied composites, 15 wt% BGO/epoxy nanocomposites showed highest thermal stability with peak degradation temperature of ~458 °C. This could be attributed either to the lowest filler size (~42 nm) of BGO nanocomposites facilitating creation of more efficient physical shield against thermal degradation or due to high heat capacity (710 J kg^{-1} K^{-1}) of GO sheets. On the other hand, 30 wt% nano-Ta_2O_5/epoxy nanocomposites displayed superior tensile strength (~576 MPa), Youngs modulus (11.38 GPa) and storage modulus (~6000 MPa) among the studied composites. This is mostly due to the incorporation of high rigidity modulus (~190 GPa) Ta-based fillers in epoxy matrix along with increased surface-to-volume ratio of nanofillers and stronger matrix-filler interfacial adhesion further improving the stiffness of the composites. Yet again, among the studied composites, 15 wt% BGO/epoxy nanocomposites showed highest μ/ρ values, at any given energy, despite of high loading ($\geq$ 30 wt%) of Bi_2O_3 and Ta_2O_5 fillers in SA and epoxy matrices. The decoration of 3D Bi_2O_3 fillers on 2D GO enables the formation of compact microstructure which on further incorporation into polymer matrix results in the formation of a continuous network across reinforced phase unlike polymer composites containing undecorated fillers. In the latter, the probability of voids or interstitial spaces in the matrix is higher than in the former, resulting in higher transmission of unattenuated photons. Therefore, it can be concluded that the surface decoration of inorganic metal/metal oxide-based fillers with organic carbon-based nanomaterials and their integration into polymer matrix is the key to tailor the properties of the end-product. Overall, BGO/epoxy nanocomposites were found to be the best among studied samples in terms of overall thermo-mechanical and photon shielding properties.

The development of a user-friendly and robust Python-based software, PAGEX, has made the computation of photon and charged particle (proton, electron and alpha particle) interaction parameters easier and time efficient. The use of well-established theoretical formulations and analytical techniques makes the results from PAGEX reliable as validated against some of the standard database/software. PAGEX is not merely a software that serves as one-stop solution with integration of varieties of radiation interaction parameters but also accounts for data missing in certain standard databases using scientifically accurate techniques. With cross-platform functionality and one-click usage, PAGEX can be used for computation of any desired photon and charged particle interaction parameters.

Table 5.1.1. Synergistic properties of synthesized composites.

Polymer composite	40 wt% Bi_2O_3/SA	30 wt% m-Ta_2O_5/Epoxy	20 wt% n-Ta_2O_5/Epoxy	Epoxy/n-Ta_2O_5	Epoxy/n-BGO
Filler loading (wt%)	40	30	20	30	15
Average filler size	15 µm	4 µm	75 nm	75 nm	42 nm
Initial decomposition temperature (°C)	236.66	406.37	404.39	408.75	417.80
Peak degradation temperature (°C)	251.65	430.21	430.15	431.33	458.08
Maximum weight loss rate (% $°C^{-1}$)	-1.342	-0.794	-0.866	-0.726	-0.759
Glass transition temperature (°C)	--	137.99	137.33	138.71	136.56
Tensile strength (MPa)	172.16	535.80	356.26	575.90	150.81
Youngs modulus (GPa)	6.96	11.01	5.95	11.38	4.36
Elongation at break (%)	4.44	2.64	2.92	2.59	3.05
Storage modulus (in glassy region) (MPa)	--	5786.20	5541.14	5998.97	4575.13
Storage modulus (in rubbery region) (MPa)	--	55.16	53.23	60.88	47.31
Density of composite (g cm^{-3})	2.409	1.626	1.565	1.761	1.405
% Heaviness with Pb at 100%	21.076	14.339	13.800	15.529	12.390
Mass attenuation coefficient at 0.662 MeV (cm^2 g^{-1})	0.090	0.087	0.095	0.096	0.098

--:- Not available.

5.2 Future prospects

Despite extensive research in this field, there is always potential for advancement in the development of environmentally friendly, light weight, and highly effective shielding materials. The experimental X-ray attenuation studies on SA/Bi_2O_3 and micro/nano-Ta_2O_5/epoxy samples can be performed using the CdTe X-ray detector spectrometer. Further, several composite systems based on biodegradable polymers can be explored for shielding thermo-mechanical and shielding properties. Some important environmental problems can be addressed by using biodegradable, reusable, or recyclable polymers as matrices. The increased usage of nanofillers is frequently met with agglomeration issues, poor matrix-filler interface adhesion leading to decrement in shielding properties. To solve these challenges, appropriate synthesis techniques may be investigated. More importantly, a systematic examination of filler size dependent shielding efficiency may prove beneficial in the development of innovative next-generation shielding materials. The integration of GO, single and multi-walled carbon nanotubes with high Z fillers to generate hybrid fillers can not only improve the physico-structural characteristics, but also address agglomeration problems and enhance shielding properties. Understanding the fundamentals of multi-layered polymer composite structure is required to optimise shielding materials with significant weight and cost savings over traditional shields. Above all, polymer composites are next - generation materials with multifunctional applications. Therefore, this research can be extended to study the usefulness of polymer composites for electromagnetic interference shielding (EMI), energy storage (battery, fuel cell, capacitor, etc) and dye degradation applications.

The structure of the thesis is planned in this way: **Chapter 1** will provide an introduction to the concept of radiation shielding and brief overview on routinely employed shielding materials highlighting the polymer matrix composites as contemporary research interest. **Chapter 2** will give a historical perspective and brief literature review of polymer composites used over the last three decades. In **Chapter 3**, the details on materials characterization, theoretical background and experimental radiation attenuation studies of polymer composites would be discussed. **Chapter 4** will describe the synthesis, characterization and γ-ray attenuation studies on the series of bismuth (III) oxide filled sodium alginate composites. In **Chapter 5**, will have discussions on the thermo-mechanical, viscoelastic and γ-ray shielding performance of micro/nano tantalum (V) oxide filled DGEBA epoxy composites. **Chapter 6** would present the studies on thermo-mechanical, viscoelastic, X-ray and γ-ray shielding properties of bismuth (III) oxide decorated graphene oxide filled DGEBA epoxy composites. **Chapter 7** will give a

brief overview on methodology, features and validity of newly developed PAGEX software. Summary of the research work and future prospects would be included in **Chapter 8**.

BIBLIOGRAPHY

1. Abasalizadeh, F., Moghaddam, S. V., Alizadeh, E., Kashani, E., Fazljou, S. M. B., Torbati, M., & Akbarzadeh, A. (2020). Alginate-based hydrogels as drug delivery vehicles in cancer treatment and their applications in wound dressing and 3D bioprinting. *Journal of Biological Engineering*, *14*, 1. https://doi.org/10.1186/s13036-020-0227-7
2. Abbas, M. I., El-Khatib, A. M., Dib, M. F., Mustafa, H. E., Sayyed, M. I., & Elsafi, M. (2022). The influence of Bi_2O_3 nanoparticle content on the γ-ray interaction parameters of silicon rubber. *Polymers*, *14*, 1048. https://doi.org/10.3390/polym14051048.
3. Abdalsalam, A. H., Şakar, E., Kaky, K. M., Mhareb, M. H. A., Şakar, B. C., Sayyed, M. I., & Gürol, A. (2020). Investigation of gamma ray attenuation features of bismuth oxide nano powder reinforced high-density polyethylene matrix composites. *Radiation Physics and Chemistry*, *168*, 108537. https://doi.org/10.1016/j.radphyschem.2019.108537.
4. Adlienė, D., Gilys, L., & Griškonis, E. (2020). Development and characterization of new tungsten and tantalum containing composites for radiation shielding in medicine. *Nuclear Instruments and Methods in Physics Research Section B: Beam Interactions with Materials and Atoms*, *467*, 21. https://doi.org/10.1016/j.nimb.2020.01.027.
5. Ambika, M. R., Nagaiah, N., & Suman, S. K. (2017). Role of bismuth oxide as a reinforcer on gamma shielding ability of unsaturated polyester-based polymer composites. *Journal of Applied Polymer Science*, *134*. https://doi.org/10.1002/app.44657.
6. ANSI/ANS-6.4.3 (1991). Gamma-ray attenuation coefficient and buildup factors for engineering materials. American Nuclear Society, La Grange Park, Illinois.
7. Arshad, M., Zubair, M., Rahman, S. S., & Ullah, A. (2020). Polymers for advanced applications. In *Polymer Science and Nanotechnology* (pp. 325-340). Elsevier. https://doi.org/10.1016/B978-0-12-816806-6.00014-5.
8. Asgari, M., Afarideh, H., Ghafoorifard, H., & Amirabadi, E. A. (2021). Comparison of nano/micro lead, bismuth and tungsten on the gamma shielding properties of the flexible composites against photon in wide energy range (40 keV–662 keV). *Nuclear Engineering and Technology*, *53*, 4142. https://doi.org/10.1016/j.net.2021.06.022.

9. Augst, A. D., Kong, H. J., & Mooney, D. J. (2006). Alginate hydrogels as biomaterials. *Macromolecular Bioscience*, *6*(8), 623. https://doi.org/10.1002/mabi.200600069
10. Badita, C. R., Aranghel, D., Burducea, C., & Mereuta, P. (2020). Characterization of sodium alginate-based films. *Romanian Journal of Physics*, *65*, 1. http://www.nipne.ro/rjp/2020_65_1-2/RomJPhys.65.602.pdf.
11. Bagheri, K., Razavi, S. M., Ahmadi, S. J., Kosari, M., & Abolghasemi, H. (2018). Thermal resistance, tensile properties, and gamma radiation shielding performance of unsaturated polyester/nanoclay/PbO composites. *Radiation Physics and Chemistry*, *146*, 5. https://doi.org/10.1016/j.radphyschem.2017.12.024.
12. Biersack, H. J., & Freeman, L. M. (Eds.). (2008). *Clinical nuclear medicine*. Springer Science & Business Media.
13. Berger, M. J., & Hubbell, J. H. (1987). XCOM: Photon cross sections on a personal computer (No. NBSIR-87-3597). National Bureau of Standards, Washington, DC (USA). Center for Radiation Research. https://doi.org/10.2172/6016002.
14. Berger, M. J., Coursey, J. S., Zucker, M. A., & Chang, J. (2005). ESTAR, PSTAR, and ASTAR: Computer programs for calculating stopping power and range tables for electrons, protons, and helium ions (version 1.2.3) [Online] Available: http://physics.nist.gov/Star [2018, October10]. National Institute of Standards and Technology, Gaithersburg, MD.
15. Boone, J. M., & Chavez, A. E. (1996). Comparison of X-ray cross sections for diagnostic and therapeutic medical physics. *Medical Physics*, *23*, 1997. https://doi.org/10.1118/1.597899.
16. Büyükyıldız, M., Kurudirek, M., Ekici, M., İçelli, O., & Karabul, Y. (2017). Determination of radiation shielding parameters of 304L stainless steel specimens from welding area for photons of various gamma ray sources. *Progress in Nuclear Energy*, *100*, 245. https://doi.org/10.1016/j.pnucene.2017.06.014.
17. Canel, A., Korkut, H., & Korkut, T. (2019). Improving neutron and gamma flexible shielding by adding medium-heavy metal powder to epoxy based composite materials. *Radiation Physics and Chemistry*, *158*, 13. https://doi.org/10.1016/j.radphyschem.2019.01.005.
18. Cao, D., Yang, G., Bourham, M., & Moneghan, D. (2020). Gamma radiation shielding properties of poly (methyl methacrylate)/Bi_2O_3 composites. *Nuclear Engineering and Technology*, *52*, 2613. https://doi.org/10.1016/j.net.2020.04.026.

19. Chang, L., Zhang, Y., Liu, Y., Fang, J., Luan, W., Yang, X., & Zhang, W. (2015). Preparation and characterization of tungsten/epoxy composites for γ-rays radiation shielding. *Nuclear Instruments and Methods in Physics Research Section B: Beam Interactions with Materials and Atoms*, *356*, 88. https://doi.org/10.1016/j.nimb.2015.04.062.
20. Chen, J., Yao, B., Li, C., & Shi, G. (2013). An improved Hummers method for eco-friendly synthesis of graphene oxide. *Carbon*, *64*, 225. https://doi.org/10.1016/j.carbon.2013.07.055.
21. Chilton, A. B., Shultis, J. K., & Faw, R. (1984). Principles of radiation shielding. United States: Prentice Hall Inc.
22. Deepa, B., Abraham, E., Pothan, L. A., Cordeiro, N., Faria, M., & Thomas, S. (2016). Biodegradable nanocomposite films based on sodium alginate and cellulose nanofibrils. *Materials*, *9*, 50. https://doi.org/10.3390/ma9010050.
23. El-Toony, M. M., Eid, G., Algarni, H. M., Alhuwaymel, T. F., & Abel-Hady, E. E. (2020). Synthesis and characterisation of smart poly vinyl ester/Pb_2O_3 nanocomposite for gamma radiation shielding. *Radiation Physics and Chemistry*, *168*, 108536. https://doi.org/10.1016/j.radphyschem.2019.108536.
24. Eren Belgin, E., & Aycik, G. A. (2015). Preparation and radiation attenuation performances of metal oxide filled polyethylene-based composites for ionizing electromagnetic radiation shielding applications. *Journal of Radioanalytical and Nuclear Chemistry*, *306*, 107. http://dx.doi.org/10.1007/s10967-015-4052-2.
25. Eyecioğlu, Ö., El-Khayatt, A. M., Karabul, Y., Çağlar, M., Toker, O., & İçelli, O. (2019). BXCOM: A software for computation of radiation sensing. *Radiation Effects and Defects in Solids*, 174, 506. https://doi.org/10.1080/10420150.2019.1606811.
26. Fan, J., Wu, J., & Ma, Y. (2020). Effect of different size of $PbWO_4$ particles on EPDM composite for gamma-ray shielding. *International Journal of Modern Physics B*, *34*, 2050046. https://doi.org/10.1142/S0217979220500460.
27. Gerward, L., Guilbert, N., Jensen, K. B., & Levring, H. (2001). X-ray absorption in matter. Reengineering XCOM. *Radiation Physics and Chemistry*, *60*, 23. https://doi.org/10.1016/S0969-806X(00)00324-8.
28. Gerward, L., Guilbert, N., Jensen, K. B., & Levring, H. (2004). WinXCom—a program for calculating X-ray attenuation coefficients. *Radiation Physics and chemistry*, *71*, 653. https://doi.org/10.1016/j.radphyschem.2004.04.040

29. Gwaily, S. E., Madani, M., & Hassan, H. H. (2002). Lead—natural rubber composites as gamma radiation shields. II: high concentration. *Polymer Composites*, *23*, 495. https://doi.org/10.1002/pc.10450
30. Han, S., Um, W., & Kim, W. S. (2019). Development of bismuth-functionalized graphene oxide to remove radioactive iodine. *Dalton Transactions*, *48*, 478. https://doi.org/10.1039/C8DT03745K.
31. Harish, V., Nagaiah, N., & Kumar, H. G. (2012). Lead oxides filled isophthalic resin polymer composites for gamma radiation shielding applications. http://nopr.niscair.res.in/handle/123456789/14920.
32. Hashemi, S. A., Mousavi, S. M., Faghihi, R., Arjmand, M., Sina, S., & Amani, A. M. (2018). Lead oxide-decorated graphene oxide/epoxy composite towards X-ray radiation shielding. *Radiation Physics and Chemistry*, *146*, 77. https://doi.org/10.1016/j.radphyschem.2018.01.008.
33. Hosseini, M. A., Malekie, S., & Kazemi, F. (2022). Experimental evaluation of gamma radiation shielding characteristics of polyvinyl alcohol/tungsten oxide composite: A comparison study of micro and nano sizes of the fillers. *Nuclear Instruments and Methods in Physics Research Section A: Accelerators, Spectrometers, Detectors and Associated Equipment*, *1026*, 166214. https://doi.org/10.1016/j.nima.2021.166214.
34. Huang, M. H., & Yang, M. C. (2010). Swelling and biocompatibility of sodium alginate/poly (γ-glutamic acid) hydrogels. *Polymers for Advanced Technologies*, *21*, 561. https://doi.org/10.1002/pat.1466.
35. Hubbell, J. H., & Overbo, I. (1979). Relativistic atomic form factors and photon coherent scattering cross sections. *Journal of Physical and Chemical Reference Data*, *8*, 69. https://doi.org/10.1063/1.555593.
36. Hubbell, J. H., & Seltzer, S. M. (1995). Tables of X-ray mass attenuation coefficients and mass energy-absorption coefficients 1 keV to 20 MeV for elements Z= 1 to 92 and 48 additional substances of dosimetric interest (No. PB-95-220539/XAB; NISTIR-5632). National Inst. of Standards and Technology-PL, Gaithersburg, MD (United States). Ionizing Radiation Div. https://www.nist.gov/pml/data/xraycoef/index.cfm.
37. Hubbell, J. H., Gimm, H. A., & O/verbo/, I. (1980). Pair, triplet, and total atomic cross sections (and mass attenuation coefficients) for 1 MeV-100 GeV photons in elements Z= 1 to 100. *Journal of Physical and Chemical Reference Data*, *9*, 1023. https://doi.org/10.1063/1.555629.

38. Hubbell, J. H., Veigele, W. J., Briggs, E. A., Brown, R. T., Cromer, D. T., & Howerton, D. R. (1975). Atomic form factors, incoherent scattering functions, and photon scattering cross sections. *Journal of Physical and Chemical Reference Data*, *4*, 471. https://doi.org/10.1063/1.555523.
39. Ibrahim, N. I., Shahar, F. S., Sultan, M. T. H., Shah, A. U. M., Safri, S. N. A., & Mat Yazik, M. H. (2021). Overview of bioplastic introduction and its applications in product packaging. *Coatings*, *11*, 1423. https://doi.org/10.3390/coatings11111423.
40. Intom, S., Kalkornsurapranee, E., Johns, J., Kaewjaeng, S., Kothan, S., Hongtong, W., Chaiphaksa, W., & Kaewkhao, J. (2020). Mechanical and radiation shielding properties of flexible material based on natural rubber/Bi_2O_3 composites. *Radiation Physics and Chemistry*, *172*, 108772. https://doi.org/10.1016/j.radphyschem.2020.108772.
41. Jyoti, J., Singh, B. P., Arya, A. K., & Dhakate, S. R. (2016). Dynamic mechanical properties of multiwall carbon nanotube reinforced ABS composites and their correlation with entanglement density, adhesion, reinforcement and C factor. *RSC advances*, 6, 3997. https://doi.org/10.1039/C5RA25561A.
42. Kaneda, K., Kuroda, S., Goto, N., Sato, D., Ohya, K., & Kasugai, S. (2008). Is sodium alginate an alternative haemostatic material in the tooth extraction socket? *Journal of Oral Tissue Engineering*, *5*, 127. https://doi.org/10.11223/jarde.5.127
43. Kaplan, M. F. (1989). Concrete radiation shielding. John Wiley and Sons Inc.
44. Kim, J., Seo, D., Lee, B. C., Seo, Y. S., & Miller, W. H. (2014). Nano-W Dispersed Gamma Radiation Shielding Materials. *Advanced Engineering Materials*, *16*, 1083. https://doi.org/10.1002/adem.201400127.
45. Kumar Giri, T., Thakur, D., Alexander, A., Badwaik, H., & Krishna Tripathi, D. (2012). Alginate based hydrogel as a potential biopolymeric carrier for drug delivery and cell delivery systems: present status and applications. *Current Drug Delivery*, *9*, 539. https://doi.org/10.2174/156720112803529800
46. Lee, K. Y., & Mooney, D. J. (2012). Alginate: properties and biomedical applications. *Progress in Polymer Science*, *37*, 106. https://doi.org/10.1016/j.progpolymsci.2011.06.003
47. Li, R., Gu, Y., Wang, Y., Yang, Z., Li, M., & Zhang, Z. (2017). Effect of particle size on gamma radiation shielding property of gadolinium oxide dispersed epoxy resin matrix composite. *Materials Research Express*, *4*, 035035. https://doi.org/10.1088/2053-1591/aa6651.

48. Lima, A. M. F., Lima, M. D. F., Assis, O. B. G., Raabe, A., Amoroso, H. C., de Oliveira Tiera, V. A., Andrade, M. B. D. and Tiera, M. J. (2018). Synthesis and physicochemical characterization of multiwalled carbon nanotubes/hydroxamic alginate nanocomposite scaffolds. *Journal of Nanomaterials*, *2018*. https://doi.org/10.1155/2018/4218270.
49. Mahmoud, K. A., Lacomme, E., Sayyed, M. I., Özpolat, Ö. F., & Tashlykov, O. L. (2020). Investigation of the gamma ray shielding properties for polyvinyl chloride reinforced with chalcocite and hematite minerals. *Heliyon*, *6*, e03560. https://doi.org/10.1016/j.heliyon.2020.e03560.
50. Mahmoud, M. E., El-Khatib, A. M., Badawi, M. S., Rashad, A. R., El-Sharkawy, R. M., & Thabet, A. A. (2018). Fabrication, characterization and gamma rays shielding properties of nano and micro lead oxide-dispersed-high density polyethylene composites. *Radiation Physics and Chemistry*, *145*, 160. https://doi.org/10.1016/j.radphyschem.2017.10.017.
51. Majka, T. M., Leszczyńska, A., & Pielichowski, K. (2016). Thermal stability and degradation of polymer nanocomposites. In *Polymer nanocomposites* (pp. 167-190). Springer, Cham.
52. Manjula, B., Varaprasad, K., Sadiku, R., & Raju, K. M. (2013). Preparation and characterization of sodium alginate–based hydrogels and their in vitro release studies. *Advances in Polymer Technology*, *32*. https://doi.org/10.1002/adv.21340.
53. McAlister, D. R. (2012). Gamma ray attenuation properties of common shielding materials. USA: University Lane Lisle.
54. Mehrara, R., Malekie, S., Kotahi, S. M. S., & Kashian, S. (2021). Introducing a novel low energy gamma ray shield utilizing polycarbonate bismuth oxide composite. *Scientific Reports*, *11*, 1. https://doi.org/10.1038/s41598-021-89773-5.
55. Mirzaei, M., Zarrebini, M., Shirani, A., Shanbeh, M., & Borhani, S. (2019). X-ray shielding behavior of garment woven with melt-spun polypropylene monofilament. *Powder Technology*, *345*, 15. https://doi.org/10.1016/j.powtec.2018.12.069.
56. Mulik, B. B., Bankar, B. D., Munde, A. V., Biradar, A. V., & Sathe, B. R. (2020). Bismuth-oxide-decorated graphene oxide hybrids for catalytic and electrocatalytic reduction of CO_2. *Chemistry–A European Journal*, *26*, 8801. https://doi.org/10.1002/chem.202001589.
57. Muthamma, M. V., Bubbly, S. G., & Gudennavar, S. B. (2020). Attenuation properties of epoxy-Ta_2O_5 and epoxy-Ta_2O_5-Bi_2O_3 composites at γ-ray energies 59.54 and 662 keV. *Journal of Applied Polymer Science*, *137*, 49366. https://doi.org/10.1002/app.49366.

58. Muthamma, M. V., Gudennavar, B. S., & Gudennavar, S. B. (2020). Attenuation parameters of polyvinyl alcohol-tungsten oxide composites at the photon energies 5.895, 6.490, 59.54 and 662 keV. *Polish Journal of Medical Physics and Engineering*, *26*, 77. https://doi.org/10.2478/pjmpe-2020-0009.
59. Muthamma, M. V., Prabhu, S., Bubbly, S. G., & Gudennavar, S. B. (2021). Micro and nano Bi_2O_3 filled epoxy composites: Thermal, mechanical and γ-ray attenuation properties. *Applied Radiation and Isotopes*, *174*, 109780. https://doi.org/10.1016/j.apradiso.2021.109780.
60. Nishiya, M., Hareyama, H., Makinoda, S., & Fujimoto, S. (1994). A study on the hemostatic effect of sodium alginate on uterocervical hemorrhage. *Asia-Oceania Journal of Obstetrics and Gynaecology*, *20*, 203. https://doi.org/10.1111/j.1447-0756.1994.tb00451.x
61. Nowotny, R. (1998). XMuDat: Photon attenuation data on PC. IAEA Report IAEA-NDS 195.
62. Olarinoye, I. O., Odiaga, R. I., & Paul, S. (2019). EXABCal: A program for calculating photon exposure and energy absorption buildup factors. *Heliyon*, *5*, e02017. https://doi.org/10.1016/j.heliyon.2019.e02017.
63. Özpolat, Ö. F., Alım, B., Şakar, E., Büyükyıldız, M., & Kurudirek, M. (2020). Phy-X/ZeXTRa: A software for robust calculation of effective atomic numbers for photon, electron, proton, alpha particle, and carbon ion interactions. *Radiation and Environmental Biophysics*, *59*, 321. https://doi.org/10.107/s00411-019-00829-7.
64. Pavlath, A. E., Gossett, C., Camirand, W., & Robertson, G. H. (1999). Ionomeric films of alginic acid. *Journal of Food Science*, *64*, 61. https://doi.org/10.1111/j.1365-2621.1999.tb09861.x.
65. Pavlenko, V. I., Cherkashina, N. I., & Yastrebinsky, R. N. (2019). Synthesis and radiation shielding properties of polyimide/Bi_2O_3 composites. *Heliyon*, *5*, e01703. https://doi.org/10.1016/j.heliyon.2019.e01703.
66. Pratt, R. H. (1960). Photoeffect from the L shell. *Physical Review*, *119*, 1619. https://doi.org/10.1103/PhysRev.119.1619.
67. Rhim, J. W. (2004). Physical and mechanical properties of water-resistant sodium alginate films. *LWT-Food Science and Technology*, *37*, 323. https://doi.org/10.1016/j.lwt.2003.09.008

68. Riyajan, S. A., Sasithornsonti, Y., & Phinyocheep, P. (2012). Green natural rubber-g-modified starch for controlling urea release. *Carbohydrate Polymers*, *89*, 251. https://doi.org/10.1016/j.carbpol.2012.03.004.
69. Russo, P. (Ed.). (2017). *Handbook of X-ray imaging: physics and technology*. CRC press.
70. Sachan, N. K., Pushkar, S., Jha, A., & Bhattcharya, A. (2009). Sodium alginate: the wonder polymer for controlled drug delivery. *Journal of Pharmacy Research*, *2*, 1191.
71. Şakar, E., Özpolat, Ö. F., Alım, B., Sayyed, M. I., & Kurudirek, M. (2020). Phy-X/PSD: development of a user-friendly online software for calculation of parameters relevant to radiation shielding and dosimetry. *Radiation Physics and Chemistry*, *166*, 108496. https://doi.org/10.1016/j.radphyschem.2019.108496.
72. Scofield, J. H. (1973). UCRL report 51326. *Lawrence Livermore Laboratory, Livermore, CA*.
73. Shah, S., Qureshi, A., Singh, N. L., Kulriya, P. K., Singh, K. P., & Avasthi, D. K. (2009). Structural and chemical modification of polymer composite by proton irradiation. *Surface and Coatings Technology*, *203*, 2595. https://doi.org/10.1016/j.surfcoat.2009.02.052.
74. Sharifi, S., Bagheri, R., & Shirmardi, S. P. (2013). Comparison of shielding properties for ordinary, barite, serpentine and steel–magnetite concretes using MCNP-4C code and available experimental results. *Annals of Nuclear Energy*, *53*, 529. http://dx.doi.org/10.1016/j.anucene.2012.09.015.
75. Sharma, S., Sudhakara, P., Singh, J., Ilyas, R. A., Asyraf, M. R. M., & Razman, M. R. (2021). Critical review of biodegradable and bioactive polymer composites for bone tissue engineering and drug delivery applications. *Polymers*, 13, 2623. https://doi.org/10.3390/polym13162623.
76. Sime, W. J. (1990). Alginates. In *Food gels* (pp. 53-78). Springer, Dordrecht.
77. Singh, B., Sharma, V., & Chauhan, D. (2010). Gastroretentive floating sterculia–alginate beads for use in antiulcer drug delivery. *Chemical Engineering Research and Design*, *88*, 997. https://doi.org/10.1016/j.cherd.2010.01.017
78. Stabin, M. G. (Ed.). (2007). *Radiation protection and dosimetry*. New York, NY: Springer New York.
79. Tavakoli, F., Salavati-Niasari, M., & Mohandes, F. (2015). Green synthesis and characterization of graphene nanosheets. *Materials Research Bulletin*, *63*, 51. https://doi.org/10.1016/j.materresbull.2014.11.045.

80. Taylor, M. L., Smith, R. L., Dossing, F., & Franich, R. D. (2012). Robust calculation of effective atomic numbers: The Auto-Z_{eff} software. *Medical Physics*, *39*, 1769. https://doi.org/10.1118/1.3689810
81. Toyen, D., Rittirong, A., Poltabtim, W., & Saenboonruang, K. (2018). Flexible, lead-free, gamma-shielding materials based on natural rubber/metal oxide composites. *Iranian Polymer Journal*, *27*, 33. https://doi.org/10.1007/s13726-017-0584-3.
82. Un, A., & Caner, T. (2014). The Direct-Z_{eff} software for direct calculation of mass attenuation coefficient, effective atomic number and effective electron number. *Annals of Nuclear Energy*, *65*, 158. https://doi.org/10.1016/j.anucene.2013.10.041.
83. Verdipoor, K., Alemi, A., & Mesbahi, A. (2018). Photon mass attenuation coefficients of a silicon resin loaded with WO_3, PbO, and Bi_2O_3 micro and nano-particles for radiation shielding. *Radiation Physics and Chemistry*, *147*, 85. https://doi.org/10.1016/j.radphyschem.2018.02.017.
84. White, D. R., Booz, J., Griffith, R. V., Spokas, J. J., & Wilson, I. J. (1989). Tissue substitutes in radiation dosimetry and measurement. International Commission on Radiation Units and Measurements. Report 44.
85. World Health Organization (WHO). Ionizing radiation, health effects and protective measures. https://www.who.int/news-room/fact-sheets/detail/ionizing-radiation-health-effects-and-protective-measures. (Accessed March 15, 2022).
86. Wu, Y., Cao, Y., Wu, Y., & Li, D. (2020). Mechanical properties and gamma-ray shielding performance of 3D-printed poly-ether-ether-ketone/tungsten composites. *Materials*, *13*, 4475. https://doi.org/10.3390/ma13204475.
87. Yılmaz, S. N., Güngör, A., & Özdemir, T. (2020). The investigations of mechanical, thermal and rheological properties of polydimethylsiloxane/bismuth (III) oxide composite for X-/gamma ray shielding. *Radiation Physics and Chemistry*, *170*, 108649.https://doi.org/10.1016/j.radphyschem.2019.108649.
88. Yu, L., Yap, P. L., Santos, A., Tran, D., & Losic, D. (2021). Lightweight bismuth titanate ($Bi_4Ti_3O_{12}$) nanoparticle-epoxy composite for advanced lead-free X-ray radiation shielding. *ACS Applied Nano Materials*, *4*, 7471. https://doi.org/10.1021/acsanm.1c01475.
89. Zegaoui, A., Derradji, M., Medjahed, A., Dayo, A. Q., Dong, W., Liu, W. B., Cai, W. A., Wang, J., & Liu, Y.G. (2018). Multifunctional polymer materials with enhanced mechanical, thermal and gamma radiation shielding properties from dicyanate ester of

bisphenol-A/bisphenol-A based benzoxazine resin and short kevlar/basalt hybrid fibers. *Journal of Polymer Research*, *25*, 1. https://doi.org/10.1007/s10965-018-1652-x.

90. Zegaoui, A., Derradji, M., Medjahed, A., Ghouti, H. A., Cai, W. A., Liu, W. B., Dayo, A. Q., Wang, J., & Liu, Y. G. (2020). Exploring the hybrid effects of short glass/basalt fibers on the mechanical, thermal and gamma-radiation shielding properties of DCBA/BA-a resin composites. *Polymer-Plastics Technology and Materials*, *59*, 311. https://doi.org/10.1080/25740881.2019.1647237.
91. Zheng, H., Yang, J., & Han, S. (2016). The synthesis and characteristics of sodium alginate/graphene oxide composite films crosslinked with multivalent cations. *Journal of Applied Polymer Science*, *133*. https://doi.org/10.1002/app.43616.
92. Ziegler, J. F., Ziegler, M. D., & Biersack, J. P. (2010). SRIM–The stopping and range of ions in matter (2010). *Nuclear Instruments and Methods in Physics Research Section B: Beam Interactions with Materials and Atoms*, *268*, 1818. https://doi.org/10.1016/j.nimb.2010.02.091.
93. Zohdiaghdam, R., Mahmoudian, M., & Salimi, S. (2020). Evaluation of synergistic effects of the single walled carbon nanotube and CeO_2-hybrid based-nanocomposite against X-ray radiation in diagnostic radiology. *Radiation Physics and Chemistry*, *168*, 108562. https://doi.org/10.1016/j.radphyschem.2019.108562

PUBLICATIONS/PROCEEDINGS

In journals:

1. Bismuth (III) oxide decorated graphene oxide filled epoxy nanocomposites: Thermo- mechanical and photon attenuation properties, **Srilakshmi Prabhu**, S G Bubbly and S B Gudennavar, Advanced Composite Materials (Under revision). **(IF: 2.870)**
2. X-ray and γ-ray shielding efficiency of polymer composites: Choice of fillers, effect of loading and filler size, photon energy and multifunctionality, **Srilakshmi Prabhu**, S G Bubbly and S B Gudennavar, Polymer Reviews, 66, 2022. https://doi.org/10.1080/15583724.2022.2067867. **(IF: 14.536)**
3. A simple software for swift computation of photon and charged particle interaction parameters: PAGEX, **Srilakshmi Prabhu**, Sreehari Jayaram, S G Bubbly and S B Gudennavar, Applied Radiation and Isotopes, 176, 109903, 2021. https://doi.org/10.1016/j.apradiso.2021.109903. **(IF: 1.787)**

4. Natural polymer-based hydrogels as prospective tissue equivalent materials for radiation therapy and dosimetry, **Srilakshmi Prabhu**, Dhanya Y Bharadwaj, Rachaita Podder, S G Bubbly and S B Gudennavar, Physical and Engineering Sciences in Medicine, 44(4), 1107, 2021. https://doi.org/10.1007/s13246-021-01047-6. **(IF: 7.099)**
5. Thermal, mechanical and γ-ray shielding properties of micro-and nano-Ta_2O_5 loaded DGEBA epoxy resin composites, **Srilakshmi Prabhu**, S G Bubbly and S B Gudennavar, Journal of Applied Polymer Science, 138(44), 51289, 2021. https://doi.org/10.1002/app.51289. **(IF: 3.057)**
6. Micro and nano Bi_2O_3 filled epoxy composites: Thermal, mechanical and γ-ray attenuation properties, Muthamma M V, **Srilakshmi Prabhu**, S G Bubbly and S B Gudennavar, Applied Radiation and Isotopes, 174, 109780, 2021. https://doi.org/10.1016/j.apradiso.2021.109780. **(IF: 1.787)**
7. Sodium alginate/bismuth (III) oxide composites for γ-ray shielding applications, **Srilakshmi Prabhu**, S G Bubbly and S B Gudennavar, Journal of Applied Polymer Science, 138(19), 50369, 2021. https://doi.org/10.1002/app.50369. **(IF: 3.057)**
8. Synthetic polymer hydrogels as potential tissue phantoms in radiation therapy and dosimetry, **Srilakshmi Prabhu**, S G Bubbly and S B Gudennavar, Biomedical Physics & Engineering Express, 6(5), 055008, 2020. https://doi.org/10.1088/2057-1976/aba209. **(IF: 1.463)**
9. Effective atomic number and electron density of some biologically important lipids for electron, proton, alpha particle and photon interactions, **Srilakshmi Prabhu**, Sneha A C, Pooja P Shetty, Arundati A Narkar, Bubbly S G and S B Gudennavar, Applied Radiation and Isotopes, 160, 109137, 2020. https://doi.org/10.1016/j.apradiso.2020.109137. **(IF: 1.270)**

In conference proceedings/book:

1. Preparation and characterization of tungsten carbide/epoxy composites for γ-ray shielding, **Srilakshmi Prabhu**, S G Bubbly and S B Gudennavar, AIP Conference Proceedings, 2021 (IF: 0.402) **(Accepted)**
2. Multi-layered epoxy composites of micro and nano Bi_2O_3 and Ta_2O_5 for γ-ray shielding, **Srilakshmi Prabhu**, Ajith Geejo, Rohit Dagar, Divyasree Chakraborty, Andrews Jacob, Sriya Paul, S G Bubbly and S B Gudennavar, Advances in Sustainability Science and Technology: Proceedings of Fourth International

Conference on Inventive Material Science Applications (ICIMA 2021), edited by V Bindhu, R S João Manuel and S T Tavares, 2021, ISBN No. 978-981-16-4321-7, pp. 457-467, Springer Nature, Singapore. https://doi.org/10.1007/978-981-16-4321-7_38.

Conferences/workshops/training attended:

1. Polymer composites for shielding of neutron and γ-radiations, **Srilakshmi Prabhu**, S G Bubbly and S B Gudennavar, DAE-BRNS Theme Meeting on Strategic Planning for Enhanced Research Reactor Utilization (RRU-2022) held during May 6 – 7, 2022 at Bhabha Atomic Research Centre (BARC), Mumbai. *(Poster presentation)*
2. Attended one-week online (July 12 to July 19, 2021) High-end workshop (Karyashala) on Software Tools and Techniques used in EHEP and its Applications" organized by Accelerate Vigyan Scheme of SERB (DST), New Delhi
3. Preparation and characterization of tungsten carbide/epoxy composites for γ-ray shielding, **Srilakshmi Prabhu**, S G Bubbly and S B Gudennavar, Proceedings of International Conference on Advances in Multi-Disciplinary Sciences and Engineering Research (ICAMSER-2021) held during July 2 - 4, 2021 at Chitkara University, Himachal Pradesh. *(Best Paper Award, Oral presentation)*
4. Multi-layered epoxy composites of micro and nano Bi_2O_3 and Ta_2O_5 for γ-ray shielding, **Srilakshmi Prabhu**, Ajith Geejo, Rohit Dagar, Divyasree Chakraborty, Andrews Jacob, Sriya Paul, S G Bubbly and S B Gudennavar, Proceedings of International Conference on Inventive Material Science and Applications (ICIMA 2021) held during May 14 - 15, 2021 at PPG Institute of Technology, Coimbatore, Tamil Nadu, India. (*Oral presentation*)
5. Bi_2O_3 filled sodium alginate composites as γ-ray shielding materials, **Srilakshmi Prabhu**, S G Bubbly and S B Gudennavar, Proceedings of the 11th International Conference on Advancements in polymeric materials (APM-2020) held during February 13-15, 2020 at Central Institute of Plastics Engineering & Technology (CIPET), Bengaluru, India. (*Oral presentation*)
6. Thermo-mechanical and γ-radiation shielding properties of micro and nano-sized Bi_2O_3 and Ta_2O_5 dispersed epoxy resin matrix composites, **Srilakshmi Prabhu**, Muthamma M V, S G Bubbly and S B Gudennavar, Proceedings of the 11th International Conference on Advancements in polymeric materials (APM-2020) held during

February 13-15, 2020 at Central Institute of Plastics Engineering & Technology (CIPET), Bengaluru, India. (*Oral presentation*)

7. Polymer-high Z element composites as X-ray and shields, S B Gudennavar, S G Bubbly and **Srilakshmi Prabhu**, Proceedings of the 11th International Conference on Advancements in polymeric materials (APM-2020) held during February 13-15, 2020 at Central Institute of Plastics Engineering & Technology (CIPET), Bengaluru, India. (*Oral presentation*)
8. Fabrication, thermo-mechanical characterization and γ-radiation shielding properties of micro and nano bismuth oxide dispersed epoxy resin composites, **Srilakshmi Prabhu**, Muthamma M V, S G Bubbly and S B Gudennavar, Proceedings of the International Conference on Advances in Materials, Ceramics & Engineering Sciences (AMCES-2020) held during January 17-18, 2020 at Dayananda Sagar College of Engineering, Bengaluru, India. *(Best oral presentation award)*